

**Simulation of long lived tracers using an improved  
empirically-based two-dimensional model transport algorithm**

E. L. Fleming,<sup>1,2</sup> C. H. Jackman,<sup>2</sup>, R.S. Stolarski,<sup>2</sup> D. B. Considine<sup>3,2</sup>

111-45

411365-

Short title: TWO-DIMENSIONAL SIMULATIONS OF LONG-LIVED TRACERS



**Abstract.**

We have developed a new empirically-based transport algorithm for use in our GSFC two-dimensional transport and chemistry model. The new algorithm contains planetary wave statistics, and parameterizations to account for the effects due to gravity waves and equatorial Kelvin waves. As such, this scheme utilizes significantly more information compared to our previous algorithm which was based only on zonal mean temperatures and heating rates. The new model transport captures much of the qualitative structure and seasonal variability observed in long lived tracers, such as: isolation of the tropics and the southern hemisphere winter polar vortex; the well mixed surf-zone region of the winter sub-tropics and mid-latitudes; the latitudinal and seasonal variations of total ozone; and the seasonal variations of mesospheric H<sub>2</sub>O. The model also indicates a double peaked structure in methane associated with the semiannual oscillation in the tropical upper stratosphere. This feature is similar in phase but is significantly weaker in amplitude compared to the observations. The model simulations of carbon-14 and strontium-90 are in good agreement with observations, both in simulating the peak in mixing ratio at 20-25 km, and the decrease with altitude in mixing ratio above 25 km. We also find mostly good agreement between modeled and observed age of air determined from SF<sub>6</sub> outside of the northern hemisphere polar vortex. However, observations inside the vortex reveal significantly older air compared to the model. This is consistent with the model deficiencies in simulating CH<sub>4</sub> in the northern hemisphere winter high latitudes and illustrates the limitations of the current climatological zonal mean model formulation. The propagation of seasonal signals in water vapor and CO<sub>2</sub> in the lower stratosphere showed general agreement in phase, and the model qualitatively captured the observed amplitude decrease in CO<sub>2</sub> from the tropics to midlatitudes. However, the simulated seasonal amplitudes were attenuated too rapidly with altitude in the tropics. Overall, the simulations with the new transport formulation are in substantially better agreement with observations compared with our previous model transport.



## 1. Introduction

Two-dimensional (2D) chemistry and transport models have been used extensively to study various natural physical processes in the middle atmosphere, and to assess the long-term impact of man-made halogens on stratospheric ozone [WMO, 1991, 1995]. Of fundamental importance in 2D modeling is the proper representation of the zonally averaged transport fields which are comprised of mean advective and eddy flux components. Previous theoretical development has shown that the residual circulation of the transformed Eulerian mean (TEM) formulation provides a reasonable approximation to the net advective mass transport in the meridional plane [e.g., Andrews and McIntyre, 1976; Dunkerton, 1978]. Earlier models which used a TEM or isentropic formulation for the mean transport and a constant diffusion coefficient to parameterize the eddy flux effects were able to reproduce some general features of the observed zonal mean temperature, zonal wind, and long lived tracer fields [e.g., Garcia and Solomon, 1983; Ko *et al.*, 1985]. Other model studies have specified various eddy diffusion rates to investigate the exchange of mass between the tropics and mid-latitudes [e.g., Weisenstein *et al.*, 1996].

Subsequent studies noted that planetary wave processes simultaneously generate both a mean circulation and eddy flux effects so that a model formulation should account for these components in a self-consistent manner. For 2-D models with empirically based 'fixed' transport schemes, these quantities were typically diagnosed from empirically determined temperatures and net heating rates [e.g., Newman *et al.*, 1988; Yang *et al.*, 1991; Patten *et al.*, 1994; Fleming *et al.*, 1995]. Here, the wave drag and diffusion were not derived explicitly, but were inferred from the residual needed to balance the zonal momentum equation. Fully coupled models, in which the zonal mean dynamical fields are computed interactively with the ozone and constituent distributions [e.g., Garcia and Solomon, 1983], now usually include a parameterization to explicitly compute the wave induced drag and diffusion due to planetary wave breaking [Garcia, 1991]. This also allows for feedback between the planetary wave field and the zonal mean flow.

In addition to planetary waves, parameterizations have been developed to compute the effects of small scale waves. For example, the parameterization of Dunkerton [1979] computed the momentum deposition due to Kelvin wave absorption in the tropical upper stratosphere, which is important for simulation of the semiannual oscillation (SAO). Lindzen [1981] developed a parameterization to account for the effects of breaking gravity waves in the mesosphere. This scheme has subsequently been widely incorporated into chemical and dynamical models [e.g., Holton and Zhu, 1984; Garcia and Solomon, 1985; Gray and Pyle, 1987; Brasseur *et al.*, 1990]. Other gravity wave drag schemes [e.g., Bacmeister, 1993; Pierrehumbert, 1987; Hines, 1997] have recently been developed and incorporated into 2D chemical and/or dynamical models [Mengel *et al.*, 1996; Summers *et al.*, 1997].

These parameterizations have enabled models to better simulate the general zonal mean temperature and zonal wind structure in the middle atmosphere, as well as characteristic dynamical features observed in long lived tracers such as the degree of



tropical and polar vortex isolation, the sub-tropical/mid-latitude surf zone of the winter hemisphere, and the upper stratospheric SAO double-peaked structure [e.g., Gray and Pyle, 1987; Brasseur *et al.*, 1990; Choi and Holton, 1991; Yang *et al.*, 1991; Garcia *et al.*, 1992; Bacmeister *et al.*, 1995; Nightingale *et al.*, 1996; Jackman *et al.*, 1996; Summers *et al.*, 1997].

In addition to the development of parameterizations of wave processes, recent work in 2D chemical modeling in general has tended to focus on the development of fully interactive models [e.g., Garcia *et al.*, 1992; Ko *et al.*, 1993; Bacmeister *et al.*, 1995; Summers *et al.*, 1997]. While empirical 'fixed transport' models provide a somewhat simpler framework for studying the atmospheric chemical response to various perturbations, interactive models have an advantage in that they can compute the feedback between chemistry and transport. They can therefore simulate future chemical, radiative, and dynamical changes induced by chlorine loading and other anthropogenic perturbations. Interactive models may ultimately be needed to fully understand the effects caused by such perturbations. However, they do not at present completely resolve all details of the observed zonal mean temperature and zonal wind fields. This point also has implications for 2D model parameterizations of eddy transport processes which can be quite sensitive to the model representation of the zonal mean flow. Most if not all interactive models also have a limitation in that they do not account for the effects of synoptic scale waves which are important in and around the tropopause region and in the very lower stratosphere.

In the present study, we have developed an upgraded empirical transport algorithm. This utilizes several quantities derived from observations: zonal mean temperature, zonal wind, net heating rates, and Eliassen-Palm flux diagnostics for planetary and synoptic scale waves. We also account for the effects of gravity waves and equatorial Kelvin waves by incorporating the parameterizations mentioned above in which the zonal mean flow is constrained to observations. These quantities are then used to derive self-consistent residual circulation and diffusion fields. The unique approach here is that we have incorporated these wave parameterizations and explicit diagnostic quantities into one comprehensive, empirically-based transport scheme. Such a scheme should be able to resolve more of the details of middle atmospheric transport compared to our previous empirically-based algorithms.

We have recently used this new transport algorithm in the GSFC 2D chemistry model to study seasonal and long-term changes in stratospheric ozone [Jackman *et al.*, 1996] and mesospheric water vapor [Chandra *et al.*, 1997], and to study stratospheric tracer correlations [Dessler *et al.*, 1998]. We have also used the model in several international assessment studies of stratospheric ozone, including the World Meteorological Organization (WMO), the Intergovernmental Panel on Climate Change (IPCC), and NASA's Atmospheric Effects of Stratospheric Aircraft Program (AESPA). In conjunction with these assessments, we have participated in the Models and Measurements II intercomparison project (MMII) [Park *et al.*, 1999] in which diagnostic tests have been performed separately on the model transport and chemistry components.

The purpose of this paper is to provide a detailed description and validation of



the new transport algorithm. We will show model simulations of standard long-lived tracers ( $\text{CH}_4$ ,  $\text{H}_2\text{O}$ , and total ozone) compared with observations. This will help assess how well the new model resolves the general zonal mean transport processes in the middle atmosphere. More recent emphasis has been put on model assessments of potential long term ozone changes due to perturbations in the lower stratosphere. Such perturbations include anthropogenic chlorine loading [WMO, 1995]; the injection and dispersion of volcanic aerosols [e.g., Solomon *et al.*, 1996; Jackman *et al.*, 1996]; and the projected emissions of supersonic aircraft [e.g., Stolarski *et al.*, 1995]. Since these ozone simulations are greatly influenced by the model dynamics in the lower stratosphere, we will address more detailed aspects of the transport in this region. This will include model/measurement comparisons of inert radioactive tracers carbon-14 and strontium-90, age of air derived from  $\text{SF}_6$ , and the propagation of seasonal cycles in water vapor and  $\text{CO}_2$ .

## 2. GSFC-2D Model

The 2-D model at NASA/Goddard Space Flight Center (GSFC) was originally described in Douglass *et al.* [1989], and extended to mesospheric heights by Jackman *et al.* [1990]. The model has recently undergone significant development in several areas, including improvements in the method of computing the photolytic source term and the photolysis of  $\text{O}_2$  [Jackman *et al.*, 1996]. We have also recently updated the model reaction rates and photolysis cross sections to the Jet Propulsion Laboratory (JPL) 1997 recommendations [DeMore *et al.*, 1997]. Improvements to the model transport algorithm were summarized in Jackman *et al.* [1996]. In this paper, we present a thorough analysis of the new transport fields and comparisons with observations. A detailed description of the transport formulation and methodology are contained in the Appendix. We note that the transport has undergone some minor changes since the recent MMII intercomparison project, so that the results shown here will differ somewhat from those presented in the MMII publications [Park *et al.*, 1999; Hall *et al.*, 1998].

In section 3.2, we present model simulations of  $\text{H}_2\text{O}$  compared with observations. Our method for computing water vapor was previously described [Fleming *et al.*, 1995], and is briefly summarized here. Photochemical production and loss follows the JPL-97 recommendations. We specify a boundary condition at 660 mb that varies in latitude and season based on the water vapor climatology of Oort [1983]. We include a loss due to rainout throughout the troposphere which is based on the model climatological temperature field. This rainout loss is inversely proportional to the temperature, and is largest at the tropical tropopause. There is also a loss due to the sedimentation of ice particles formed by heterogeneous chemical processes [Considine *et al.*, 1994].



### 3. Results

We will now examine the spatial structure and seasonal evolution of several model simulated tracer fields and show comparisons with observations. We will first show  $\text{CH}_4$ ,  $\text{H}_2\text{O}$ , and total ozone from our standard model which has been run for 20 years to obtain a seasonally repeating steady state simulation. We will then show results from time dependent simulations of  $\text{CO}_2$ ,  $\text{SF}_6$ , and radioactive products of atmospheric nuclear bomb tests, carbon-14 and strontium-90, to illustrate more detailed aspects of the model transport in the upper troposphere and lower stratosphere. We will also compare our new model simulations with those using the previous version of the model transport to illustrate how the new algorithm improves the tracer simulations.

#### 3.1. Methane

Figure 1 shows latitude-height sections of methane from the model simulation (solid) and observations (dashed). Here, we use the combined climatology compiled by Randel *et al.* [1998] based on data from the Halogen Occultation Experiment (HALOE) and the Cryogenic Limb Array Etalon Spectrometer (CLAES) instruments aboard the Upper Atmosphere Research Satellite (UARS). Here, the CLAES data have been used to fill in the high latitude regions during winter where HALOE does not obtain measurements. This climatology has been averaged using potential vorticity (PV) as a horizontal coordinate and then mapped to equivalent latitude (the latitude of an equivalent PV distribution arranged symmetrically about the pole - see Randel *et al.* [1998] for details). This averaging procedure increases the effective latitudinal coverage of the data. Results are similar to standard latitude averaging except at high northern latitudes during winter and spring when the vortex can be significantly displaced from the pole.

The structure and seasonal variations of the model compare qualitatively well with the data. Characteristic dynamical features are evident, such as the isolation of the tropics and the well mixed surf-zone region of the winter subtropics and midlatitudes. The fact that the simulated gradients in the tropics and subtropics compare reasonably well with the data supports the use of the HRDI wind data to derive the model wave driving and diffusion quantities in this region (section A.2.a). The comparison in Figure 1 also shows some discrepancies. For example, the absolute values of  $\text{CH}_4$  in the model tend to be underestimated in the middle and upper stratosphere. A similar difference was noted in comparisons between the HALOE+CLAES climatology and the MACCM2 general circulation model [Waugh *et al.*, 1997]. At high latitudes, the model captures the isolation of the southern hemisphere (SH) vortex in July and October in the lower and middle stratosphere. By contrast in the upper stratosphere, flat tracer gradients illustrating strong horizontal mixing into the polar region are evident during October in both the data and model (the 300 ppbv contour). Note also that high latitude descent during autumn in the upper stratosphere is evident in both hemispheres. Small  $\text{CH}_4$  values characteristic of mesospheric air extend down to 35-40 km in both the model and data.



The model shows some differences at high northern latitudes, which can be more clearly seen in the month-height cross sections in Figure 2. Here, the northern hemisphere (NH) has been shifted by 6 months to facilitate the visual comparison of the polar regions during winter and spring. In both hemispheres, descent within the vortex is indicated by the steady decline of the observed  $\text{CH}_4$  isopleths from autumn through early spring, followed by a sharp increase indicating the spring break-up of the polar vortex and mixing in of midlatitude air. However, the model does not fully resolve the observed low values of  $\text{CH}_4$  within the northern polar vortex. This is not surprising since this region experiences large longitudinal variability. This variability is accounted for in the equivalent latitude mapping of the data, but is not resolved with the standard zonal mean model formulation. In contrast, the southern polar region typically exhibits less variability, so that the model agrees fairly well with the data in this region in Figures 1 and 2.

Figures 3 and 4 provide a heuristic illustration of the processes that control the long lived tracer distributions in the stratosphere. Figure 3 shows the standard model  $\text{CH}_4$  distribution in color for January and September, overlaid with streamlines depicting the residual circulation. Upward motion is present in the tropics throughout the year, providing the advective flux of mass from the troposphere to the stratosphere. Strong descent is evident in the winter polar region of both hemispheres, with ascent in the summer upper stratosphere. The summer lower stratosphere in both hemispheres is characterized by very weak vertical motion. Figure 4 shows the same  $\text{CH}_4$  distributions in the solid contours, with the model  $K_{yy}$  values overlaid in color. Weak mixing is evident in the tropics and summer hemisphere, except for the very lower summer stratosphere where decaying baroclinic wave activity from the troposphere generates mixing below 20 km. Strong mixing is seen in the surf zone region of both hemispheres (20° to 50°), which is reflected in the flat gradients of the  $\text{CH}_4$  field. In the winter polar regions, the mixing is stronger in the NH compared with the SH, reflecting the hemispheric asymmetries in planetary wave activity. Note also the minimum in mixing at 60°S in September extending from ~20 to 40 km. This coincides with the maximum in  $\bar{u}$  at the vortex edge and results in sharp horizontal tracer gradients with much larger values of methane outside compared to inside the vortex.

Referring back to Figure 1, the UARS data for April shows the well-known 'double-peaked' structure at low latitudes in the upper stratosphere. This feature is associated with the meridional circulation induced by the SAO and is most pronounced during the NH spring. This characteristic is also seen in the month-latitude sections of the data and model  $\text{CH}_4$  at 2.2 mb (Figure 5). The model, which utilizes the Kelvin wave parameterization discussed in section A.2.c, captures the overall time evolution and phasing seen in the observations, but has weaker gradients compared to the data. Similar findings were reported in other modeling studies of the SAO using climatological data [Choi and Holton, 1991], and results from the NCAR MACCM2 [Randel *et al.*, 1994; Waugh *et al.*, 1997]. Choi and Holton [1991] discuss the possible limitations of simulating the strength of the SAO circulation using climatological data as is done here.



### 3.2. Water vapor

Figure 6 shows latitude-height sections of  $\text{H}_2\text{O}$  from the model simulation (solid) and UARS observations (dashed). In the stratosphere and lower mesosphere, we use the combined climatology compiled by Randel *et al.* [1998]. This is based on data from HALOE augmented with data from the Microwave Limb Sounder (MLS) in the polar regions. As was done for  $\text{CH}_4$ , the  $\text{H}_2\text{O}$  climatology is mapped in equivalent latitude coordinates. For the mesosphere above 60 km, Figure 6 includes HALOE version 18  $\text{H}_2\text{O}$  data for October 1991 through December 1996 averaged in standard latitude coordinates. Again the model reproduces the overall structure and seasonal variations seen in the data. Mixing ratios in lower tropical stratosphere are  $\sim 3\text{-}4$  ppmv, consistent with the flux of dry air into the stratosphere from the tropical tropopause. The oxidation of methane causes the water vapor concentrations to increase with height above the lower stratosphere, to a maximum of 6-7 ppmv in the summer upper stratosphere and lower mesosphere.

The seasonal variation of  $\text{H}_2\text{O}$  in the equatorial lower stratosphere is shown in Figure 7. Here we show the HALOE data for 1993-1995, along with the model climatological simulation repeated for every year with no interannual variations. The model qualitatively captures the annual cycle at the tropical tropopause. Dry (moist) air enters the stratosphere during the NH winter (summer), coincident with the coldest (warmest) tropopause temperatures. This seasonal variation is advected slowly upwards by the residual circulation, and maintains its structure for a long time period because of the weak horizontal and vertical diffusion characteristic of the tropical lower stratosphere [e.g., Mote *et al.*, 1996]. In the upper stratosphere above 35 km, the model indicates a semiannual cycle which is generally consistent with the HALOE data. The model amplitudes are underestimated relative to HALOE, although the signature in the data is contaminated by interannual variability not represented in the model. This semiannual feature is related to the SAO circulation which brings down water vapor-rich air from the lower mesosphere during the equinoxes. The model circulation and the accompanying signature in the tracers tend to be a bit more apparent during March-April than September-October, which is consistent with observations indicating that the SAO circulation is stronger during the NH spring [e.g., Holton and Choi, 1988] (see also Figures 1 and 5).

The lower stratospheric seasonal signal is more readily seen in the quantity,  $2\text{CH}_4 + \text{H}_2\text{O}$  (defined as  $\hat{H}$  as in Mote *et al.* [1998]), which is quasi-conserved since the chemical destruction of methane produces two molecules of water vapor. Figure 8 again shows that the model qualitatively reproduces the characteristics of the data, with the signal extending up to above 10 mb. The amplitude and phase lag based on Fourier analysis of the annual harmonic of this signal are shown in Figure 9. Here, the quantities plotted are relative to those at the tropical tropopause. The model phase lag variation with height shows good agreement with the data, with an average phase propagation of about .31 mm/sec between 100 and 10 mb. However, the model amplitude is attenuated faster with increasing altitude than observed. This discrepancy was characteristic of the



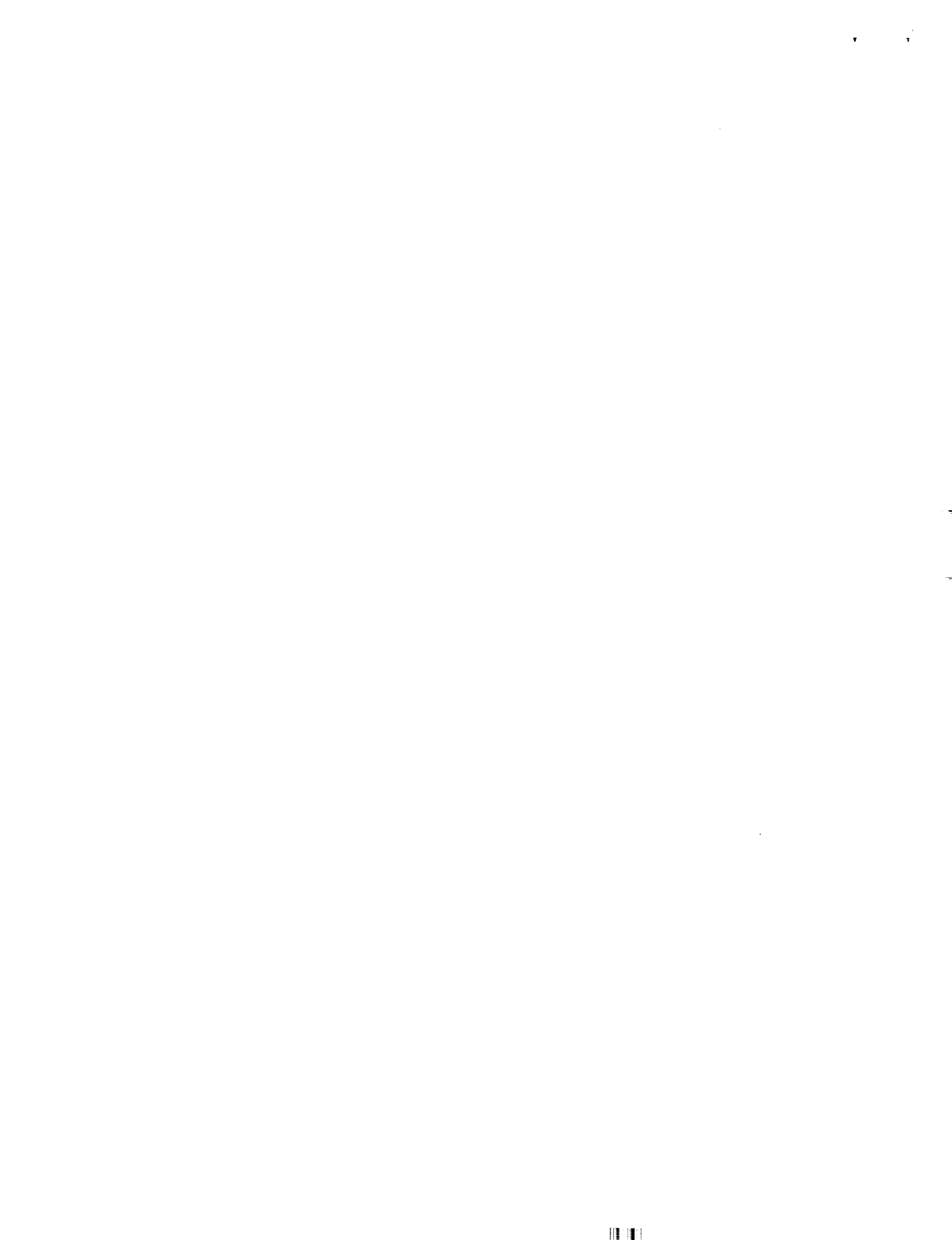
various models analyzed in the MMII intercomparisons [Hall *et al.*, 1998].

To understand the transport processes that affect the seasonal signal propagation in this region, we have plotted our model transport fields in the lower tropical stratosphere in Figure 10. These can be compared with those derived from HALOE data by Mote *et al.* [1998]. Here we present values for the different seasons and the annual average. The annual mean residual vertical velocity ( $\bar{w}^*$ ) is in good agreement with the Mote *et al.* analysis, with a minimum of .22 mm/sec at 19-21 km, increasing with height to about .4 mm/sec at 32 km. The average phase propagation of .31 mm/sec in the model and data for  $\hat{H}$  in Figure 9 generally reflects the average vertical velocity between 16 and 32 km. The minimum  $\bar{w}^*$  at 19-25 km contributes to a slight increase in the vertical gradient of the model phase (i.e., slower propagation) at these altitudes in Figure 9, although this feature is weaker than observed. Consistent with previous findings, the seasonal variations in the lower stratosphere reveal a maximum  $\bar{w}^*$  during NH winter (January), and a minimum during the SH winter (July). This is attributed to the greater extratropical planetary wave driving during the NH winter compared to the SH winter which in turn controls the seasonal variations of the vertical mass flux in the lower tropical stratosphere [e.g., Rosenlof, 1995; Mote *et al.*, 1996]. The seasonal variation in vertical velocity is thought to be responsible for the seasonal variation in temperature in this region, which in turn drives the seasonal signal in water vapor.

The model vertical diffusion rates in Figure 10 also are generally similar to Mote *et al.*, 1998 and the observational analysis of Hall and Waugh [1997b]: values are  $.01\text{-.02 m}^2\text{s}^{-1}$  at 17-29 km, and increase to greater than  $.1\text{ m}^2\text{s}^{-1}$  above 30 km (see Appendix).

To estimate the dilution rate of midlatitude air into the tropics, we computed the annual mean  $K_{yy}$  value averaged over  $35^\circ\text{S}$  to  $35^\circ\text{N}$ , divided by the equator- $35^\circ$  distance squared. The results in Figure 10 reveal a minimum annual mean dilution rate (maximum time scale) near 22 km. This is qualitatively consistent with observational analyses that suggest that the tropics are considerably more isolated from the midlatitudes above about 19 km than below [e.g., Schoeberl *et al.*, 1997; Mote *et al.*, 1998]. Our maximum time scale near 22 km is about 2 years, a bit longer than reported by other previous studies [e.g., Schoeberl *et al.*, 1997; Hall and Waugh 1997b; Randel *et al.*, 1998], but much shorter than the 6-7 year time scale derived by Mote *et al.* [1998]. The seasonal variation in model dilution rates in Figure 10 is consistent with variations in extratropical wave activity. Maximum dilution rates occur during the NH winter (January) and SH late winter-spring (October), with minimum dilution in April and July.

As discussed by Mote *et al.* [1998] and Hall *et al.* [1998], entrainment of midlatitude air is largely responsible for the attenuation of the observed taperecorder signal in the lower tropical stratosphere, although vertical diffusion is also important despite the relatively small values. The observed entrainment is a minimum at 19-25 km which coincides with both the reduced attenuation of the taperecorder signal and the sharp reduction in the vertical gradients of  $\text{CH}_4$  and  $\hat{H}$  observed in this region. Our model simulation noticeably attenuates the seasonal signal faster with increasing altitude than is observed, especially in the 19-25 km region, and shows only a very weak reduction of



the vertical gradients of  $\text{CH}_4$  and  $\hat{H}$ .

Reasons for the model overattenuation of the seasonal signal are unclear. The HALOE data has been noted to underestimate the  $\text{H}_2\text{O}$  annual cycle near the tropopause [e.g., Mote *et al.*, 1996] so that the signal attenuation with height in Figure 9 may be underestimated by HALOE. The model dilution time scales above 20 km are quantitatively consistent with some observational studies, but are significantly shorter than the Mote *et al.* [1998] analysis. To test if the model entrainment rates are too large, we set  $K_{yy}$  to a very small value of  $10^8 \text{ cm}^2 \text{ s}^{-1}$  throughout the year at  $35^\circ\text{S}$  to  $35^\circ\text{N}$  in the lower stratosphere. This corresponds to a dilution time scale of 49 years and implies an extremely isolated tropical region. However, the corresponding amplitude attenuation of the seasonal signal in  $\hat{H}$  was only slightly diminished, and was still significantly greater than observed. This suggests that our model entrainment of midlatitude air in Figure 10 is reasonable. Increasing the model vertical diffusion may effectively reduce the signal attenuation to be closer to observations, however, this will diminish the model-measurement agreement in other areas [Hall *et al.*, 1998]. For example, the phase of the signal will be propagated too quickly and the vertical gradient of the age of air will be decreased (see section 3.5.a, Figure 22). Our model vertical velocity and vertical diffusion rates shown in Figure 10 are in fairly good agreement with the observations so that model discrepancies in these quantities do not seem to significantly contribute to the overattenuation. Numerical diffusion introduced by the advection scheme could artificially damp out the signal, however such diffusion is small in the current scheme [Lin and Rood, 1996]. It is possible that the overattenuation is caused by the relatively coarse vertical resolution of the model (2 km) which may not enable the simulation to properly resolve the propagation of seasonal signals. This possibility will be addressed in future work.

### 3.2.a. Mesospheric Water vapor

Returning to Figure 6, both the model and data show the overall sharp decrease in  $\text{H}_2\text{O}$  with height in the upper mesosphere due to the photo-dissociation by Lyman alpha flux. As a result, seasonal variations in the gravity wave-driven mesospheric meridional circulation are reflected in the water vapor distribution. In the summer extratropics, ascent advects water vapor-rich air upwards from the stratosphere to the upper mesosphere, and wintertime descent brings down dry air from the lower thermosphere. Net photochemical effects are small in winter, and although there is some net photochemical loss of  $\text{H}_2\text{O}$  in the summer upper mesosphere, this effect is not large enough to offset the water vapor increase due to vertical advection. Transport due to vertical diffusion has a secondary effect as discussed below, and horizontal diffusive transport is small in our model simulation.

The seasonal variations of the model and HALOE water vapor at 80 km and 65 km for 3 latitude regions are shown in Figures 11 and 12. At both altitudes, the model captures the overall seasonal variability observed by HALOE. There has been debate over the relative importance of vertical advection and diffusion in controlling the water vapor



distribution in the mesosphere [e.g., Garcia and Solomon, 1985; Holton and Schoeberl, 1988; Smith and Brasseur, 1991; Nedoluha *et al.*, 1996]. A time tendency analysis of our model simulations revealed that throughout most of the mesosphere, vertical advection has a significantly larger influence on  $H_2O$  than does diffusion [Chandra *et al.*, 1997]. However, diffusion does play a secondary role in determining the extratropical seasonal variations seen in Figure 11. Maximum vertical diffusion occurs during the solstices, coincident with the strong westerly and easterly midlatitude mesospheric jets (section A.2.b). This diffusion acts to increase (decrease)  $H_2O$  in the upper (lower) mesosphere. In the upper mesosphere, the diffusive transport therefore enhances the water vapor increase in summer and partially offsets the  $H_2O$  decrease in winter due to vertical advection. This effect maximizes at 80 km, and results in the secondary maxima seen in Figure 11 during mid-winter at midlatitudes. This effect is somewhat more pronounced in the SH winter because the stronger zonal westerlies, and hence the larger difference between the background zonal wind and the gravity wave phase speed ( $\bar{u} - c$ ), allow for larger diffusion compared to the NH winter (section A.2.b). We also note that these secondary maxima are partially generated by the horizontal advection of moist air from the summer to the winter hemisphere induced by the meridional circulation. However, this effect is substantially less than the contribution due to vertical diffusion. At high latitudes,  $\bar{v}^*$ , and hence the horizontal advection, are quite small, so that the secondary mid-winter maxima are due only to vertical diffusion.

At the equator in Figure 11, the model at 80 km shows a dominant semiannual cycle qualitatively similar to the data, although the absolute magnitudes of the model  $H_2O$  are underestimated by 1-1.5 ppmv. Here, the effect from vertical diffusion is small throughout the year, so that the semiannual variation in vertical advection, with maximum upward  $\bar{w}^*$  during the solstices (Figure A.7), controls the water vapor seasonality.

The overall seasonal variations in transport become weaker with decreasing altitude so that the corresponding seasonality in  $H_2O$  is much less pronounced at 65 km in Figure 12. This is especially true at the equator where a rather flat seasonal structure is seen in both the model and HALOE data.

### 3.3. Total Ozone

Our model total ozone simulation and comparison with TOMS version 7 data were reported in Jackman *et al.* [1996]. Since that publication, the simulation has improved somewhat in the southern hemisphere midlatitudes and we provide a summary of our current model-TOMS comparison here. Figure 13 shows the model total ozone for 1990 conditions of total chlorine loading, along with the TOMS data averaged over 1988 to 1992, and the difference (model minus TOMS). Much of the observed seasonal structure is qualitatively simulated by the model, including the on-the-pole maximum of  $\sim 440$  DU during the NH spring and the minimum in the NH autumn; the seasonality in the tropics, with a maximum during October, a secondary maximum during April, and a minimum during the NH winter; the off-the-pole maximum during the southern late



winter-spring; and the very low ozone at the southern pole characterizing the Antarctic ozone hole during spring.

There are some notable discrepancies in the simulation: (1) the model predicts larger amounts of ozone at midlatitudes during summer and early fall, especially in the NH; (2) the magnitude of the simulated southern off-the-pole-maximum is not as large as observed; and (3) the model does not simulate the near elimination of strong latitudinal gradients at high southern latitudes observed following the break-up of the ozone hole. The model also shows noticeably less ozone compared to TOMS at high southern latitudes throughout most of the year. To check if discrepancy (3) is due to an underestimation of horizontal mixing during the spring breakup of the Antarctic vortex, we performed an additional model run with  $K_{yy}$  set to a very large value of  $4 \times 10^{10} \text{ cm}^2 \text{ s}^{-1}$  poleward of  $50^\circ\text{S}$  throughout the lower stratosphere during October and November. However, this gave only a marginal improvement compared to the standard model simulation. This suggests that other deficiencies in the model are causing the larger than observed latitudinal gradients during the austral spring and summer.

### 3.4. Carbon-14 and Strontium-90

The radioactive products of atmospheric nuclear bomb tests, carbon-14 ( $^{14}\text{C}$ ) and strontium-90 ( $^{90}\text{Sr}$ ), are very useful in testing the transport in a model [e.g., Jackman et al., 1991; Prather and Remsberg, 1993; Kinnison et al., 1994].  $^{14}\text{C}$  and  $^{90}\text{Sr}$  were produced in large quantities in the late 1950s and early 1960s by aboveground nuclear tests conducted by the United States and the Soviet Union. These radioactive products were measured extensively by aircraft and balloons sondes in the troposphere and stratosphere [see Kinnison et al., 1994 and references therein]. The measurements after January 1, 1963, are especially important since there were no atmospheric nuclear detonations from 1963 through 1966, and so no excess production of  $^{14}\text{C}$  or  $^{90}\text{Sr}$  needs to be accounted for in model simulations during this time period. There is a natural source of  $^{14}\text{C}$  from galactic cosmic rays which we do not attempt to simulate. All model simulations and measurements shown in this section are the excess  $^{14}\text{C}$  above the natural background state.

The distribution of  $^{14}\text{C}$  from 1963 through 1966 is dependent primarily on the transport processes of the stratosphere and troposphere as  $^{14}\text{C}$  is in the form of  $^{14}\text{CO}_2$  and acts like a passive tracer. The half-life of  $^{14}\text{C}$  is 5730 years and provides a negligible loss over this time period. The distribution of  $^{90}\text{Sr}$  in the middle 1960s is dependent on both the transport processes of the stratosphere and troposphere and the settling velocity of aerosol particles since  $^{90}\text{Sr}$  rapidly coalesces onto these particles. The half-life of  $^{90}\text{Sr}$  is 28 years and provides only a very small loss over this time period.

The initial conditions for  $^{14}\text{C}$  and  $^{90}\text{Sr}$  input into our model were taken from Prather and Remsberg [1993] and their latitude and altitude dependent distributions were specified on October 15, 1963, and on October 15, 1964, respectively. Time and hemisphere dependent ground boundary conditions for  $^{14}\text{C}$  and latitude and altitude dependent settling velocities for  $^{90}\text{Sr}$  were also specified from Prather and Remsberg



[1993].

Our time-dependent simulation of  $^{14}\text{C}$  is shown in Figure 14 for the months of January and July in years 1964, 1965, and 1966. The peak at middle to high latitudes persists through July 1965 although the model transport moves the enhanced  $^{14}\text{C}$  in the tropical lower stratosphere up through the middle (January 1965) and upper (July 1965) stratosphere before being totally dissipated (January 1966). Strong gradients in the Northern lower stratosphere between the tropics and extra-tropics persist through January 1966 indicating the very slow transport and mixing that takes place in this region. The final distribution shown in July 1966 is similar to that of a long-lived source gas (see  $\text{CH}_4$  in Figure 1), except the largest amounts of  $^{14}\text{C}$  are found in the upper stratosphere with smaller amounts at lower altitudes. It thus takes about 3 years for a primarily Northern Hemisphere lower stratospheric source distribution of a substance to become relatively well mixed throughout the stratosphere.

Detailed comparisons between the model and measurements at  $31^\circ\text{N}$  are shown in Figure 15. Also shown are model results from an older version (designated "1995 Model") as well as the present version of our model transport (designated "1998 Model"). The "1998 Model" is clearly an improvement over the "1995 Model" during the period of the  $^{14}\text{C}$  simulation. The  $^{14}\text{C}$  peak between 20 and 25 km and the very large gradient between 10 and 20 km in the measurements are represented much better by the "1998 Model."

We also show comparisons of  $^{90}\text{Sr}$  between the two versions of our model and the measurements at two latitudes,  $9^\circ\text{N}$  and  $34^\circ\text{S}$ , in Figures 16 and 17, respectively. At both of these latitudes in which the atmospheric transport characteristics are substantially different, it is apparent that the "1998 Model" simulates the  $^{90}\text{Sr}$  more realistically than the "1995 Model." The two model simulations especially diverge from one another in late 1965. The very excellent agreement between the "1998 Model" and the measurements in October 1966 is probably somewhat fortuitous, given that the real atmosphere undergoes interannual dynamical variability that is not contained in our '1998 Model' transport. It is significant, however, that the modeled  $^{90}\text{Sr}$  generally simulates the gradual decrease of measured stratospheric  $^{90}\text{Sr}$  over 1965 and 1966, while representing the peak concentration at 20-25 km in a very reasonable manner.

There are substantial differences between our "1998 Model" and "1995 Model" transport algorithms which are reflected in these  $^{14}\text{C}$  and  $^{90}\text{Sr}$  simulations. While the advective transport by the mean circulation exhibits some differences, most of the changes seen in Figures 15-17 are due to changes in the meridional and vertical diffusive transport. The "1998 Model" is generally less diffusive in a globally averaged sense. However more importantly, the sharp changes in diffusion that occur across certain atmospheric regions are much better resolved in the "1998 Model". These include the changes in vertical mixing across the tropopause, and the changes in horizontal mixing between the tropics and subtropics in the stratosphere.



### 3.5. Sulfur hexafluoride

$\text{SF}_6$  is a nearly inert anthropogenically-produced tracer. It has had a relatively steady source at the ground over the past 2-3 decades, allowing for a quasi-linear temporal increase in atmospheric concentration [e.g., Geller *et al.*, 1997]. The time lag of  $\text{SF}_6$  between a given point in the stratosphere and a reference location at the ground determines the mean age of air,  $\Gamma$  [Elkins *et al.*, 1996; Harnisch *et al.*, 1996]. This has become a widely used diagnostic of model transport [e.g., Hall and Plumb, 1994; Waugh *et al.*, 1997; Bacmeister *et al.*, 1998; Hall *et al.*, 1998]. The annually averaged  $\Gamma$  derived from  $\text{SF}_6$  is very similar to the mean age determined from the first moment of the age spectrum in model simulations [Hall and Plumb, 1994; Hall and Waugh, 1997a; Hall *et al.*, 1998]. However, seasonal variations of the age determined from  $\text{SF}_6$  can be significant.

Our model simulation of  $\Gamma$  determined from  $\text{SF}_6$  for various seasons is shown in Figure 18. Here we have taken the area weighted global mean value at the surface as the reference point. In the troposphere, the vertical gradients are quite small due to the rapid vertical mixing, and there is a 1-1.5 year time lag between midlatitudes of the northern and southern hemispheres. This interhemispheric exchange time is in good agreement with  $\text{SF}_6$  measurements [e.g., Harnisch *et al.*, 1996; Geller *et al.*, 1997] and largely results from the tropospheric horizontal diffusion imposed in the model (see section A.2.a). The very lower stratosphere exhibits sharp vertical gradients in age due to the drastic reduction in vertical mixing across the tropopause into the lower stratosphere. The age of air contour shapes in the stratosphere are qualitatively similar to other long lived tracers (e.g.,  $\text{CH}_4$ , Figure 1), consistent with the mean circulation. The youngest stratospheric air occurs just above the tropical tropopause (about .6 years older than the global mean surface value), with the oldest air of  $\sim 6$  years occurring in the mesosphere and polar winter upper stratosphere. The mean age in the mesosphere is relatively uniform owing to the vigorous meridional circulation and vertical mixing characteristic of this region. The older ages seen in the polar stratosphere in fall and winter are indicative of the descent of older mesospheric air within the polar vortex. As expected, this feature is more pronounced in the SH where, relative to the NH, the polar vortex is more isolated from the younger mid-latitude air. The isolation of the SH polar region in the lower stratosphere persists into October, as indicated by the small 5.5 year isopleth centered at 50 mb at the south pole in Figure 18d. This is also reflected in the  $\text{CH}_4$  simulation in Figure 1d.

Observations of  $\Gamma$  can be made in certain regions using measurements of  $\text{SF}_6$  from aircraft [Elkins *et al.*, 1996], balloons [Harnisch *et al.*, 1996; Patra *et al.*, 1997; Moore *et al.*, 1998], and the space shuttle [Rinsland *et al.*, 1993]. Mean ages can also be derived from  $\text{CO}_2$  measurements after taking into account the annual cycle in  $\text{CO}_2$  at the ground and a small correction for  $\text{CH}_4$  oxidation [e.g., Boering *et al.*, 1996]. Ages derived from  $\text{CO}_2$  in this way were found to be similar to those derived from  $\text{SF}_6$  data [Waugh *et al.*, 1997; Hall *et al.*, 1998].

Figure 19 shows the mean age for October/November 1994 (top) and Jan-



uary/February 1996 (bottom) computed from three model simulations at 20 km compared with that derived from SF<sub>6</sub> data at 19-21 km taken onboard several NASA ER-2 flights [Elkins *et al.*, 1996]. The global mean surface time series of Geller *et al.* [1997] is used as the reference point for the SF<sub>6</sub> measurements. Note that in deriving  $\Gamma$  from both the model and observations, we have not accounted for the small nonlinear effect in the time increase of SF<sub>6</sub>. This effect slightly increases the mean age compared to the simple time lag method, with the difference approaching .5 years for  $\Gamma$  of  $\sim$ 6 years [Volk *et al.*, 1997]. However, for the present analysis we are mainly interested in the relative differences in  $\Gamma$  between the model and measurements.

The base '1998 Model' simulation (solid line) in Figure 19 captures much of the latitudinal variation seen in the data, including the sharp gradient between the equator and  $\pm 20^\circ$ . Ages near the equator are  $\sim$ 1.5 years in both the model and data. The model-data agreement of the low-latitude gradients supports the use of the HRDI wind data to derive the model wave driving and diffusion quantities in the tropics (section A.2.a). While there is a fairly large spread in the observations at middle and higher latitudes, the model  $\Gamma$  tends to be a little younger than observed, especially in January/February 1996. For example near 50°N, during January/February 1996, the mean of the data is about 5 years whereas the model indicates about 4 years. Underestimation of  $\Gamma$  is a characteristic seen in most stratospheric models [Hall *et al.*, 1998].

Figure 20 shows vertical profiles of  $\Gamma$  from three different model runs for the various latitudes and seasons indicated. These are plotted along with  $\Gamma$  derived from the balloon SF<sub>6</sub> data of Harnisch *et al.* [1996] (asterisks and squares) and the Observations of the Middle Stratosphere campaign (OMS) [Moore *et al.*, 1998] (triangles). Again we have used the global mean value at the surface [Geller *et al.*, 1997] as the reference function for the data. This gives stratospheric ages that are .25 to 1 year younger compared to ages derived using the NH tropospheric reference function used by Harnisch *et al.* [1996]. At low to middle latitudes, the standard '1998 model' (solid line) shows good agreement with the observations, including the transition from very weak vertical gradients in the troposphere to much stronger gradients in the lower stratosphere. The data generally indicate a transition to little or no vertical gradient above about 25 km, and the '1998 model' qualitatively reproduces this feature in most of the comparisons. At midlatitudes above  $\sim$ 22 km, the model agrees well with the data at 44°N but not as well at 35°N. These data show age differences of about 1 year in the middle stratosphere, even though they are at similar latitudes and seasons (September). The data were taken during different years (1996 versus 1993), so some of the difference may be due to interannual dynamical variability effects which are not contained in the model. At high latitudes, the model agrees well with the late winter observations in March taken outside of the polar vortex at 68°N (Figure 20h, squares), and the summer observations at 65°N (Figure 20e). The model also shows a region of reduced vertical age gradients at 10-15 km in the summer profile at 65°N which is somewhat indicated in the data. However, the model did not capture the very old air (8-10 years) observed inside the vortex above 20 km at 68°N in mid-winter (Figure 20g) and late winter (Figure 20h, asterisks).



Figures 19-20 also show the mean age from our previous '1995 Model' version (dotted line) which was discussed in the  $^{14}\text{C}$  and  $^{90}\text{Sr}$  simulations (section 3.4). Relative to the observations and the '1998 model' simulation,  $\Gamma$  from the '1995 model' is significantly underestimated, and the associated latitudinal gradient is much flatter. The vertical gradients in the lower stratosphere (Figure 20) are also generally weaker than observed. This is consistent with the '1995 Model' simulation of  $^{14}\text{C}$  and  $^{90}\text{Sr}$  (section 3.4) and reflects the overly diffusive nature of this previous model transport.

While these model simulations assume  $\text{SF}_6$  is an inert tracer, it is possible that  $\text{SF}_6$  incurs a small photo-chemical loss in the mesosphere. If such a loss exists it would effectively increase the model  $\Gamma$  to be older than the base simulations shown above. To test this, we included a loss identical to  $\text{C}_2\text{ClF}_5$  (CFC-115) in our '1998 Model' simulation in Figures 19-20 (dashed line). CFC-115 photolytic losses are taken from DeMore *et al.* [1997] and result in a lifetime of about 600 years in our model. Significant increases in the model age occur at middle and high latitudes, and at the higher altitudes in the tropics when including this mesospheric loss. At 20 km (Figure 19),  $\Gamma$  is generally .5 to 1 year older at middle to high latitudes, with ages increased by nearly 2 years at the SH pole during spring. This latter result reflects the mesospheric character of air within the SH vortex, even at levels reaching down to the lower stratosphere. Including the mesospheric loss has increased  $\Gamma$  in the mid-stratosphere by 1 year at low latitudes, 2 years at middle latitudes, and 3 years at high latitudes (Figure 20).

Overall, the model  $\Gamma$  is in better agreement with the data at the higher altitudes and latitudes when including this mesospheric loss, although the comparison is not as good at  $44^\circ\text{N}$  (Figure 20f). The comparisons inside the NH vortex are also improved, however, the model still underestimates the observations by 1 to 2 years (Figure 20g, Figure 20h, asterisks). We note that a loss rate comparable to CFC-115 is considered a probable upper limit and is shown here primarily as a qualitative example of how such a loss could effect  $\Gamma$ . Differences between the base model simulation and observations could reflect other limitations of the model such as the grid resolution. Furthermore, discrepancies within the NH polar vortex are probably due to the fact that the vortex is frequently centered off the pole and exhibits large year to year variability and as such cannot be resolved by the current zonal mean climatological model formulation. In contrast, the model does a reasonable job in resolving the SH vortex (Figure 1c-d, Figure 18c-d) which has smaller longitudinal and interannual variability.

### 3.5.a. Age of air sensitivity to $K_{zz}$

An important transport component in 2D models is the vertical eddy diffusivity ( $K_{zz}$ ). In the mesosphere, diffusion coefficients can be determined from gravity wave parameterizations [e.g., Lindzen, 1981], which provide for reasonably good long lived tracer simulations (section 3.2.a, see also Garcia *et al.* [1985]). Determination of  $K_{zz}$  in the upper troposphere and lower stratosphere is very important for proper treatment of the tropopause boundary and troposphere-stratosphere exchange processes. In this region of our model, we scale  $K_{zz}$  based on the vertical temperature gradient, so that



a stronger lapse rate, indicative of more rapid convective overturning, implies a larger value of diffusion. This methodology implies a large mixing rate in the troposphere, and a very small  $K_{zz}$  in the lower stratosphere, with a sharp gradient across the tropopause boundary (see section A.2.d). We specify a lower limit on  $K_{zz}$  of  $.01\text{--}.02\text{ }m^2\text{s}^{-1}$  in the lower stratosphere following the observational analyses of Hall and Waugh [1997b] and Mote *et al.* [1998].

An evaluation of the lower stratospheric vertical diffusion specified in models was recently made by Hall *et al.* [1998]. These authors discussed the influence of  $K_{zz}$  on the propagation of seasonal signals in the tropics and concluded that a value of  $K_{zz} < .1\text{ }m^2\text{s}^{-1}$  is most realistic. Here, we illustrate the sensitivity of the model global distribution of  $\Gamma$  to the lower stratospheric minimum in  $K_{zz}$ . This will help to evaluate the qualitative realism of the current model  $K_{zz}$  field.

Figures 21-22 show the mean age from the base '1998 model' simulation along with the SF<sub>6</sub> observations as in Figures 19-20. We also include two additional model scenarios in which the lower stratospheric minimum  $K_{zz}$  is increased to  $.1\text{ }m^2\text{s}^{-1}$  and  $1\text{ }m^2\text{s}^{-1}$ , respectively, but are otherwise identical to the base '1998 model'. Increasing the minimum rate of vertical mixing reduces the mean age throughout the stratosphere. Increasing the minimum to  $.1\text{ }m^2\text{s}^{-1}$  decreases  $\Gamma$  only slightly in the tropical lower stratosphere, but the difference increases to as much as .5 years in the lower stratosphere extratropics and in the middle stratosphere at all latitudes.

With a minimum of  $1\text{ }m^2\text{s}^{-1}$ ,  $\Gamma$  is significantly younger everywhere compared to observations and the base model scenario. Maximum differences of 3 years occur at middle and high latitudes in the middle stratosphere. In addition, both the vertical and horizontal gradients in mean age are drastically reduced in this model run. This unrealistic scenario is far outside the range of the observations, and is similar to the 'diffusive regime' discussed by Hall *et al.* [1998] in their analysis of seasonal signal propagation. Although the model scenario with the minimum  $K_{zz}$  set to  $.1\text{ }m^2\text{s}^{-1}$  is within the observational values of  $\Gamma$ , the overall model-measurement agreement is not as good relative to the base model case. This provides evidence that a minimum  $K_{zz}$  of  $.01\text{--}.02\text{ }m^2\text{s}^{-1}$  gives the most realistic model simulation, as is suggested by the analyses of Hall and Waugh [1997b] and Mote *et al.* [1998]. Our model-measurement comparisons of CH<sub>4</sub> also reveal that a minimum  $K_{zz}$  of  $.01\text{--}.02\text{ }m^2\text{s}^{-1}$  gives the best simulation.

### 3.6. Carbon dioxide

The source of carbon dioxide at the ground includes a large secular trend of  $\sim 1.4\text{ ppmv/yr}$  along with a large biosphere-induced seasonal cycle. This seasonal variation is largest at high northern latitudes and is strongly latitude dependent. At stratospheric levels, CO<sub>2</sub> is nearly inert: it has no photochemical loss, and has only a small production from CH<sub>4</sub> oxidation. The transport characteristics of the stratosphere are therefore reflected in the propagation of the CO<sub>2</sub> seasonal cycle. As shown in previous observational analyses, this signal originates at the tropical tropopause and propagates vertically in the tropics with a gradual loss of amplitude, similar to the



observed behavior of  $\hat{H}$ . The CO<sub>2</sub> signal is also transported rapidly poleward with only a small decrease in amplitude just above the tropopause. At higher altitudes (above  $\sim 460$ K,  $\sim 19$  km) the midlatitude signal is very small, indicating that the barrier to poleward transport from the tropics becomes increasingly strong with height [Strahan *et al.*, 1998; Mote *et al.*, 1998]. Simulation of these characteristics in CO<sub>2</sub> therefore provides a diagnostic of model transport.

Our time dependent model simulation of CO<sub>2</sub> uses lower boundary conditions based on monthly mean global surface observations for 1979 to 1995 [Conway *et al.*, 1994]. The simulation was continued through 1996 by using the 1995 boundary conditions and adding 1.4 ppmv. To account for the small CO<sub>2</sub> source from CH<sub>4</sub> oxidation, the simulation includes the corresponding time dependent surface boundary conditions of CH<sub>4</sub> [WMO, 1995] and is run with all model photo-chemistry included.

Figure 23a-b shows the model simulated annual cycle amplitude of CO<sub>2</sub>, defined as one-half of the difference from peak to trough of the seasonal variation, and the corresponding phase. The amplitude maximizes at the ground in the northern hemisphere extratropics ( $\sim 7.5$  ppmv), and decreases equatorward and with increasing height in the troposphere. The phase in the troposphere is fairly uniform in the tropics and northern hemisphere, reflecting the strong horizontal and vertical mixing of the region. In the lower stratosphere, the amplitude attenuates with height and a strong phase shift is seen with increasing latitude and altitude away from the tropical tropopause.

Previous studies have shown that the seasonal cycle in CO<sub>2</sub> in the northern hemisphere midlatitude lower stratosphere is propagated from the tropics and not from the underlying troposphere [e.g., Strahan *et al.*, 1998]. Figure 24 shows the model simulation at 55°N for five pressure levels increasing in altitude from the middle troposphere to the lower stratosphere. There is a dramatic decrease in amplitude and an increase in phase lag between 282 and 212 mb, illustrating a distinct difference in the airmass characteristics of the troposphere and lower stratosphere. This was also seen in the sharp gradient in amplitude and phase across the tropopause in Figure 23, and suggests that the model reasonably simulates the separation between the troposphere and stratosphere.

Comparisons of the model simulation in certain regions of the stratosphere can be made with CO<sub>2</sub> observations from the ER-2 field campaigns [Boering *et al.*, 1996; Strahan *et al.*, 1998]. We first examine the simulation at the tropical tropopause which essentially is the boundary condition for CO<sub>2</sub> entering the stratosphere. Figure 25 shows time series of the model simulation (solid line) and observations for 1992 through 1996. Here, the observations are taken as the average of the surface time series at Mauna Loa (19°N) and Samoa (14°S) with a two month time lag (dashed line). This time series gives an excellent fit to the ER-2 CO<sub>2</sub> data just above the tropical tropopause (triangles), and therefore provides a proxy for the stratospheric CO<sub>2</sub> boundary condition [Boering *et al.*, 1996]. The model agrees fairly well in phase, lagging the observations by about 1-2 weeks. However, the model amplitude is underestimated by roughly a third (1.2 vs. 1.8 ppmv). While the model captures the observed maxima



fairly well, the amplitude discrepancy is due primarily to the model underestimating the observed minima. We note that at lower altitudes, the model exhibits a significantly larger CO<sub>2</sub> amplitude than seen in Figure 25, and at least part of the deficiency around the tropopause is due to the coarse vertical resolution (2 km) of the model. Because of this resolution, we must ramp down  $K_{zz}$  to very small values starting in the very upper troposphere ( $\sim 15$  km) to avoid spurious transport across the tropical tropopause (section A.2.b). In reality, this region experiences large vertical mixing, and so the seasonal CO<sub>2</sub> signal is propagated through the tropopause with a larger amplitude than is simulated by the model. Future versions of the model with improved resolution should provide better simulations of the region around the tropopause.

To check the propagation of the CO<sub>2</sub> seasonal cycle throughout the lower stratosphere, Figure 26 compares the model simulation (bottom row) with time series representing the ER-2 data at several latitudes and levels adapted from Strahan *et al.* [1998] (top row). These curves are least squares fits to a combination of the estimated stratospheric input seasonal cycle (the delayed Mauna Loa-Samoa average in Figure 25) and the observed linear trend at stratospheric midlatitudes. The data are binned by N<sub>2</sub>O for the range of potential temperature ( $\Theta$ ) values indicated (370-410K, 395-435K, 440-480K), and for three latitude ranges: tropics (6°S-12°N), subtropics (12°S-30°N), and midlatitudes (30°S-48°N). The model values represent the averages for the same latitude and theta ranges used for the observations. In all three latitude regions, the observations show similar amplitudes in the lower two theta ranges. At the top level, the data show some amplitude attenuation in the tropics, with much more attenuation with increasing latitude so that little seasonal signal is seen at midlatitudes at 440-480K. The data also show a general increasing phase lag with increasing altitude and latitude.

The model simulation in Figure 26 shows an underestimation of amplitude at all levels and latitudes. This is due in large part to the underestimation of the signal amplitude entering the stratosphere (Figure 25) which then biases the model simulation throughout the stratosphere. Nevertheless, the simulation shows some qualitative consistency with the observations and illustrates that the model reproduces the general characteristics of seasonal cycle propagation. For example in the tropics and subtropics, the model and data show an increasing phase lag and amplitude attenuation with height. At midlatitudes, the model shows very good qualitative agreement with the observations: very similar amplitudes and phases are seen in the bottom two levels, with the top level showing almost no seasonal amplitude. At the lowest level (370-410K), the model compares well with the observations in simulating very similar amplitudes and phases in the tropics and subtropics (Figure 27), illustrating strong coupling of these regions. The midlatitude data at 370-410K show some amplitude attenuation and phase delay relative to the tropics and subtropics, and these features are reasonably captured by the model, although more amplitude attenuation is simulated than observed.

Referring back to Figure 23a, somewhat surprising features are the simulated amplitude maxima at middle and high latitudes of both hemispheres centered near 16 km. At these altitudes and latitudes, the seasonal cycle due to the CO<sub>2</sub> source has been completely attenuated. However, descent within the polar vortices during winter and



early spring advects down relatively low CO<sub>2</sub> values, creating a late winter/early spring minimum and hence a significant seasonal cycle amplitude. This effect maximizes at the poles, and is evident at 15-20 km where there is a substantial vertical gradient in CO<sub>2</sub>. Above 20 km, there is little vertical gradient in CO<sub>2</sub> so that the downward motion has little effect. This feature was not indicated in previous model simulations of the CO<sub>2</sub> seasonal cycle [Hall and Prather, 1993; Waugh *et al.*, 1997; Strahan *et al.*, 1998]. This feature would also be difficult to isolate in the ER-2 data given the limited temporal coverage of the current observations. Furthermore, this feature does not seem to be related to the annual cycle in the CO<sub>2</sub> source, so that extracting information from the data by fitting a tropospheric annual cycle and trend as was done by Strahan *et al.* [1998] would not seem to be justified in this case.

Figures 28 and 29 compare vertical profiles of the ER-2 and model CO<sub>2</sub> for different months in the tropics, northern midlatitudes, and high southern latitudes. Here, CO<sub>2</sub> is plotted against potential temperature, which acts as a vertical coordinate similar to pressure. The secular trend in CO<sub>2</sub> is apparent in the observations, and is captured fairly well by the model (e.g., Figures 28a,f). The tropical data in Figure 28 show the vertical propagation of the CO<sub>2</sub> seasonal cycle [Boering *et al.*, 1996] which is repeated from year to year. A maximum is observed just above the tropical tropopause (380-400K) during August, and progresses to higher levels during October through December. A minimum is seen near 380K during October and at 430-440K during February. The model shows some indication of this signal propagation, however, the amplitude is significantly underestimated, as was seen in Figure 26. As shown in Figure 25, the model underestimates the CO<sub>2</sub> seasonal signal entering the stratosphere by roughly a third. However, Figure 28 suggests that relative to the observations, the model further overattenuates the amplitude with increasing height in the tropical lower stratosphere. A similar deficiency was seen in the propagation of the seasonal cycle of 2CH<sub>4</sub> + H<sub>2</sub>O (Figure 9).

At middle and high latitudes (Figure 29), the vertical variations of the model show general agreement with the observations. Both the model and data indicate a larger decrease with height at midlatitudes compared to either the tropics or high latitudes. The large amount of scatter seen in the observations of CO<sub>2</sub> and Θ in Figure 29 can be explained by the fact that in the extratropics, air parcels originate from a wide range of airmass types due to the inherent large dynamical variability. And unlike CO<sub>2</sub>, potential temperature is conserved for time scales of only 2-3 weeks at most in the lower stratosphere. Therefore, CO<sub>2</sub> and Θ do not exhibit a high correlation in these regions. Furthermore, these data reflect variations in transport for a particular year that will not be resolved by our climatological model. However in the tropics, air parcels on a given theta (or pressure) surface have a limited distribution of air mass origins, so that CO<sub>2</sub> and Θ form a compact relationship [e.g., Boering *et al.*, 1996]. To reduce the variability due to transport in the extratropics, it is useful to plot CO<sub>2</sub> using N<sub>2</sub>O as the vertical coordinate [Boering *et al.*, 1996; Strahan *et al.*, 1998], as shown in Figure 30. In the lower stratosphere, both CO<sub>2</sub> and N<sub>2</sub>O are very long lived and form a compact relationship, unlike CO<sub>2</sub> and Θ. The tropospheric source of N<sub>2</sub>O is seasonally invariant



and undergoes only a small secular increase which is contained in our model simulation. Therefore, variations in CO<sub>2</sub> for a given value of N<sub>2</sub>O will be independent of the seasonal variations in transport, and will be due only to the seasonal cycle and trend of the CO<sub>2</sub> source.

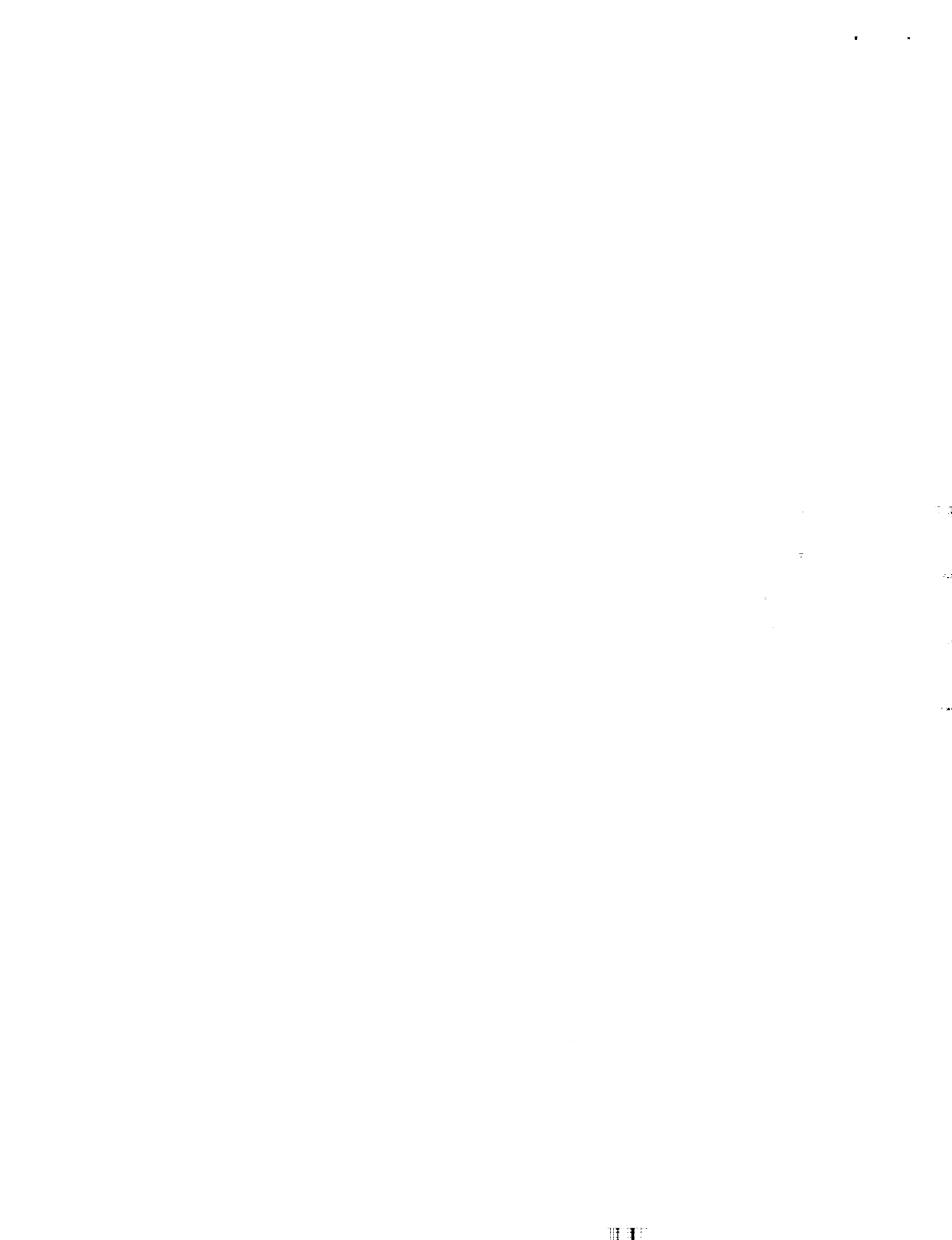
The model CO<sub>2</sub> – N<sub>2</sub>O relationship shows good overall consistency with the data. Note the observed CO<sub>2</sub> maximum at N<sub>2</sub>O = 300 ppbv during October/November 1995 is qualitatively simulated by the model, although with reduced magnitude. This feature probably reflects the separation between tropospheric air at the lowest altitudes (highest N<sub>2</sub>O concentrations), and stratospheric air above. A notable discrepancy in Figure 30 appears at the high southern latitudes where the model consistently underestimates the vertical CO<sub>2</sub> gradient at low N<sub>2</sub>O values. This results in too much CO<sub>2</sub> being simulated by the model at these upper levels, a deficiency which occurs throughout the year. At these altitudes and latitudes, the seasonal cycle is almost completely attenuated so that CO<sub>2</sub> exhibits only a secular increase. The model-measurement difference may therefore be due to inadequacies in the model photochemistry such that, 1) the N<sub>2</sub>O loss rates are too large; 2) the production of CO<sub>2</sub> from CH<sub>4</sub> oxidation is overestimated, and/or 3) there is an additional stratospheric loss of CO<sub>2</sub> not accounted for in the model.

#### 4. Conclusions

We have developed a new empirically-based transport algorithm for use in our GSFC two-dimensional transport and chemistry model. To derive the transport fields, the algorithm utilizes empirically based zonal mean zonal wind, temperature, diabatic and latent heating rates, E-P flux diagnostics for planetary and synoptic scale waves, and parameterizations to account for the effects due to gravity waves and equatorial Kelvin waves. As such, this scheme utilizes significantly more information compared to our previous algorithm which was based only on zonal mean temperatures and heating rates.

To validate this new transport, we have presented extensive model-measurement comparisons of several long lived tracers. The model captures much of the qualitative spatial and seasonal variability seen in satellite and aircraft observations. These include the isolation of the tropics and the well mixed surf-zone region of the winter sub-tropics and mid-latitudes. The fact that the simulated tracer gradients in the tropics and subtropics agree fairly well with the observations supports the validity of using the HRDI wind data to derive the model wave driving and diffusion quantities in this region. At high latitudes, the model captures the general isolation of the southern polar vortex in winter and early spring, but does not adequately resolve the NH polar vortex. In the tropical upper stratosphere, the simulated double peaked structure in CH<sub>4</sub> associated with the SAO is similar in phase, but is significantly weaker in amplitude compared to observations. This deficiency is consistent with other previous model studies.

The model total ozone field captures much of the observed seasonal and latitudinal variability seen in the TOMS data. A major discrepancy occurs in the middle to high southern latitudes in which the model does not resolve the spring break-up of



the Antarctic ozone hole and subsequently maintains larger than observed latitudinal gradients during the southern high latitude summer. Sensitivity tests reveal that this deficiency is not due to an underestimation of horizontal mixing during the break-up of the southern polar vortex, and points to other processes that are not accurately resolved in the model.

In the mesosphere, the model simulated  $H_2O$  also shows good agreement with HALOE data. The model reveals that the seasonal water vapor changes are controlled primarily by vertical advection by the meridional circulation. Vertical diffusion induced by gravity wave breaking is less important, consistent with the findings of Holton and Schoeberl [1988]. However, diffusion does generate a secondary  $H_2O$  maximum during mid-winter, which is somewhat more pronounced in the southern hemisphere.

We performed several diagnostic tests of the model transport emphasizing the region below 35 km. Simulations of carbon-14 and strontium-90 reproduced the observed peak in mixing ratio at 20-25 km, and the decrease with altitude in mixing ratio above 25 km. The simulated mean age from  $SF_6$  reveals that the oldest air of around 6 years occurs in the high latitude upper stratosphere during fall and early winter. The latitudinal and vertical gradients of the simulated mean ages compare well with aircraft and balloon observations outside of the northern hemisphere polar winter vortex. Including a mesospheric loss rate identical to that of CFC-115 (corresponding to a  $\sim 600$  year atmospheric lifetime) in the  $SF_6$  simulation increased the age of air by as much as 3 years in the high latitude middle stratosphere, and provided better overall agreement with the balloon data above 20 km.

The fact that the model significantly underestimates (by 3-5 years above 25 km) the NH vortex observations of very old air of 8-10 years seems to be inconsistent with the reasonably good model-measurement agreement at other latitudes. Even when including the mesospheric loss for  $SF_6$ , the model mean age at high northern winter latitudes still underestimates the observations by as much as 2 years. Some underestimation of the model  $\gamma$  in this region is expected given the model underestimation of the isolation of the NH vortex seen in the  $CH_4$  comparison (Figure 2). The model does qualitatively show the greater isolation of the SH vortex, as indicated in the various simulations and the fact that the mean age is .75 years older in the SH than the NH at 20 km. If the observations indicating mean ages of 8-10 years within the NH vortex are accurate, the significant model underestimation of  $\gamma$  in this region probably reflects the limitations of the current zonal mean climatological model formulation. Such a model would not be able to resolve the large longitudinal and interannual variability characteristic of the NH polar regions during winter and early spring.

The propagation of the seasonal signal in carbon dioxide from the tropical lower stratosphere to midlatitudes is qualitatively reproduced by the model, and the model simulates the observed near-absence of seasonal variability at higher levels at midlatitudes. However, simulations of both  $CO_2$  and  $\hat{H}$  show that the model attenuates the seasonal signals too rapidly with altitude in the tropics, a characteristic that is consistent among many stratospheric models. We found that the model reproduces the observed altitudinal variation of horizontal entrainment of midlatitude air into



the tropics reported in several studies [e.g., Schoeberl *et al.*, 1997; Mote *et al.*, 1998]. Furthermore, the vertical phase propagation of  $\hat{H}$  and the vertical gradient of the mean age are both consistent with the observations. These results, along with various sensitivity tests, suggest that the overattenuation of the seasonal signal cannot be explained by an over-estimation of the horizontal in-mixing, or the explicit vertical diffusion contained in the model. The numerical advection scheme exhibits small numerical diffusion [Lin and Rood, 1996], so that this would have only a small effect on the signal degradation. It is possible that the signal over-attenuation is caused in large part by the coarse vertical and horizontal model resolution (2 km by 10° latitude). The model with such resolution cannot sufficiently resolve and propagate the seasonal cycles so that the amplitudes are effectively reduced.

We found that the circulation in the upper troposphere and stratosphere is determined by a combination of the empirically determined heating rates, wave drive, and the bottom boundary condition in the lower troposphere. Changes in this circulation will affect methane, total ozone, and the mean age in a consistent manner. For example, an overly strong circulation will overestimate (underestimate) CH<sub>4</sub> at low (high) latitudes, with the opposite tendency in total ozone, and produce a mean age that is too young at all latitudes. Obtaining reasonable model-measurement agreement in these tracers simultaneously at different latitudes and seasons gives confidence that the circulation is fairly consistent with the real atmosphere. Furthermore, the simulations with the new transport formulation are in substantially better agreement with observations compared to our previous model transport. Taken together, these model-measurement tracer comparisons therefore provide a rigorous test of the new model transport, and enable us to provide better model ozone simulations for a variety of scientific and assessment studies.

**Acknowledgments.** The authors would like to thank S.J. Lin for many helpful discussions concerning the numerical advection scheme, M. Burrage for supplying the HRDI level 2 wind data, J. Harnisch for supplying the balloon SF<sub>6</sub> data, S. Strahan for supplying the seasonal cycle fits of the CO<sub>2</sub> data, and for helpful discussions concerning the data, K. Boering for supplying the tropical tropopause CO<sub>2</sub> data, and B. Randel for supplying the UARS climatologies of CH<sub>4</sub> and H<sub>2</sub>O. J. Elkins??? We also thank the NASA Atmospheric Chemistry Modeling and Analysis Program and the UARS Science Investigation Program for support of this project.



## Appendix: GSFC 2-D Model Transport Description

Earlier versions of the GSFC 2-D model transport algorithm derived the residual meridional and vertical velocities ( $\bar{v}^*$ ,  $\bar{w}^*$ ) from the TEM thermodynamic and continuity equations. This formulation used empirically determined climatological temperatures and heating rates and neglected the eddy heating terms. This was essentially the diabatic circulation, as based on Dunkerton [1978], and assumed that horizontal temperature advection by the circulation was small. This assumption is reasonable in the stratosphere, but may not be applicable in the mesosphere where meridional velocities can be large. This approach was somewhat different from other studies that derived the diabatic circulation by iterating the continuity and thermodynamic equations to obtain a converged solution [Shine, 1989; Huang and Smith, 1991, Eluszkiewicz et al., 1996]. In the previous GSFC model versions, the mean residual velocities along with the empirical zonal mean wind field were used in the zonal mean momentum equation to obtain the Eliassen-Palm (E-P) flux divergence, or equivalently, the eddy flux of potential vorticity (PV) taken as the residual needed for momentum balance. The  $K_{yy}$  field was then determined self-consistently as the ratio of the eddy PV flux to the latitudinal gradient of zonal mean PV [Newman et al., 1988; Fleming et al., 1995]. These circulation and diffusion fields were able to capture some of the general features seen in long-lived tracer observations. However, because the transport was based only on zonal mean temperatures and heating rates with no explicit planetary or gravity wave effects included, many detailed observational features reflecting zonal mean transport were not resolved in the model simulated tracer fields.

Our new methodology generally follows that of other interactive 2-D models [e.g., Brasseur et al., 1990; Garcia et al., 1992; Bacmeister et al., 1995] as originally formulated by Garcia and Solomon [1983], and includes explicit calculations of the various wave effects. However, the new dynamical fields are based on pre-determined empirical data sets, as opposed to being computed interactively in the model. Note that as with previous model versions, the transport is climatological and does not account for the quasi-biennial oscillation or any other interannual variability.

### A.1. Zonal Mean Formulation

Following the methodology originally outlined in Garcia and Solomon [1983], a meridional streamfunction ( $\bar{\chi}^*$ ) is calculated to obtain the TEM residual circulation ( $\bar{v}^*$ ,  $\bar{w}^*$ ). To derive an equation for the streamfunction, we use the zonal mean momentum, thermodynamic, and mass continuity equations of the TEM system [e.g., Andrews et al., 1987],

$$\frac{\partial \bar{u}}{\partial t} - \bar{v}^* \left( f + \frac{\bar{u} \tan \phi}{a} - \frac{\partial \bar{u}}{a \partial \phi} \right) + \bar{w}^* \frac{\partial \bar{u}}{\partial z} = F_{PW} + F_{GW} + F_{KW} \quad (1)$$

$$\frac{\partial \bar{T}}{\partial t} + \bar{v}^* \frac{\partial \bar{T}}{a \partial \phi} + \bar{w}^* \left( \frac{\partial \bar{T}}{\partial z} + \frac{\kappa \bar{T}}{H} \right) = Q_D + Q_L + Q_{PW} + Q_{GW} \quad (2)$$

$$\frac{1}{a \cos \phi} \frac{\partial (\bar{v}^* \cos \phi)}{\partial \phi} + \frac{1}{\rho} \frac{\partial (\bar{w}^* \rho)}{\partial z} = 0 \quad (3)$$

where the scale height ( $H$ ) is taken to be 7 km, and the other symbols have their usual meanings. Here, mechanical forcing is taken as the E-P flux divergence due to dissipating



planetary waves ( $F_{PW}$ ), gravity waves ( $F_{GW}$ ), and equatorial Kelvin waves ( $F_{KW}$ ). We have not included a term accounting for unresolved motions, e.g., as represented by a weak Rayleigh frictional drag, given the uncertainties involved. Thermal forcing is due to the combined effects of the net diabatic heating ( $Q_D$ ), latent heating ( $Q_L$ ), and the net eddy heat flux associated with planetary waves ( $Q_{PW}$ ) and gravity wave breaking in the mesosphere ( $Q_{GW}$ ). Equations (1) and (2) are combined using the thermal wind relation,

$$f_1 \frac{\partial \bar{u}}{\partial z} = -\frac{R}{H} \frac{\partial \bar{T}}{a \partial \phi}, \quad f_1 = f + \frac{2\bar{u} \tan \phi}{a}. \quad (4)$$

This eliminates the time derivatives (assuming  $\bar{u}_z \partial f_1 / \partial t$  is negligible), and along with continuity yields a single diagnostic equation for  $\bar{\chi}^*$ ,

$$C_{zz} \frac{\partial^2 \bar{\chi}^*}{\partial z^2} + C_z \frac{\partial \bar{\chi}^*}{\partial z} + C_{zy} \frac{\partial^2 \bar{\chi}^*}{\partial y \partial z} + C_y \frac{\partial \bar{\chi}^*}{\partial y} + C_{yy} \frac{\partial^2 \bar{\chi}^*}{\partial y^2} + C_0 \bar{\chi}^* = C_F \cos \phi \quad (5)$$

The coefficients ( $C_{zz}, C_z, C_{zy}, C_y, C_{yy}$ , and  $C_0$ ) depend on empirically determined  $\bar{u}$  and  $\bar{T}$  fields (see section A.1.b) and are similar to those derived in Garcia and Solomon [1983]. The forcing term ( $C_F$ ) is proportional to the vertical gradient of the total momentum forcing and the latitudinal gradient of the total heating rate,

$$C_F = f_1 \frac{\partial}{\partial z} (F_{PW} + F_{GW} + F_{KW}) + \frac{R}{H} \frac{\partial}{a \partial \phi} (Q_D + Q_L + Q_{GW} + Q_{PW}) \quad (6)$$

These quantities will be described below. The residual circulation is computed from  $\bar{\chi}^*$  via continuity,

$$\bar{v}^* = -\frac{1}{\cos \phi} \left[ \frac{\partial \bar{\chi}^*}{\partial z} - \frac{\bar{\chi}^*}{H} \right] \quad (7)$$

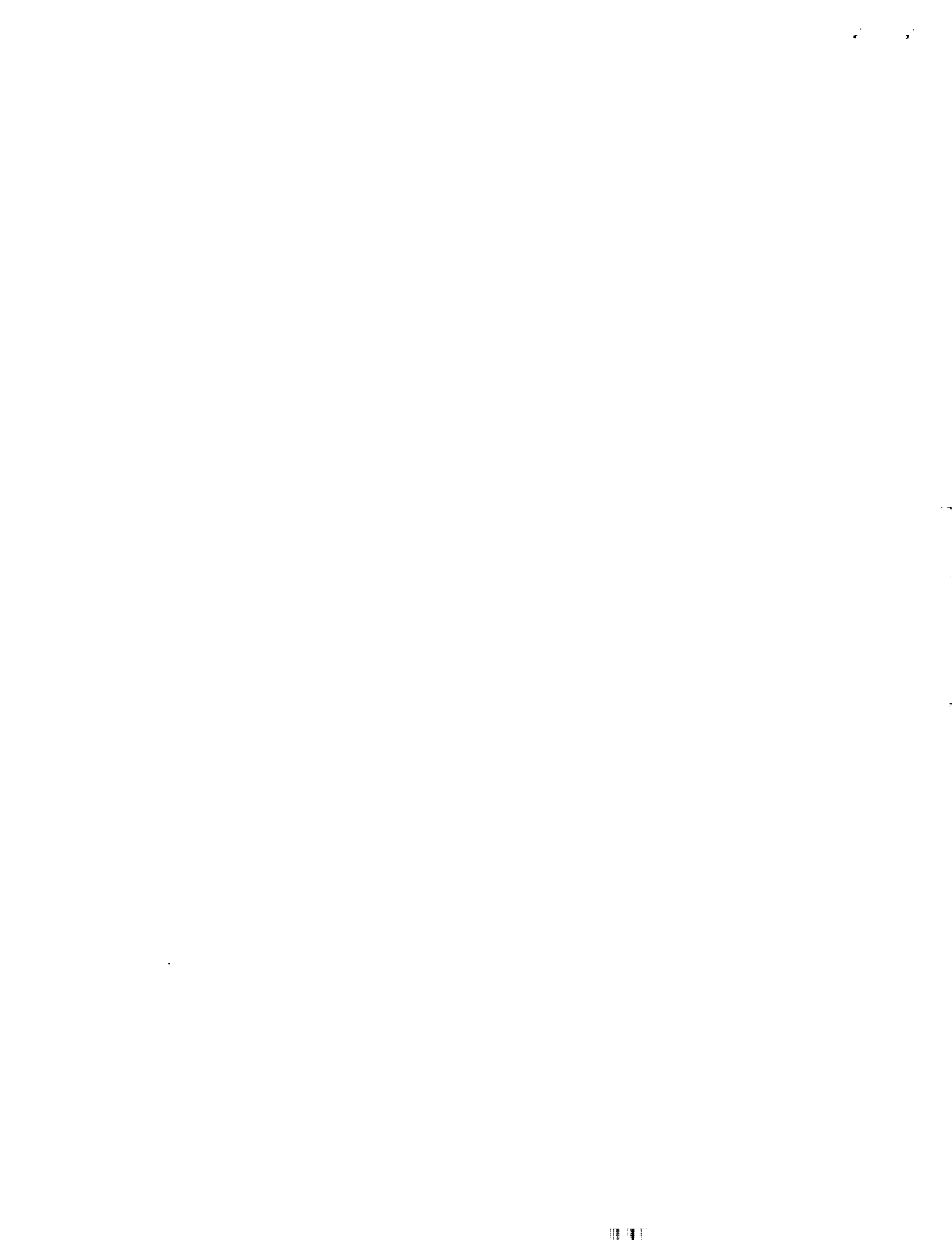
$$\bar{w}^* = \frac{1}{\cos \phi} \frac{\partial \bar{\chi}^*}{\partial y} \quad (8)$$

Note that this formulation satisfies global mass balance such that,

$$\int_{-90^\circ}^{+90^\circ} \rho \bar{w}^* \cos \phi d\phi = 0 \quad (9)$$

This differs from previous calculations of the diabatic circulation in which inaccuracies in the heating rate algorithms and/or input data sets made it necessary to manually adjust  $\bar{w}^*$  to satisfy the condition in (9).

#### A.1.a. Numerical Solution/Boundary Conditions on $\bar{\chi}^*$



To obtain  $\bar{\chi}^*$ , equation (5) was solved in finite difference form by a successive over-relaxation method (identical results were obtained using the method of Lindzen and Kuo [1969]). We used a rectangular latitude-height grid extending from 90°S-90°N at 5° increments, and from the ground to  $\sim 116$  km in log-pressure altitude at approximately 2 km intervals. As discussed below, the top level of the transport model has been raised from the 90 km level used in previous model versions.

For boundary conditions, we treat the model as being bounded by four rigid walls with no flow into or out of the model domain. Therefore,  $\bar{v}^*=0$  at the poles and  $\bar{w}^*=0$  at the ground (1013 mb) and the top boundary. By equations (7) and (8), this implies that  $\bar{\chi}^*=0$  at the four boundaries. While our current chemistry model extends up to 90 km, putting the upper boundary on the dynamics and hence making  $\bar{w}^*=0$  at this level caused unrealistically large values in  $\bar{v}^*$  in the upper mesosphere. To avoid this problem, we extended the upper boundary on the model transport up to 116 km. The heating rates and wave driving were linearly damped down to be zero at this top level. This gave a  $\bar{w}^*$  field that gradually decreased to zero at the top boundary, thereby avoiding any anomalously large jets in the  $\bar{v}^*$  field. In this formulation, the dynamical processes in the region above 90 km are not completely represented and as such this region serves only as a sponge layer for the transport. We therefore only show model results for the 0-90 km region where chemistry is computed.

To obtain reasonable long lived tracer simulations in the stratosphere, we found it necessary to impose an additional boundary condition on  $\bar{\chi}^*$  at one level above the ground (762 mb - denoted as  $\bar{\chi}_2^*$ ). Following Garcia *et al.* [1992], we calculate  $\bar{\chi}_2^*$  as,

$$\bar{\chi}_2^* = -\frac{\cos \phi}{f \rho_2} \int_{z_2}^{\infty} \rho (F_{PW} + F_{GW} + F_{KW}) dz \quad (10)$$

This expression is derived from equation (7) and the linearized steady state momentum equation,  $-fv^* = F_{PW} + F_{GW} + F_{KW}$ , and follows from the downward control principle under quasi-geostrophic scaling [e.g., Haynes *et al.*, 1991; Rosenlof and Holton, 1993]. Equation (10) is applied to latitudes outside of  $\pm 15^\circ$  with values in the tropics interpolated between  $\pm 15^\circ$ . The vertical velocity at 762 mbar obtained from  $\bar{\chi}_2^*$  then depends solely on the momentum forcing of the free atmosphere above this pressure surface. Upward motion out of the boundary layer generally occurs equatorward of  $\pm 50^\circ$  with downward motion into the boundary layer at higher latitudes. We found that the circulation computed using  $\bar{\chi}_2^*$  obtained from (10) was too strong, i.e., too much upwelling (downwelling) in the tropics (high latitudes), as reflected in model-measurement comparisons of CH<sub>4</sub>, total ozone, and the mean age of air (too young at most latitudes). Multiplying the expression in (10) by a constant factor of .75 for all latitudes and seasons produced a somewhat weaker circulation and gave much better model agreement with long lived tracer observations. We therefore used this methodology for all simulations shown throughout this paper. We note that as an independent check of this method, a very similar circulation was obtained by computing  $\bar{\chi}_2^*$  via integration of equation (8) and applying the definition [e.g., Andrews *et al.*, 1987],

$$\bar{w}^* \equiv \bar{w} + \frac{1}{a \cos \phi} \frac{\partial}{\partial \phi} \left[ \cos \phi \frac{\bar{v}' \bar{T}'}{(\partial \bar{T} / \partial z) + \kappa \bar{T} / H} \right] \quad (11)$$



Here, the terms on the RHS of (11) are obtained from climatological averages of the recently reanalyzed NCEP data [Kalnay *et al.*, 1996].

Figure A.1c-d shows  $\bar{w}^*$  and  $\bar{v}^*$  for January. These fields are generally similar to previous model calculations [e.g., Garcia *et al.*, 1992]. Upward motion is seen throughout the tropical stratosphere, and in the extratropical middle to upper stratosphere and mesosphere in summer. Maximum ascent of  $3.6 \text{ cms}^{-1}$  occurs in the polar upper mesosphere. The winter extratropics are characterized by downward motion throughout the troposphere and middle atmosphere. The strong upward motion of the Hadley cell is also evident in the tropical troposphere. The meridional velocities are generally weak in the stratosphere, but reach maximum values of  $6 - 7 \text{ ms}^{-1}$  in the upper mesosphere reflecting the summer to winter meridional flow pattern induced by gravity wave drag.

#### A.1.b. $\bar{u}$ and $\bar{T}$

The zonal mean temperature and zonal wind fields used in the coefficients in equation (5) were compiled as follows. We used zonal mean temperatures based on the 17-year (1979-1995) average of NCEP data for 1000-1 mbar, and the CIRA-86 empirical reference atmosphere [Fleming *et al.*, 1990] for the mesosphere above 1 mbar. Outside the tropics, zonal mean winds were derived from the temperatures via thermal wind balance (equation 4). This derivation is problematic at low latitudes where the Coriolis parameter is small, and in the region above 80 km where the temperature data contained in the CIRA model was rather sparse. Therefore, we used direct wind measurements from the high resolution Doppler imager (HRDI) onboard UARS to obtain  $\bar{u}$  for  $20^\circ\text{S}$ - $20^\circ\text{N}$  in the stratosphere and mesosphere (10-115 km) and at all latitudes above 80 km. We used the HRDI level 2B winds averaged over the period November 1991 to September 1996 which cover the region  $70^\circ\text{S}$ - $70^\circ\text{N}$ . To maintain a constant relative angular velocity at high latitudes, values of  $\bar{u}$  poleward of  $\pm 70^\circ$  were extrapolated by  $\cos \phi$  so that  $\bar{u} \rightarrow 0$  at the poles. The HRDI data also contain a measurement gap at 40-50 km which was filled in by spline interpolation. Above  $\sim 75$  km, the HRDI data at lower latitudes ( $\pm 35^\circ$ ) becomes increasingly aliased by the diurnal tide due to the daytime only measurements. This aliasing was minimized by fitting and subtracting out the tidal mode corresponding to the (1,1) Hough function, expected to be the dominant contribution. This fitting procedure is described by Hays *et al.* [1994] and Burrage *et al.* [1995]. Since HRDI does not make measurements below 10 km, we derived the zonal wind in the equatorial lower-middle troposphere from a second derivative thermal wind calculation. In this formulation,  $\bar{u}$  is proportional to  $(\partial f / \partial y)^{-1}$ , rather than  $f^{-1}$ , thereby avoiding the equatorial singularity problematic of the standard geostrophic wind derivation. This technique has been used in the middle atmosphere with some qualitative success in estimating the directly measured wind [e.g., Fleming and Chandra, 1989; Fleming *et al.*, 1996].

As noted above, the streamfunction formulation necessitates maintaining exact thermal wind balance in all regions. To do this in regions where different temperature and wind data were used, we combined the  $\partial \bar{u} / \partial z$  field computed directly from the HRDI winds with the  $\partial \bar{u} / \partial z$  field implied from the temperatures via thermal wind balance. These quantities were merged together over several latitudes or levels to obtain a smooth transition. Again, we set the constraint that at the poles,  $\bar{u} = 0$  and therefore,  $\partial \bar{u} / \partial z = \partial \bar{T} / \partial y = 0$ . The resulting  $\partial \bar{u} / \partial z$  and the equivalent  $\partial \bar{T} / \partial y$  fields were then re-integrated to obtain  $\bar{u}$  and  $\bar{T}$  fields in thermal wind balance. Figure A.1a-b shows these fields for January and indicates the well



known zonal mean structure during solstice conditions, e.g., the summer easterlies and winter westerlies of the middle atmosphere. These features have been discussed frequently in previous climatological compilations [e.g., Randel, 1992; Fleming *et al.*, 1990].

#### *A.1.c. Heating Rates*

The diabatic heating rates ( $Q_D$ ) are computed following Rosenfield *et al.* [1994], using climatological distributions of zonal mean temperature (section A.1.b), ozone, and water vapor. The ozone climatology was constructed as follows. Values in the troposphere are based on SBUV data as described in McPeters *et al.* [1984]. SAGE II data (both sunrise and sunset) averaged over 1984-1989 are used in the lower stratosphere (100-10 mbar). Nimbus-7 SBUV data averaged over 1979-1989 are used for the upper stratosphere (10-0.7 mbar), and SME IR and UV measurements averaged over 1982-1986 are used for the mesosphere above 0.7 mbar. The water vapor climatology is based on Oort [1983] for the troposphere up to 375 mbar and climatologically averaged SAGE II data for the upper troposphere and stratosphere (375-1 mbar). For the mesosphere above 1 mbar, we used the midlatitude reference profile from Remsberg *et al.* [1989] which is independent of latitude and season. For both the ozone and water vapor climatologies, linear interpolation was used to fill in data gaps. For data-void regions at polar latitudes, data were extrapolated by maintaining a constant value poleward from the highest latitude available. Values were blended over 2-3 levels where there was overlapping data, thereby obtaining a smooth transition between the original data sources.

The net diabatic heating rates for January are shown in Figure A.2. These values are generally consistent with previous heating rate calculations that utilize climatological data [e.g., Shine, 1989; Huang and Smith, 1991; Newman and Rosenfield, 1997], and UARS observations [Eluszkiewicz *et al.*, 1996]. Net diabatic heating (cooling) is seen in regions where the observed temperature is colder (warmer) than the radiative equilibrium temperature. Largest cooling occurs in the winter extratropics due to planetary and gravity wave effects, with the latter being dominant in the mesosphere. Gravity wave breaking drives the summer mesosphere to be far colder than the radiative equilibrium temperature, leading to large net diabatic heating there. Small net diabatic cooling occurs throughout the troposphere during all seasons. Largest values are  $\sim 1.5$  K/day which occur in the tropical mid-troposphere.

For the latent heating rates ( $Q_L$ ), we have used the empirical climatology compiled by Newell *et al.* [1974]. The January latent heating is shown in Figure A.3a (note that this plot is only for the troposphere, 1000-100 mb). Largest latent heating of  $\sim 2.5$  K/day occurs in the tropical mid-troposphere coincident with tropical convective systems, with minima observed in the high latitude regions.

Gravity wave breaking in the mesosphere induces a net thermal flux due to the combination of an eddy heat flux convergence and the turbulent diffusion of the mean thermal field [Schoeberl *et al.*, 1983; Huang and Smith, 1991]. The time tendency due to the eddy heat flux convergence is expressed as,

$$\frac{\partial \bar{T}}{\partial t} = \dots - \frac{1}{\rho} \frac{\partial}{\partial z} \left[ \rho \bar{w'} \bar{T'} \right] - \frac{\kappa}{H} \bar{w'} \bar{T'} = - \frac{N^2 C_v}{2 R C_p} \left( \frac{\alpha (\bar{u} - c)^2}{N^2} + K_{zz} \right) = Q_{GW1} \quad (12)$$

where  $\kappa = R/C_p$ ,  $c$  is the gravity wave phase speed,  $\alpha$  is the Newtonian cooling rate



associated with the radiative damping of the waves, and  $K_{zz}$  is the vertical eddy diffusion coefficient computed from the gravity wave breaking parameterization described in section A.2.b. Consistent with Huang and Smith [1991], our calculations show that the first term in parentheses in equation (12) is quite small compared to the turbulent diffusion term. The total quantity,  $Q_{GW1}$  in (12), is shown in Figure A.3b for January. Net cooling is seen throughout the mesosphere, with largest values of  $\sim 4.5$  K/day occurring in the regions of largest diffusion in the upper mesosphere (see Figure A.5d).

Turbulent diffusion of the mean thermal field is expressed as,

$$\frac{\partial \bar{T}}{\partial t} = \dots + \frac{(\kappa - 1)}{H} \left[ K_{zz} \left( \frac{\kappa \bar{T}}{H} + \frac{\partial \bar{T}}{\partial z} \right) \right] + \frac{\partial}{\partial z} \left[ K_{zz} \left( \frac{\kappa \bar{T}}{H} + \frac{\partial \bar{T}}{\partial z} \right) \right] = Q_{GW2}. \quad (13)$$

This quantity is shown in Figure A.3c for January and can contribute to either a net heating or cooling depending on the vertical distribution of temperature and diffusivity. For January, net cooling is seen throughout most of the mesosphere with a maximum of -11 K/day in the summer mid-latitudes near 80 km. Smaller regions of net heating on the order of +1-2 K/day occur in the middle mesosphere at mid-latitudes of both hemispheres. The total contribution of breaking gravity waves to the thermodynamic budget (equation 2) and used in the streamfunction (equations 5-6) is then  $Q_{GW} = Q_{GW1} + Q_{GW2}$  shown in Figure A.3d. The total net contribution of gravity wave breaking is cooling throughout almost the entire mesosphere. A maximum of -12.5 K/day occurs at 80-90 km in the mid-latitude SH during January.

Planetary waves also induce a net thermal flux [e.g., Andrews *et al.*, 1987] which enters into the streamfunction equations (5)-(6) as,

$$Q_{PW} = -\frac{(\kappa - 1)}{H} \left[ \bar{v}' \bar{T}' \frac{\partial \bar{T}}{\partial y} \frac{\partial \bar{T}}{\partial z} \right] - \frac{\partial}{\partial z} \left[ \bar{v}' \bar{T}' \frac{\partial \bar{T}}{\partial y} \frac{\partial \bar{T}}{\partial z} \right] \quad (14)$$

The eddy terms in (14) are taken from 3-D meteorological fields as discussed in section A.2.a. The quantity  $Q_{PW}$  (figure not shown) is small compared to the other heating rate contributions. Maximum values are generally less than  $\pm .75$  K/day occurring in the high latitude winter stratosphere-lower mesosphere, and the mid-high latitude troposphere throughout the year.

The total heating rate for January is shown in Figure A.4. Diabatic heating/cooling dominates the total throughout the stratosphere, with the gravity wave effects playing a significant role in the mesosphere along with the diabatic contribution. Both the diabatic and latent heating are important in the troposphere, and the combination of these processes leads to horizontal gradients in the total heating rate which determines the classical Hadley cell circulation in the tropical troposphere and lower stratosphere (Figure A.1c).

## A.2. Wave Parameterizations

### A.2.a. Planetary and Synoptic Scale Waves

Planetary wave dissipation generates rapid irreversible mixing of tracers which can be expressed as a horizontal diffusive transport in two-dimensional models. This wave dissipation



also induces a drag on the zonal mean flow which can modify the mean advective transport by the meridional circulation. Previous investigations have illustrated the importance of accounting for these processes in a self-consistent manner [Newman *et al.*, 1988; Garcia, 1991].

The E-P flux divergence computed from 3-dimensional meteorological analyses provides a diagnostic estimate of the planetary wave drag ( $F_{PW}$  in equation 1). This quantity is defined as [e.g., Andrews *et al.*, 1987],

$$F_{PW} = \frac{1}{\rho a \cos \phi} \left[ \frac{1}{a \cos \phi} \frac{\partial (F_\phi \cos \phi)}{\partial \phi} + \frac{\partial F_z}{\partial z} \right] \quad (15)$$

where,

$$F_\phi = \rho a \cos \phi \left[ \frac{\partial \bar{u}}{\partial z} \frac{R}{H} \frac{\overline{v' T'}}{N^2} - \overline{v' u'} \right], \quad (16)$$

$$F_z = \rho a \cos \phi \left[ \left( f - \frac{1}{a \cos \phi} \frac{\partial (\bar{u} \cos \phi)}{\partial \phi} \right) \frac{R}{H} \frac{\overline{v' T'}}{N^2} \right] \quad (17)$$

Following Randel and Garcia [1994], horizontal mixing rates can then be calculated self-consistently as the ratio of the E-P flux divergence to the latitudinal gradient of zonal mean potential vorticity,

$$K_{yy} = -F_{PW} / \bar{q}_y \quad (18)$$

where,

$$\bar{q}_y = \frac{2\Omega \cos \phi}{a} - \frac{1}{a^2} \frac{\partial}{\partial \phi} \left[ \frac{1}{\cos \phi} \frac{\partial (\bar{u} \cos \phi)}{\partial \phi} \right] - \frac{f^2}{\rho} \frac{\partial}{\partial z} \left[ \frac{\rho}{N^2} \frac{\partial \bar{u}}{\partial z} \right] \quad (19)$$

This formulation follows from the flux-gradient relationship [e.g., Newman *et al.*, 1988],  $\overline{v' q'} = -K_{yy} \bar{q}_y$ , where the E-P flux divergence is taken as the zonal mean PV flux for quasi-geostrophic planetary waves.

For the troposphere and stratosphere, we have derived climatological E-P flux divergence and  $K_{yy}$  quantities from equations (15)-(19) using 17 years (1979-1995) of daily 3-dimensional NCEP analyses for 1000-1 mb. This computation includes the wave dissipation and induced mixing due to both thermal damping and wave breaking. To account for the effects from both planetary and synoptic scale waves in the troposphere and very lower stratosphere, we include zonal wavenumbers 1-12 from the ground to 10 mb. Above this level, zonal waves 1-6 are included since only the planetary scale waves are important in this region.

For the zonal and meridional velocities in (15)-(19), balanced winds were computed from the NCEP geopotential height analyses for regions poleward of  $\pm 20^\circ$  [Randel, 1992]. To deal with the problem of deriving winds in the tropics, we computed balanced winds at the equator from the NCEP height fields using a second derivative calculation analogous to that used for the zonal mean wind as described in section A.1.b. Winds between  $\pm 20^\circ$  and the equator were interpolated by the cosine of latitude to minimize the latitudinal gradient across the equator and thereby maintaining inertial stability. Previous studies have shown that this technique



produces a  $\bar{u}$  field that is in general qualitative agreement with radiosonde, rocketsonde and HRDI data in the phasing of the QBO and SAO. However, the derived wind magnitudes were generally underestimated compared with the direct wind measurements [Fleming and Chandra, 1989; Fleming *et al.*, 1996]. We found that deriving the equatorial eddy winds in this manner underestimated the E-P flux and eddy diffusion magnitudes. This was evident in the simulated long lived tracer fields that exhibited significantly larger latitudinal gradients in the tropics compared to UARS observations. We also found that using tropical eddy winds from the UKMO data assimilation system provided only a marginal improvement in the simulated tracer fields. Instead, we utilized HRDI zonal and meridional wind measurements for the calculations between  $\pm 20^\circ$ . To avoid a bias caused by the QBO, we used HRDI data for January 1992 to May 1996 corresponding to 2 complete QBO cycles. Because of data gaps and the limited longitudinal coverage obtained with daily HRDI data, we used monthly mean HRDI winds and the corresponding monthly mean NCEP temperatures to compute the quantities in equations (15)-(19) between  $\pm 20^\circ$ . Using monthly mean data accounts for the stationary wave components but not the transient eddy contributions. However, the HRDI-derived E-P flux divergence and  $K_{yy}$  values were larger than those derived from the NCEP or UKMO winds. The resulting tropical-subtropical gradients in the tracer fields were weaker and in significantly better agreement with observations compared with the NCEP or UKMO-based derivations (see Figures 1 and 19).

For the mesosphere above 1 mbar (up to  $\sim 85\text{km}$ ), we compute the E-P flux divergence and eddy mixing from the CIRA-86 stationary planetary wave climatology [Barnett and Labitzke, 1990]. This contained monthly mean geopotential height and temperature values for zonal waves 1-2 which are based on data from the Nimbus-6 Pressure Modulator Radiometer (PMR) for 1975-1978. As in the stratosphere, balanced winds were used for the wind velocities poleward of  $\pm 20^\circ$ , with the second derivative balanced wind calculation used in the tropics. Unlike the stratosphere, we did not use the HRDI data for the tropical winds in the mesosphere since using different time periods for the temperatures (1975-1978) and winds (1992-1996) was thought to be unsatisfactory for the calculations in equations (15)-(19). Values of  $F_{PW}$  above 85 km were linearly damped down with altitude to be zero at 116 km. Future E-P flux calculations for the mesosphere will use both wind and temperature data from UARS as these retrieval algorithms mature.

Consistent with previous investigations [Robinson, 1986; Newman *et al.*, 1988], our computations of equations (15)-(17) revealed mostly negative areas of E-P flux divergence, but also some positive values, especially at high latitudes. This implies a wave-induced acceleration of the mean flow, and a negative mixing rate via the flux-gradient relationship in (18). While regions of positive values may be caused by limitations of the original data sets, some areas of positive E-P flux may be real, and the implied negative  $K_{yy}$  indicates a breakdown in the assumptions underlying (18). This is also indicative of the ambiguity in interpreting E-P diagnostics for wave propagation and dissipation [e.g., Andrews, 1987; Newman *et al.*, 1988].

To avoid computing negative mixing rates in practice, regions of positive E-P flux divergence were set to zero, implying a zero  $K_{yy}$ . The resultant E-P flux fields were smoothed once in the latitude-height domain before being applied in the calculations for  $\bar{\chi}^*$  and  $K_{yy}$ . To ensure that  $K_{yy}$  computed from (18) remains well behaved, we also apply the criterion that  $\bar{q}_y \geq 0.5 \times 10^{-11} \text{m}^{-1}\text{s}^{-1}$  as suggested by Randel and Garcia [1994]. This avoids negative mixing rates and implies that large positive values of  $K_{yy}$  are caused by eddy processes via



the E-P flux divergence and not by instability of the zonal mean flow as represented by small or negative  $\bar{q}_y$ . To accomodate the one day time step used in the chemistry model, we set an upper  $K_{yy}$  limit of  $5 \times 10^{10} \text{ cm}^2 \text{ s}^{-1}$  which is sufficiently large to accomodate the diffusion induced by planetary and synoptic scale waves.

We impose a very small background  $K_{yy}$  of  $10^8 \text{ cm}^2 \text{ s}^{-1}$  throughout the stratosphere and mesosphere. In the low-middle troposphere, it was necessary to set a large background  $K_{yy}$  of  $2 \times 10^{10} \text{ cm}^2 \text{ s}^{-1}$  to simulate the interhemispheric transit time of 1-2 years estimated from SF<sub>6</sub> and halocarbon data near the ground [e.g., Geller *et al.*, 1997]. This background  $K_{yy}$  was gradually tapered down with altitude to blend with the small  $10^8 \text{ cm}^2 \text{ s}^{-1}$  background value imposed in the stratosphere and mesosphere. Finally, we impose a small  $K_{yy}$  of  $10^8 \text{ cm}^2 \text{ s}^{-1}$  around the tropopause region where the tropopause height changes across adjacent latitudes. This decreased the anomolous cross-tropopause transport and gave better model simulations of water vapor compared with observations in the very lower stratosphere at middle to high latitudes.

We do not include the transport due to the off-diagonal  $K_{yz}$  and  $K_{zy}$  terms in the diffusion tensor which arise from the projection of  $K_{yy}$  from isentropes to pressure surfaces [Newman *et al.*, 1988]. This was done because of the uncertainties in the calculation of  $K_{yz}$  and  $K_{zy}$ , and because these terms represent only a small effect. Note also that to ensure that the diffusion matrix is always positive and diffusive, the relation  $K_{yy}K_{zz} > K_{yz}K_{zy}$  must hold. Neglecting the off-diagonal terms ensures that the total diffusive flux is positive even when imposing the very small  $K_{zz}$  values necessary in the stratosphere.

Figures A.5a and A.5c show latitude-height plots of the climatological E-P flux divergence ( $F_{PW}$ ) and  $K_{yy}$  for January. In the troposphere, large wave driving is evident poleward of  $\pm 20^\circ$  during winter and to a lesser extent, summer, due to synoptic and planetary wave activity. These features are similar in both hemispheres (July not shown). The  $K_{yy}$  values computed from equation (18) reflect this pattern, although they are superimposed on the large background mixing rates which we have specified throughout the troposphere as described above. Large planetary wave driving also occurs in the extra-tropical stratosphere and mesosphere during winter. Consistent with Randel and Garcia [1994], the direct ratio calculation used in (18) gives large mixing rates at high latitudes in the upper stratosphere and lower mesosphere, and also above 100 mb at  $20^\circ$ - $45^\circ$ N coincident with weak  $\bar{q}_y$  in the surf-zone region. This is in contrast to Newman *et al.* [1988] who computed largest mixing rates only at high latitudes using a linear regression fit of  $\bar{v}'\bar{q}'$  and  $\bar{q}_y$  with a zero intercept.

The seasonal variation of  $K_{yy}$  and  $\bar{u}$  at several different levels are shown in Figure A.6a-d (see also Figs. 12-13 in Randel and Garcia [1994]). These plots depict the hemispheric asymmetries in mixing and the zonal mean flow. In the mid-upper stratosphere and mesosphere, weak mixing occurs in the easterly flow regimes of the summer hemisphere and in the tropics, consistent with a minimum of planetary wave activity in these regions. Note that the tropical stratospheric mixing rates based on the HRDI winds are weak but not negligible, with values as large as  $8 \times 10^9 \text{ cm}^2 \text{ s}^{-1}$ . In the mid-late winter, large  $K_{yy}$  values are seen along the subtropical edges of the polar night jets, characterizing the surf-zone region of the winter stratosphere. This area of maxima moves poleward during late winter, with large mixing at high latitudes during spring of both hemispheres associated with the deceleration and break up of the polar vortices. These figures also show the contrasting degree of winter polar vortex isolation in the two hemispheres. Weak mixing occurs in the core of the SH mid-winter vortex,



consistent with the inhibition of planetary wave propagation through strong westerly winds [Charney and Drazin, 1961]. The NH exhibits significantly weaker  $\bar{u}$  and larger  $K_{yy}$  throughout the winter stratosphere poleward of 25°N. This hemispheric asymmetry is also reflected in the long lived constituent simulations discussed in section 3. In the lower mesosphere, both hemispheres show strong subtropical jets near  $\pm 35^\circ$  in mid-winter, with strong mixing occurring mainly on the poleward flanks of the jets. In the very lower stratosphere (68 mb), westerly winds and significant mixing occur throughout much of the year in the extratropics of both hemispheres. There is also evidence of a semi-annual signal in the mixing in both hemispheres, with largest  $K_{yy}$  in spring and fall coinciding with the build-up and decrease of the winter polar jets. As at higher levels, weaker mixing at 68 mbar is observed in the tropics, and in mid-winter in the cores of the polar jets, especially in the SH.

#### *A.2.b. Gravity Waves*

Computations of vertical eddy diffusion ( $K_{zz}$ ) and mechanical forcing ( $F_{GW}$  in equation 1) from gravity waves are based on the parameterization originally formulated by Lindzen [1981] and modified by Holton and Zhu [1984] (hereafter HZ84). In this scheme, waves propagate vertically and break when the amplitudes become large enough to cause convective overturning. The resulting turbulent diffusion then inhibits further amplitude growth with height, leading to a momentum flux convergence. This mechanical forcing can accelerate or decelerate the zonal mean flow depending on the phase speed of the wave relative to  $\bar{u}$ . This in turn induces a meridional circulation, and, along with the turbulent diffusion, exerts a strong influence on the distribution of trace gases in the middle atmosphere.

Other studies have used this parameterization to compute the time evolution of the zonal mean flow [Schoeberl *et al.*, 1983; HZ84; Garcia and Solomon, 1985]. However, since  $\bar{u}$  and  $\bar{T}$  are pre-determined in our model, we compute the seasonal and spatial distribution of wave drag and diffusion based on the empirically determined zonal wind and temperature fields and an input set of gravity wave parameters. These computed wave effects are highly dependent on the background wind field. For example, previous studies have observed greater wave drag during the SH winter compared with the NH [e.g., Shine, 1989]. It was postulated that the larger planetary wave amplitudes of the NH winter generate a greater range of wind speeds at different longitudes throughout the underlying stratosphere compared with the SH winter. This effectively filters out a greater range of the gravity wave spectrum, resulting in less gravity wave drag and diffusion in the NH winter mesosphere. To account for such longitudinal dependence, we use a 3-D (longitude-latitude-height) background zonal wind field for the calculations of wave drag and diffusion. The zonal mean of this  $u$  field is the same as that described in section A.1.b, with the longitudinal variability based on NCEP and HRDI data for 1992-1996 as discussed in section A.2.a. The longitudinal grid resolution is  $30^\circ$  which, although rather coarse, should be sufficient to accommodate the planetary scale features of the middle atmosphere. Although the wind field is comprised of a 5-year average, the greater degree of zonal asymmetry during the NH winter compared to the SH is represented, and is reflected in the computed fields of wave drag and diffusion.

In accordance with the tropospheric sources of gravity waves, we assume a spectrum of 9 waves with zonal phase speeds  $c = 0, \pm 10, \pm 20, \pm 30, \pm 40 \text{ ms}^{-1}$ . Following HZ84, we specify a horizontal wavelength of 200 km for these waves, consistent with the dominant horizontal wavelength of breaking waves observed in the mesosphere [Vincent and Reid, 1983]. Here we



have assumed that waves are only traveling zonally, although similar results were obtained by assuming an isotropic spectrum of waves as in HZ84. Garcia et al. [1992] obtained a reasonable simulation of the mesospheric zonal wind SAO in their model by including two additional tropical waves with phase speeds  $c = \pm 50 \text{ ms}^{-1}$  and zonal wavelength of 800 km. We have followed this methodology and included these waves in our computations with the largest boundary forcing (see below) at the equator.

For each latitude and longitude, the algorithm first requires determination of the breaking level  $z_{br}$  of each wave. Since more than one wave component in the spectrum can break at a given location, the  $z_{br}$  of a given wave will be modified by the diffusion ( $D$ ) induced by waves breaking at lower levels. The breaking level also depends on molecular diffusion ( $D_{mol}$ ) in the lower thermosphere (as defined in HZ84), and on thermal damping of the wave which is parameterized by Newtonian cooling, so that

$$z_{br} = z_0 + \frac{HN}{k} \int_{z_0}^{z_{br}} \frac{\alpha dz}{(u - c)^2} + \frac{2HN^3}{k} \int_{z_0}^{z_{br}} \frac{(D + D_{mol}) dz}{(u - c)^4} + 3H \ln \left| \frac{u - c}{\hat{u}} \right| \quad (20)$$

where  $c$  and  $k$  are the wave phase speed and zonal wavenumber (corresponding to a 200 or 800 km wavelength),  $\alpha$  is the Newtonian cooling coefficient, and  $z_0$  is the bottom boundary (375 mbar). Forcing at  $z_0$  is determined by  $\hat{u} = (\hat{w}_0 N_0 / k)^{2/3} / |u_0 - c|^{1/3}$ . Here,  $\hat{w}_0$  is a vertical velocity that is specified as a function of the wave phase speed. As with the previous modeling studies, we assume that the small phase velocity waves have the largest bottom boundary forcing. Values of  $\hat{w}_0$  range from  $.03 \text{ ms}^{-1}$  for the slow phase speed waves to  $.002 \text{ ms}^{-1}$  for the fastest waves. We also skewed  $\hat{w}_0$  to have slightly larger values for the westerly waves, following Huang and Smith [1991]. We impose only a weak geographical variation of  $\hat{w}_0$ , with slightly larger values at midlatitudes compared with the tropics and polar regions. To mimic the generation of gravity waves by convection, we also specify slightly larger  $\hat{w}_0$  over subtropical land areas during summer following Wu and Waters [1996]. However, we note that in our current model formulation, the geographical and seasonal variability in the computed gravity wave effects is determined primarily by the background wind in the middle atmosphere.

The turbulent diffusion  $D$  for each wave component is computed in the altitude range  $z_{br} < z < z_c$ , where  $z_c$  is the critical level where  $c = u$ , such that,

$$D = \frac{k}{2} \frac{(u - c)^2}{N^3} \left[ \frac{(u - c)^2}{H} - 3 \frac{\partial u}{\partial z} (u - c) - \frac{\alpha N}{k} \right] \quad (21)$$

Starting with the wave with the lowest  $z_{br}$  (in which  $D = 0$  in equation 20), the breaking levels and diffusion are recomputed for each subsequent wave, taking into account the total diffusion induced by waves breaking at lower levels.

For altitudes in the range  $z_{br} < z < z_c$ , the vertical momentum flux convergence for each component is,

$$-\frac{1}{\rho} \frac{\partial}{\partial z} (\overline{\rho u' w'}) = -\frac{k(u - c)^3}{2N} \left[ \frac{1}{H} - \frac{\partial u}{\partial z} \frac{3}{(u - c)} \right] = F_x \quad (22)$$



Below  $z_{br}$ , a particular wave does not generate diffusion, but undergoes damping from thermal dissipation, molecular diffusion, and the diffusion induced from other waves that are breaking. This wave damping results in a momentum flux convergence given by HZ84 (see their equation 40) which we also include in our computations of  $F_x$ .

The computed wave drag and diffusion may exhibit discontinuities between the breaking levels of the different wave components. To smooth out these features and to allow for sporadic wave breaking below  $z_{br}$ , we include an exponential decay of diffusion ( $D_{sp}$ ) and momentum deposition ( $F_{xsp}$ ) below  $z_{br}$  for each wave. The diffusion and wave drag, including that due to sporadic wave breaking, are summed over all waves to obtain total distributions of these quantities ( $K_{zz}$  and  $F_{GW}$ ). We also include the wave driving due to the turbulent diffusion of the zonal flow so that,

$$F_{GW} = \epsilon(F_x + F_{xsp}) + \frac{1}{\rho} \frac{\partial}{\partial z} \left[ \rho K_{zz} \frac{\partial \bar{u}}{\partial z} \right], \quad \text{and} \quad K_{zz} = \epsilon(D + D_{sp}) \quad (23)$$

where  $\epsilon$  is an intermittency factor discussed below. The  $K_{zz}$  and  $F_{GW}$  values are then zonally averaged, and smoothed in latitude and height.

As discussed in previous studies, the Lindzen parameterization gives unreasonably large values of diffusion and momentum deposition. This problem was alleviated by applying an intermittency factor ( $\epsilon$ ) to the computed values in equations (21)-(23). This represents the fact that gravity wave breaking is not continuous, but rather is sporadic in time and space. For our calculations we found it necessary to set  $\epsilon = .025$  for all wave components. The values of  $\epsilon$  along with  $\hat{w}_0$  used to determine  $z_{br}$  were specified to compute a wave drag peaking at about  $100 \text{ ms}^{-1} \text{ day}^{-1}$  in the upper mesosphere as inferred previously [e.g., Holton, 1983; Fritts and Vincent, 1987]. This wave drag was in rough qualitative agreement but larger in magnitude compared with the mesospheric momentum residual obtained from the empirically determined diabatic circulation [e.g., Shine, 1989; Huang and Smith, 1991]. As discussed in section 3.2.a, our computed values of wave drag and diffusion gave good agreement in the computed seasonal cycle of mesospheric  $\text{H}_2\text{O}$  compared with UARS/HALOE measurements. It may be possible to further improve the simulations of mesospheric tracers by specifying the input parameters to have much stronger seasonal or spatial variability than is presently employed. However, we have not done this given the current lack of gravity wave observations, although recent work has begun to better characterize gravity waves on a global basis [e.g., Wu and Waters, 1996; Alexander and Rosenlof, 1996; Alexander, 1998].

We also include a contribution to the zonal mean  $F_{GW}$  and  $K_{zz}$  from the breaking diurnal tide in the lower thermosphere as discussed by Lindzen [1981]. In accordance with UARS/HRDI observations [Lieberman and Hays, 1994] and theoretical estimates [Forbes, 1982], we specify the largest values to be at the equator at 90-100 km, with a semiannual variation maximizing at the equinoxes. Values exponentially decrease in latitude and height. Largest values for March at 90 km at the equator are set to  $-10 \text{ ms}^{-1} \text{ day}^{-1}$  for wave drag and  $30 \text{ m}^2 \text{s}^{-1}$  for diffusion.

The total zonal mean  $F_{GW}$  from gravity waves and the diurnal tide is then applied in equations (5)-(6). The total  $K_{zz}$  including the background value (section A.2.d) is then used in the model transport of chemical constituents. We impose an upper limit of  $100 \text{ m}^2 \text{s}^{-1}$  to accomodate the 3 hour time step used for the vertical diffusive transport of constituents.



Previous studies have discussed the possibility that the turbulent Prandtl number,  $Pr$  (i.e., the ratio of the total eddy momentum diffusivity to the eddy diffusivity of heat or constituents) has a value greater than unity [e.g., Smith and Brasseur, 1991; Huang and Smith; 1991]. Quantification of  $Pr$  in our model is difficult given that we do not compute  $\bar{u}$  or  $\bar{T}$ . Applying a value of  $Pr > 1$  to the quantities computed in our gravity wave scheme essentially decreases the relative importance of the diffusive transport of constituents compared to the advective transport. However, the advective contribution already dominates in our current model formulation which has  $Pr = 1$  [Chandra *et al.*, 1997]. Using a value of  $Pr > 1$  did not improve the overall simulation of mesospheric  $H_2O$  compared with UARS/HALOE data. Because of this and the uncertainties in determining  $Pr$ , we have elected to set  $Pr = 1$  in the present model study.

Figures A.5b and A.5d show latitude-height sections of gravity wave drag ( $F_{GW}$ ) and vertical diffusion from the gravity wave scheme together with the background specifications (see section A.2.d). These calculations are consistent with previous model results [e.g., Garcia and Solomon, 1985]. The largest wave drag occurs in the middle to upper mesosphere. Values of  $F_{GW}$  are opposite in sign to  $\bar{u}$  (Figure A.1b) as the gravity wave drag acts to close off the jets in the upper mesosphere, and induce the summer-winter meridional flow pattern (Figure A.1d). The  $K_{zz}$  field also shows maxima occurring in regions of large  $\bar{u}$  in the mid-latitude upper mesosphere, with a distinct minimum in the tropics. This pattern is very similar to zonally averaged small scale variances seen in UARS microwave limb sounder (MLS) radiance measurements, which may be an indicator of gravity wave activity [Wu and Waters, 1996]. The tropopause is also evident in this figure, as seen by the sharp transition from large  $K_{zz}$  in the troposphere to very small values in the stratosphere. The determination of the model  $K_{zz}$  in this region is discussed in section A.2.d.

### A.2.c. Kelvin Waves

Equatorial Kelvin waves are thought to be important in driving the westerly acceleration of the stratospheric SAO and related meridional circulation. To approximate this process, we used the parameterization of Dunkerton [1979] and Gray and Pyle [1987] along with the empirical  $\bar{u}$  and  $\bar{T}$  (section A.1.b) to diagnose the mechanical forcing from thermally damped Kelvin waves. The expression for the mean flow acceleration at the equator is,

$$\frac{\partial \bar{u}_{eq}}{\partial t} = B \exp \left[ \frac{z - z_0}{H} \right] R(z) \exp[-P(z)] \quad (24)$$

where,

$$R(z) = \frac{\alpha N}{k(\bar{u} - c)^2}, \quad \text{and} \quad P(z) = \int_{z_0}^z R(z') dz' \quad (25)$$

Here,  $z_0$  is taken to be 14 km (138 mb),  $B$  is the vertical momentum flux at  $z_0$ ,  $\alpha$  is the thermal damping rate as a function of height,  $c$  is the zonal phase speed specified as  $50 \text{ ms}^{-1}$ , and  $k = 1$  is the zonal wavenumber. We specified  $B$  to be  $.0105 \text{ m}^2 \text{s}^{-2}$  which is a factor of 1.5 larger than that used by Gray and Pyle [1987]. We also used a thermal damping



rate which was slightly slower than the 'fast' rates of Dunkerton [1979], with a minimum e-folding damping time of 2.7 days near 50 km. We found that specifying these values of  $B$  and  $\alpha$  resulted in model simulated tracer fields most similar to observations. The latitudinal distribution of the forcing is [Gray and Pyle, 1987],

$$F_{KW} = \frac{\partial \bar{u}_{eq}}{\partial t} \exp \left[ \frac{-2\Omega a \phi^2}{c - \bar{u}} \right] \quad (26)$$

where  $a$  and  $\Omega$  are the radius and rotation rate of the earth, and  $\phi$  is latitude. The acceleration  $F_{KW}$  is then used in the forcing of the streamfunction in equations (5)-(6).

Figure A.7a-f shows the wave driving and zonal mean circulation at the equator. The zonal mean wind shows the well known SAO signature above 10 mb, with a phase reversal between the upper stratosphere and upper mesosphere. Maximum  $F_{KW}$  occurs near the stratopause, with values of  $2-3 \text{ ms}^{-1} \text{ day}^{-1}$ . There is a semiannual oscillation in  $F_{KW}$ , with significant values extending into the upper mesosphere during January and July, coincident with the weakest westerly  $\bar{u}$  in the lower mesosphere. Weakest westerly accelerations in the upper stratosphere and lower mesosphere occur during the equinoxes, when the westerlies are at a maximum. This is consistent with the modeling study of Dunkerton [1979] and the observations of Hirota [1978]. There are also strong semiannual signals in the total heating rate and gravity wave forcing ( $F_{GW}$ ), especially in the middle and upper mesosphere. The resultant  $\bar{w}^*$  field in the upper mesosphere shows a semiannual cycle with maximum upward (downward) motion during the solstices (equinoxes). However, the upper stratosphere and lower mesosphere exhibits a dominant annual cycle with only a weak semiannual component, probably due to the competing influences of the heating and wave driving. The seasonal variation in  $K_{zz}$  also shows a strong semiannual signal above 80 km with maximum mixing during the equinoxes. This semiannual signal reverses phase in the 40-60 km region, although with significantly weaker modulation.

Finally, we show the total wave driving ( $F_{TOT} = F_{PW} + F_{GW} + F_{KW}$ ) for January in Figure A.8. Gravity wave drag dominates the total throughout the upper mesosphere, with the planetary wave effects being a greater contribution to the total in the stratosphere. The signal in the middle to high latitude troposphere is due to the combination of planetary and baroclinic eddies.

#### A.2.d. Tropospheric/Stratospheric $K_{zz}$

We prescribe a baseline  $K_{zz}$  which is added to the  $K_{zz}$  computed from the gravity wave parameterization (section A.2.b). In the troposphere and lower stratosphere at and below 30 km, the background is based on the climatological temperature lapse rate, and is determined as follows. We specify the largest value of  $K_{zz}$  to be  $100 \text{ m}^2 \text{s}^{-1}$  for the steepest lapse rate observed in the lower troposphere (-8 K/km). Following the analyses of Mote *et al.* [1998] and Hall and Waugh [1997b], we specify the minimum  $K_{zz}$  to be  $.01 \text{ m}^2 \text{s}^{-1}$  in the tropical lower stratosphere where the lapse rate is most stable ( $\sim +4 \text{ K/km}$ ). The  $K_{zz}$  values at each grid point throughout the year are then interpolated from these extreme values using the corresponding lapse rate. This methodology assumes that larger mixing occurs in regions of weaker static stability, given that the latter is indicative of stronger convective



overturning. Here we have not accounted for the effects induced by instability in the vertical wind shear given the difficulty in quantifying the diffusion due to this process. Above 30 km, the background  $K_{zz}$  is increased from its value at 30 km to  $.3 \text{ m}^2\text{s}^{-1}$  in the mesosphere. As seen in Figure A.5d, this  $K_{zz}$  profile mimics the large vertical mixing in the troposphere with a sharp decrease in mixing across the tropopause into the lower stratosphere.

### A.3. Numerical Advection Scheme

We have implemented a new numerical advection algorithm replacing the previous scheme based on Prather [1986]. The new algorithm is a two dimensional version of the flux form scheme developed by Lin and Rood [1996] (hereafter LR96) currently used in the GSFC 3-D chemistry and transport model [Douglass *et al.*, 1996]. The new scheme is mass conserving and utilizes an upstream piecewise parabolic method (PPM) [Colella and Woodward, 1984; Carpenter *et al.*, 1990]. We use the fully monotonic PPM so that no new minima or maxima are generated by advection. The algorithm of LR96 also includes cross terms to account for errors produced by operator splitting, i.e., the successive application of meridional and vertical advection operators. A time step of 12 hours is used for the advection of constituents. The PPM is highly accurate (to 4th order) and preserves sharp tracer gradients quite well, while exhibiting very little numerical diffusion. This was found to be especially important for simulations in regions of strong wind shear and sharp gradients in the tracer field, such as water vapor near the tropical tropopause (section 3.2).



## References

Alexander, M.J., Interpretations of observed climatological patterns in stratospheric gravity wave variance, *J. Geophys. Res.* (in press), 1998.

Alexander, M.J., and K.H. Rosenlof, Nonstationary gravity wave forcing of the stratospheric zonal mean wind *J. Geophys. Res.*, **101**, 23465-23474, 1996.

Andrews, D.G., On the interpretation of the Eliassen-Palm flux divergence, *Q.J.R. Meteor. Soc.*, **113**, 323-338, 1987.

Andrews, D.G., and M.E. McIntyre, Planetary waves in horizontal and vertical shear: the generalized Eliassen-Palm relation and the mean zonal acceleration, *J. Atmos. Sci.*, **33**, 2049-2053, 1978.

Andrews, D.G., J.R. Holton, and C.B. Leovy, *Middle Atmosphere Dynamics*, 498 pp., Academic, San Diego, Calif., 1987.

Bacmeister, J.T., Mountain-wave drag in the stratosphere and mesosphere inferred from observed winds and a simple mountain-wave parameterization scheme, *J. Atmos. Sci.*, **50**, 377-399, 1993.

Bacmeister, J.T., M.R. Schoeberl, M.E. Summers, J. Rosenfield, and X. Zhu, Descent of long lived trace gases in the winter polar vortex, *J. Geophys. Res.*, **100**, 11669-11684, 1995.

Bacmeister, J.T., D.E. Siskind, M.E. Summers, S.D. Eckermann, Age of air in a zonally averaged two-dimensional model, *J. Geophys. Res.*, **103**, 11263-11288, 1998.

Barnett, J.J., and K. Labitzke, Climatological distribution of planetary waves in the middle atmosphere, *COSPAR International Reference Atmosphere: 1986, Part II: Middle Atmosphere Models, Adv. Space Res.*, **10**, No. 12, 63-91, 1990.

Boering, K.A., S.C. Wofsy, B.C. Daube, H.R. Schneider, M. Loewenstein, J.R. Podolske, and T.J. Conway, Stratospheric mean ages and transport rates from observations of carbon dioxide and nitrous oxide, *Science*, **274**, 1340-1343, 1996.

Brasseur, G., M.H. Hitchman, S. Walters, M. Dymek, E. Falise, and M. Pirre, An interactive chemical dynamical radiative two-dimensional model of the middle atmosphere, *J. Geophys. Res.*, **95**, 5639-5655, 1990.

Burrage, M.D., M.E. Hagan, W.R. Skinner, D.L. Wu, and P.B. Hays, Long-term variability in the solar diurnal tide observed by HRDI and simulated by the GSWM, *Geophys. Res. Lett.*, **22**, 2641-2644, 1995.

Carpenter, R.L., Jr., K.K. Droege, P.R. Woodward, and C.E. Hane, Application of the piecewise parabolic method (PPM) to meteorological modeling, *Mon. Wea. Rev.*, **118**, 586-612, 1990.

Chandra, S., C.H. Jackman, E.L. Fleming, and J.M. Russell III, The seasonal and long term changes in mesospheric water vapor, *Geophys. Res. Lett.*, **24**, 639-642, 1997.

Charney, J.G., and P.G. Drazin, Propagation of planetary scale disturbances from the lower into the upper atmosphere, *J. Geophys. Res.*, **66**, 83-109, 1961.

Choi, W.K., and J.R. Holton, Transport of N<sub>2</sub>O in the stratosphere related to the equatorial semiannual oscillation, *J. Geophys. Res.*, **96**, 22543-22557, 1991.

Colella, P., and P.R. Woodward, The piecewise parabolic method (PPM) for gas-dynamical simulations, *J. Comp. Phys.*, **54**, 174-201, 1984.

Considine, D. B., A. R. Douglass, and C. H. Jackman, Effects of a polar stratospheric cloud parameterization on ozone depletion due to stratospheric aircraft in a two-dimensional model, *J. Geophys. Res.*, **99**, 18879-18894, 1994.



Conway, T.J., P.P. Tans, L.S. Waterman, K.W. Thoning, D.R. Kitzis, K.A. Masarie, and N. Zhang, Evidence for interannual variability of the carbon cycle from the NOAA Climate Monitoring and Diagnostics Laboratory Global Air Sampling Network, *J. Geophys. Res.*, **99**, 22831-22855, 1994.

DeMore, W.B., S.P. Sander, D.M. Golden, R.F. Hampson, M.J. Kurylo, C.J. Howard, A.R. Ravishankara, C.E. Kolb, and M.J. Molina, Chemical kinetics and photochemical data for use in stratospheric modeling, Evaluation number 12, *JPL Publ.*, **97-4**, 266 pp., 1997.

Dessler et al., Tracer correlations using a 2D Lagrangian parcel model, *J. Atmos. Sci.*, (submitted), 1998.

Douglass, A.R., C.H. Jackman, R.S. Stolarski, Comparison of model results transporting the odd nitrogen family with results transporting separate odd nitrogen species, *J. Geophys. Res.*, **94**, 9862-9872, 1989.

Douglass, A.R., C.J. Weaver, R.B. Rood, and L. Coy, A three-dimensional simulation of the ozone annual cycle using winds from a data assimilation system, *J. Geophys. Res.*, **101**, 1463-1474, 1996.

Dunkerton, T.J., On the mean meridional mass motions of the stratosphere and mesosphere, *J. Atmos. Sci.*, **35**, 2325-2333, 1978.

Dunkerton, T.J., On the role of the Kelvin wave in the westerly phase of the semi-annual zonal wind oscillation, *J. Atmos. Sci.*, **36**, 32-41, 1979.

Elkins, J.W., et al., Airborne gas chromatograph for in situ measurements of long-lived species in the upper troposphere and lower stratosphere, *Geophys. Res. Lett.*, **23**, 347-350, 1996.

Eluszkiewicz, J., et al., Residual circulation in the stratosphere and lower mesosphere as diagnosed from microwave limb sounder data, *J. Atmos. Sci.*, **53**, 217-240, 1996.

Fleming, E.L., and S. Chandra, Equatorial zonal wind in the middle atmosphere derived from geopotential height and temperature data, *J. Atmos. Sci.*, **46**, 860-866, 1989.

Fleming, E.L., S. Chandra, J.J. Barnett, and M. Corney, Zonal mean temperature, pressure, zonal wind, and geopotential height as functions of latitude, *COSPAR International Reference Atmosphere: 1986, Part II: Middle Atmosphere Models*, *Adv. Space Res.*, **10**, No. 12, 11-59, 1990.

Fleming, E.L., S. Chandra, C.H. Jackman, D.B. Considine, and A.R. Douglass, The middle atmospheric response to short and long term solar UV variations: analysis of observations and 2D model results, *J. Atmos. Terr. Phys.*, **57**, 333-365, 1995.

Fleming, E.L., S. Chandra, M.D. Burrage, W.R. Skinner, P.B. Hays, B.H. Solheim, and G.G. Shepherd, Climatological mean wind observations from the UARS high-resolution Doppler imager and wind imaging interferometer: Comparison with current reference models, *J. Geophys. Res.*, **101**, 10455-10473, 1996.

Forbes, J.M., Atmospheric tides 1. Model description and results for the solar diurnal component, *J. Geophys. Res.*, **87**, 5222-5240, 1982.

Fritts, D.C., and R.A. Vincent, Mesospheric momentum flux studies at Adelaide, Australia: Observations and a gravity wave-tidal interaction model, *J. Atmos. Sci.*, **44**, 605-619, 1987.

Garcia, R.R., Parameterization of planetary wave breaking in the middle atmosphere, *J. Atmos. Sci.*, **48**, 1405-1419, 1991.



Garcia, R.R., and S. Solomon, A numerical model of the zonally averaged dynamical and chemical structure of the middle atmosphere, *J. Geophys. Res.*, **88**, 1379-1400, 1983.

Garcia, R.R., and S. Solomon, The effect of breaking gravity waves on the dynamics and chemical composition of the mesosphere and lower thermosphere, *J. Geophys. Res.*, **90**, 3850-3868, 1985.

Garcia, R.R., F. Stordal, S. Solomon, and J.T. Kiehl, A new numerical model of the middle atmosphere, 1. Dynamics and transport of tropospheric source gases, *J. Geophys. Res.*, **97**, 12967-12991, 1992.

Geller, L.S., J.W. Elkins, J.M. Lobert, A.D. Clarke, D.F. Hurst, J.H. Butler, and R.C. Myers, Tropospheric SF<sub>6</sub>: Observed latitudinal distribution and trends, derived emissions and interhemispheric exchange time, *Geophys. Res. Lett.*, **24**, 675-678, 1997.

Gray, L.J., and J.A. Pyle, Two-dimensional model studies of equatorial dynamics and tracer distributions, *Q.J.R. Meteor. Soc.*, **113**, 635-651, 1987.

Hall, T.M., M.J. Prather, Simulations of the trend and annual cycle in stratospheric CO<sub>2</sub>, *J. Geophys. Res.*, **98**, 10573-10581, 1993.

Hall, T.M., and R.A. Plumb, Age as a diagnostic of stratospheric transport, *J. Geophys. Res.*, **99**, 1059-1070, 1994.

Hall, T.M., and D.W. Waugh, Timescales for the stratospheric circulation derived from tracers, *J. Geophys. Res.*, **102**, 8991-9001, 1997a.

Hall, T.M., and D.W. Waugh, Tracer transport in the tropical stratospheric due to vertical diffusion and horizontal mixing, *Geophys. Res. Lett.*, **24**, 1383-1386, 1997b.

Hall, T.M., D.W. Waugh, K.A. Boering, and R.A. Plumb, Evaluation of transport in stratospheric models, *J. Geophys. Res.* (submitted), 1998.

Harnisch, J., R. Borchers, P. Fabian, and M. Maiss, Tropospheric trends for CF<sub>4</sub> and C<sub>2</sub>F<sub>6</sub> since 1982 derived from SF<sub>6</sub> dated stratospheric air *Geophys. Res. Lett.*, **23**, 1099-1102, 1996.

Haynes, P.H., C.J. Marks, M.E. McIntyre, T.G. Shepherd, and K.P. Shine, On the 'downward control' of extratropical diabatic circulations by eddy-induced mean zonal forces, *J. Atmos. Sci.*, **48**, 651-678, 1991.

Hays, P.B., et al., Observations of the diurnal tide from space, *J. Atmos. Sci.*, **51**, 3077-3093, 1994.

Hines, C.O., Doppler-spread parameterization of gravity-wave momentum deposition in the middle atmosphere. Part 1: Basic formulation, *J. Atmos. Sol.-Terr. Phys.*, **59**, 371-386, 1997.

Hiruta, I., Equatorial waves in the upper stratosphere and mesosphere in relation to the semiannual oscillation of the zonal wind, *J. Atmos. Sci.*, **35**, 714-722, 1978.

Holton, J.R., The influence of gravity wave breaking on the general circulation of the middle atmosphere, *J. Atmos. Sci.*, **40**, 2497-2507, 1983.

Holton, J.R., and X. Zhu, A further study of gravity wave induced drag and diffusion in the mesosphere, *J. Atmos. Sci.*, **41**, 2653-2662, 1984.

Holton, J.R., and W.K. Choi, Transport circulation deduced from SAMS species data, *J. Atmos. Sci.*, **45**, 1929-1939, 1988.

Holton, J.R., and M.R. Schoeberl, The role of gravity wave generated advection and diffusion in transport of tracers in the mesosphere *J. Geophys. Res.*, **93**, 11075-11082, 1988.

Huang, T.Y.W., and A.K. Smith, The mesospheric diabatic circulation and the parameterized



thermal effect of gravity wave breaking on the circulation, *J. Atmos. Sci.*, **48**, 1093-1111, 1991.

Jackman, C.H., A.R. Douglass, R.B. Rood, R.D. McPeters, and P.E. Meade, Effect of solar proton events on the middle atmosphere during the past two solar cycles as computed using a two-dimensional model, *J. Geophys. Res.*, **95**, 7417-7428, 1990.

Jackman, C.H., A.R. Douglass, K.F. Brueske, and S.A. Klein, The influence of dynamics on two-dimensional model results: Simulations of  $^{14}\text{C}$  and stratospheric  $\text{NO}_x$  injections, *J. Geophys. Res.*, **96**, 22559-22572, 1991.

Jackman, C.H., E.L. Fleming, S. Chandra, D.B. Considine, and J.E. Rosenfield, Past, present, and future modeled ozone trends with comparisons to observed trends, *J. Geophys. Res.*, **101**, 28753-28767, 1996.

Kinnison, D. E., H. S. Johnston, H. S., and D.J. Wuebbles, Model study of atmospheric transport using carbon 14 and strontium 90 data as inert tracers, *J. Geophys. Res.*, **99**, 20647-20664, 1994.

Ko, M.K.W., K.K. Tung, D.K. Weisenstein, and N.D. Sze, A zonal mean of stratospheric tracer transport in isentropic co-ordinates: Numerical simulations for nitrous oxide and nitric acid, *J. Geophys. Res.*, **91**, 2313-2329, 1985.

Ko, M.K.W., H.R. Schneider, R.L. Shia, D.K. Weisenstein, and N.D. Sze, A two-dimensional model with coupled dynamics, radiation, and photochemistry, 1. Simulation of the middle atmosphere, *J. Geophys. Res.*, **98**, 20429-20440, 1993.

Lieberman, R.S., and P.B. Hays, An estimate of the momentum deposition in the lower thermosphere by the observed diurnal tide, *J. Atmos. Sci.*, **51**, 3094-3105, 1994.

Lin, S.-J., and R.B. Rood, Multidimensional flux-form semi-Lagrangian transport schemes, *Mon. Wea. Rev.*, **124**, 2046-2070, 1996.

Lindzen, R. S., Turbulence and stress owing to gravity wave and tidal breakdown, *J. Geophys. Res.*, **86**, 9707-9714, 1981.

Lindzen, R. S., and H.L. Kuo, A reliable method for the numerical integration of a large class of ordinary and partial differential equations, *Mon. Wea. Rev.*, **96**, 732-734, 1969.

McPeters, R.D., D.F. Heath, and P.K. Bhartia, Average ozone profiles for 1979 from the Nimbus-7 SBUV instrument, *J. Geophys. Res.*, **89**, 5199-5214, 1984.

Mengel, J.G., H.G. Mayr, K.L. Chan, C.O. Hines, C.A. Reddy, N.F. Arnold, and H.S. Porter, Equatorial oscillations in the middle atmosphere generated by small scale gravity waves, *Geophys. Res. Lett.*, **22**, 3027-3030, 1995.

Moore, F.L., J.W. Elkins, E.A. Ray, G.S. Dutton, R.E. Dunn, D.W. Fahey, R.J. McLaughlin, and T.L. Thompson, First in situ gas chromatograph on a balloon platform yielding tracer measurements with improved spatial resolution, (manuscript in preparation), 1998.

Mote, P.W., K.H. Rosenlof, M.E. McIntyre, E.S. Carr, J.C. Gille, J.R. Holton, J.S. Kinnersley, H.C. Pumphrey, J.M. Russell III, and J.W. Waters, An atmospheric tape recorder: The imprint of tropical tropopause temperatures on stratospheric water vapor, *J. Geophys. Res.*, **101**, 3989-4006, 1996.

Mote, P.W., T.J. Dunkerton, M.E. McIntyre, E.A. Ray, P.H. Haynes, and J.M. Russell III, Vertical velocity, vertical diffusion, and dilution by midlatitude air in the tropical lower stratosphere, *J. Geophys. Res.*, **103**, 8651-8666, 1998.

Nedoluha, G.E., R.M. Bevilacqua, R.M. Gomez, W.B. Waltman, B.C. Hicks, D.L. Thacker,



and W.A. Matthews, Measurements of water vapor in the middle atmosphere and implication for mesospheric transport, *J. Geophys. Res.*, **101**, 21183-21193, 1996.

Newell, R.E., J.W. Kidson, D.G. Vincent, and G.J. Boer, *The General Circulations of the Tropical Atmosphere*, vol. 2, chapter 7, MIT Press, Cambridge, Mass., 1974.

Newman, P.A., and J.E. Rosenfield, Stratospheric thermal damping times, *Geophys. Res. Lett.*, **24**, 433-436, 1997.

Newman, P.A., M.R. Schoeberl, R.A. Plumb, and J.E. Rosenfield, Mixing rates calculated from potential vorticity, *J. Geophys. Res.*, **93**, 5221-5240, 1988.

Nightingale, R.W., et al., Global CF<sub>2</sub>Cl<sub>2</sub> measurements by UARS cryogenic limb array etalon spectrometer: Validation by correlative data and a model, *J. Geophys. Res.*, **101**, 9711-9736, 1996.

Oort, A.H., *Global Atmospheric Circulation Statistics, 1958-1983*, NOAA Professional Paper 14, 1983.

Park, J. H., M. K. W. Ko, C. H. Jackman, and R. A. Plumb, Editors, Report of the 1997 Models and Measurements Workshop, held November 3-5, 1997, Williamsburg, Virginia, *NASA Reference Publication XXXX*, 1999.

Patra, P.K., S. Lal, B.H. Subbaraya, C.H. Jackman, and P. Rajaratnam, Observed vertical profile of sulphur hexafluoride (SF<sub>6</sub>) and its atmospheric applications, *J. Geophys. Res.*, **102**, 8855-8859, 1997.

Patten, K.O., Jr., P.S. Connell, D.E. Kinnison, D.J. Wuebbles, T.G. Slanger, and L. Froidevaux, Effect of vibrationally excited oxygen on ozone production in the stratosphere, *J. Geophys. Res.*, **99**, 1211-1223, 1994.

Pierrehumbert, R.T., An essay on the parameterization of gravity wave drag, in Seminar/Workshop Report: Observation, Theory and Modelling of Orographic Effects, Reading, England, European Centre for Medium-Range Weather Forecasts, 251-282, 1987.

Prather, M.J., Numerical advection by conservation of second-order moments, *J. Geophys. Res.*, **91**, 6671-6681, 1986.

Prather, M.J., and E.E. Remsberg, The atmospheric effects of stratospheric aircraft: Report of the 1992 Models and Measurements Workshop, *NASA Ref. Publ.*, **1292**, vols. 1-3, 1993.

Randel, W.J., Global atmospheric circulation statistics, 1000-1 mb, NCAR Tech. Note, TN-36STR, 256 pp., 1992.

Randel, W.J., and R.R. Garcia, Application of a planetary wave breaking parameterization to stratospheric circulation statistics, *J. Atmos. Sci.*, **51**, 1157-1168, 1994.

Randel, W.J., B.A. Boville, J.C. Gille, P.L. Bailey, S.T. Massie, J.B. Kumer, J.L. Mergenthaler, and A.E. Roche, Simulation of stratospheric N<sub>2</sub>O in the NCAR CCM2: Comparison with CLAES data and global budget analyses, *J. Atmos. Sci.*, **51**, 2834-2845, 1994.

Randel, W.J., F. Wu, J.M. Russell III, A. Roche, and J.W. Waters, Seasonal cycles and QBO variations in stratospheric CH<sub>4</sub> and H<sub>2</sub>O observed in UARS HALOE data, *J. Atmos. Sci.*, **55**, 163-185, 1998.

Remsberg, E.E., J.M. Russell III, and C.Y. Wu, An interim reference model for the variability of the middle atmosphere H<sub>2</sub>O vapor distribution, *Handbook for Middle Atmosphere Program*, **31**, 50-66, 1989.

Rinsland, C.P., M.R. Gunson, M.C. Abrams, L.L. Lowes, R. Zander, and E. Mahieu,



ATMOS/ATLAS 1 measurements of sulfur hexafluoride SF<sub>6</sub> in the lower stratosphere and upper troposphere, *J. Geophys. Res.*, 98, 20491-20494, 1993.

Robinson, W.A., The application of the quasi-geostrophic Eliassen-Palm flux to the analysis of stratospheric data, *J. Atmos. Sci.*, 43, 1017-1023, 1986.

Rosenfield, J.E., P.A. Newman, and M.R. Schoeberl, Computations of diabatic descent in the stratospheric polar vortex, *J. Geophys. Res.*, 99, 16677-16689, 1994.

Rosenlof, K.H., Seasonal cycle of the residual mean meridional circirculation in the stratosphere, *J. Geophys. Res.*, 100, 5173-5191, 1995.

Rosenlof, K.H., and J.R. Holton, Estimates of the stratospheric residual circulation using the downward control principle, *J. Geophys. Res.*, 98, 10465-10479, 1993.

Schoeberl, M.R., D.F. Strobel, and J.P. Apruzese, A numerical model of gravity wave breaking and stress in the mesosphere, *J. Geophys. Res.*, 88, 5249-5259, 1983.

Schoeberl, M.R., A.E. Roche, J.M. Russell III, D. Ortland, P.B. Hays, and J.W. Waters, An estimation of the dynamical isolation of the tropical lower stratosphere using UARS wind and trace gas observations of the quasi-biennial oscillation, *Geophys. Res. Lett.*, 24, 53-56, 1997.

Shine, K., Sources and sinks of zonal momentum in the middle atmosphere daignosed using the diabatic circulation, *Q.J.R. Meteor. Soc.*, 115, 265-292, 1989.

Smith, A.K., and G.P. Brasseur, Numerical simulation of the seasonal variation of mesospheric water vapor, *J. Geophys. Res.*, 96, 7553-7563, 1991.

Solomon, S., R.W. Portmann, R.R. Garcia, L.W. Thomason, L.R. Poole, and M.P. McCormick, The role of aerosol variations in anthropogenic ozone depletion at northern midlatitudes, *J. Geophys. Res.*, 101, 6713-6727, 1996.

Stolarski, R.S., et al., Scientific assessment of the atmospheric effects of stratospheric aircraft, *NASA Ref. Pub.*, 1381, 110 pp., 1995.

Strahan, S.E., A.R. Douglass, J.E. Nielsen, and K.A. Boering, The CO<sub>2</sub> seasonal cycle as a tracer of transport, *J. Geophys. Res.*, 103, 13729-13741, 1998.

Summers, M.E., D.E. Siskind, J.T. Bacmeister, R.R. Conway, S. Zasadil, and D.F. Strobel, The seasonal variation of middle atmosphere CH<sub>4</sub> and H<sub>2</sub>O with a new chemical-dynamical model, *J. Geophys. Res.*, 102, 3503-3526, 1997.

Vincent, R.A., and I.M. Reid, HF doppler measurements of mesospheric gravity wave momentum fluxes, *J. Atmos. Sci.*, 40, 1321-1332, 1983.

Volk, C.M., et al., Evaluation of source gas lifetimes from stratospheric observations, *J. Geophys. Res.*, 102, 25543-25564, 1997.

Waugh, D.W., et al., Three-dimensional simulations of long-lived tracers using winds from MACCM2, *J. Geophys. Res.*, 102, 21493-21513, 1997.

Weisenstein, D.W., M.K.W. Ko, N.D. Sze, and J.M. Rodriguez, Potential impact of SO<sub>2</sub> emissions from stratospheric aircraft on ozone, *Geophys. Res. Lett.*, 23, 161-164, 1996.

World Meteorological Organization (WMO), Scientific Assessment of Ozone Depletion: 1991, *Rep. 25* Global Ozone Research and Monitoring Project, Geneva, 1991.

World Meteorological Organization (WMO), Scientific Assessment of Ozone Depletion: 1994, *Rep. 37* Global Ozone Research and Monitoring Project, Geneva, 1995.

Wu, D.L., and J.W. Waters, Satellite observations of atmospheric variances: A possible indication of gravity waves, *Geophys. Res. Lett.*, 23, 3631-3634, 1996.

Yang, H., E. Olaguer, and K.-K. Tung, Simulation of the present-day atmospheric ozone, odd



nitrogen, chlorine, and other species using a coupled 2-D model in isentropic coordinates  
*J. Atmos. Sci.*, 48, 442-471, 1991.

Received \_\_\_\_\_

---

<sup>1</sup>Steve Meyers and Associates Corporation, Vienna, Virginia

<sup>2</sup>NASA Goddard Space Flight Center, Greenbelt, Maryland

<sup>3</sup>University of Maryland, College Park, Maryland



## Figure Captions

**Figure 1.** Zonal mean  $\text{CH}_4$  (ppbv) from the model simulation (solid line) and the HALOE+CLAES climatology (dashed line) for January, April, July, and October. The contour interval is 300 ppbv, and the 150 ppbv contour is also included.

**Figure 2.** Zonal and monthly averaged month-height sections of  $\text{CH}_4$  (ppbv) from the model simulation and the HALOE+CLAES climatology for the northern and southern polar regions. Note that the plots for the NH have been shifted by 6 months to facilitate the visual comparison. The contour interval is 100 ppbv.

**Figure 3.** Model simulation of  $\text{CH}_4$  in ppbv (color) for January and September, along with streamlines depicting the sense of the model residual circulation  $(\bar{v}^*, \bar{w}^*)$ .

**Figure 4.** Model simulation of  $\text{CH}_4$  as in Figure 3 for January and September, (solid contours) along with the model  $K_{yy}$  fields depicted in color. The contour interval for  $\text{CH}_4$  is 100 ppbv, and the  $K_{yy}$  values are in  $10^8 \text{ cm}^2 \text{ sec}^{-1}$ .

**Figure 5.** Zonal and monthly averaged month-latitude sections of  $\text{CH}_4$  (ppbv) from the model simulation and the HALOE+CLAES climatology at 2.2 mb. The contour interval is 100 ppbv.

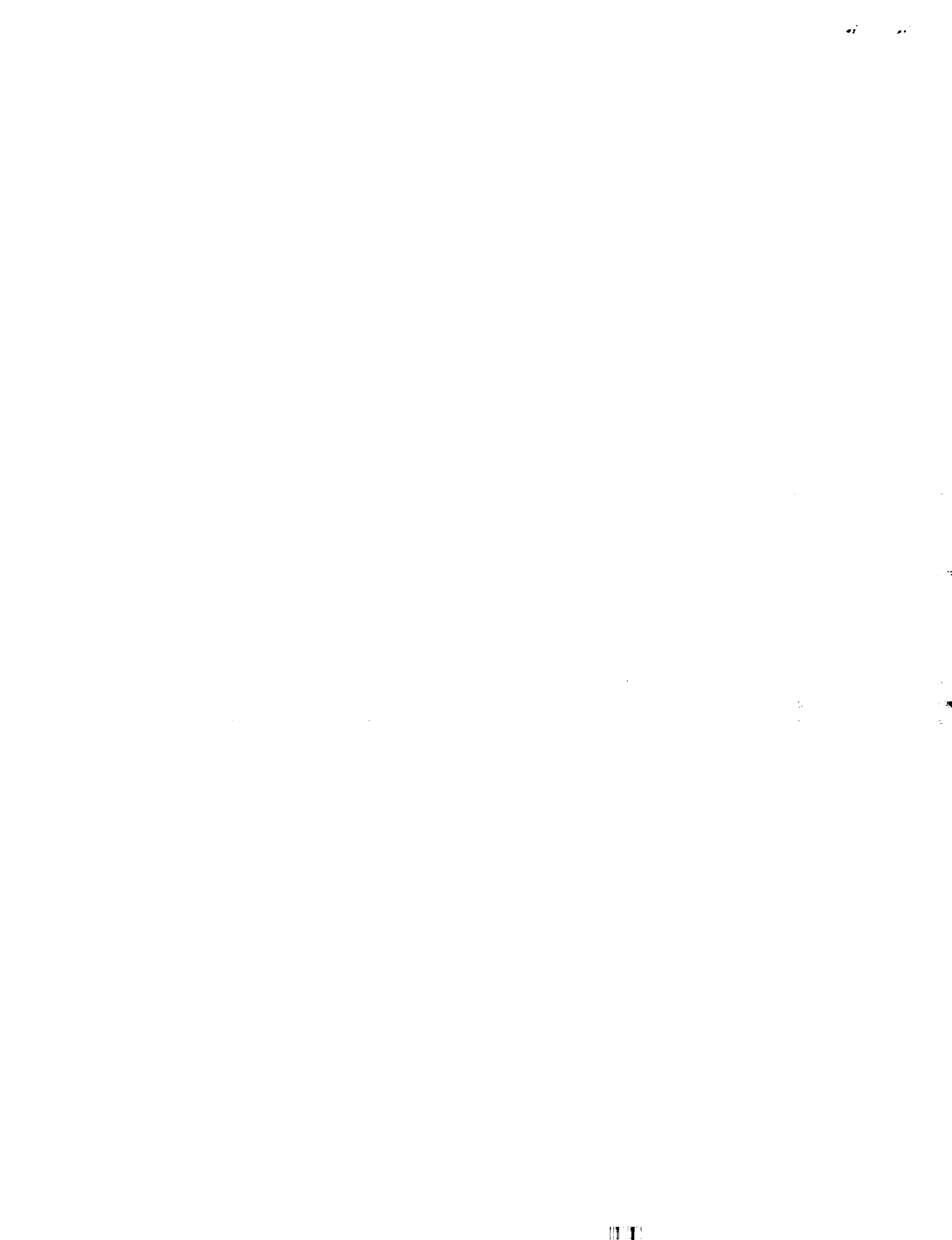
**Figure 6.** Zonal mean  $\text{H}_2\text{O}$  (ppmv) from the model simulation (solid line) and the HALOE+MLS climatology (dashed line) for January, March-April, July, and September-October. The HALOE version 18 data averaged over 1991-1997 is included above 60 km. The contour interval is 1 ppmv.

**Figure 7.** Zonal mean time series of HALOE  $\text{H}_2\text{O}$  (ppmv) averaged from  $10^\circ\text{S}$  and  $10^\circ\text{N}$  for 1993 to 1995. Also shown is the one year climatological model simulation of  $\text{H}_2\text{O}$  at the equator repeated for three years. Water vapor is shown in color and in the overlaid contours in intervals of .2 ppmv.

**Figure 8.** Zonal mean time series of the quantity  $2\text{CH}_4 + \text{H}_2\text{O}$  in ppmv from HALOE averaged from  $10^\circ\text{S}$  and  $10^\circ\text{N}$  for 1993 to 1995. Also shown is the one year climatological model simulation of  $2\text{CH}_4 + \text{H}_2\text{O}$  at the equator repeated for three years. The values are shown in color and in the overlaid contours in intervals of .2 ppmv along with the 6.7 ppmv contour.

**Figure 9.** Vertical profiles of the fractional amplitude and phase lag of the annual cycle in  $2\text{CH}_4 + \text{H}_2\text{O}$  at the equator from the model (solid line) and HALOE data (dashed-asterisk line). These quantities were obtained by Fourier analysis of the values shown in Figure 8. The amplitude has been normalized to the value at the tropical tropopause (100 mb), and the phase lag (years) is defined to be zero at the tropical tropopause.

**Figure 10.** Vertical profiles of the model dynamics in the equatorial lower stratosphere for January (thin solid), April (dotted), July (dashed), October (dash-dot), and the annual



mean (heavy solid). The dilution rate ( $10^{-6} \text{ sec}^{-1}$ ) and its reciprocal, the dilution time scale (months), are estimates of the horizontal in-mixing of mid-latitude air and are based on the model  $K_{yy}$  values (see text for details). Also included are the residual vertical velocity ( $\text{mm/sec}$ ) and the vertical diffusion ( $\text{m}^2/\text{sec}$ ).

**Figure 11.** Seasonal profiles of zonal and monthly mean  $\text{H}_2\text{O}$  from the model (solid) and HALOE data (dashed-asterisk) for 80 km (.01 mbar) at 45°N, equator, and 45°S.

**Figure 12.** Same as Figure 11 for 65 km (.1 mbar).

**Figure 13.** Zonal and monthly mean total ozone from Nimbus-7 TOMS version 7 data averaged over 1988 to 1992 (top), the model simulation corresponding to 1990  $\text{Cl}_y$  loading (middle), and the difference, model minus TOMS (bottom). The contour interval is 20 Dobson units (DU).

**Figure 14.** Time dependent model simulations of carbon 14 every six months between January 1964 and July 1966. The contour interval is 50 mixing ratio units, defined as  $10^5$  atoms of  $^{14}\text{C}$  per gram of dry air [Kinnison *et al.*, 1994].

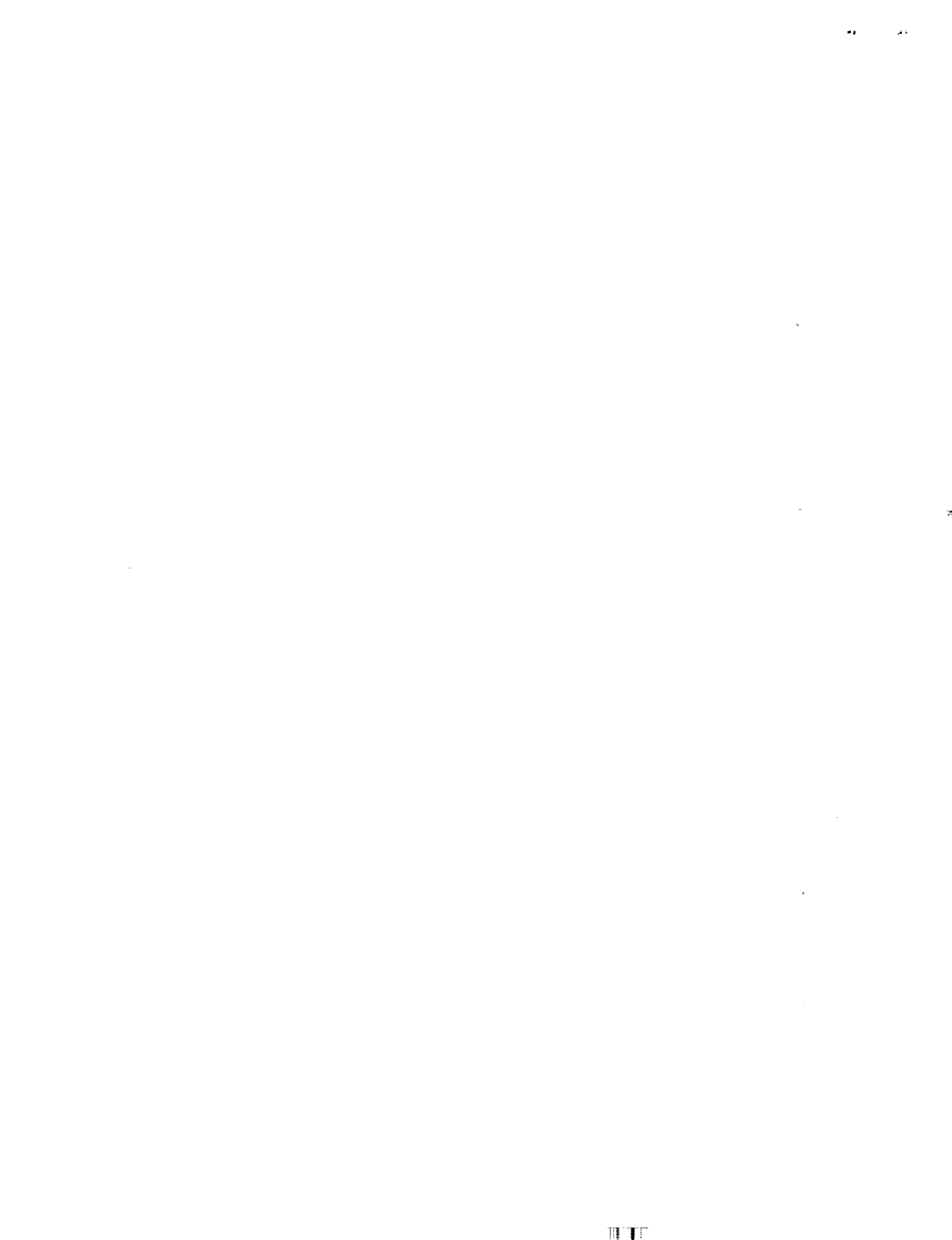
**Figure 15.** Vertical profiles of carbon 14 at 31°N every six months between January 1964 and July 1966. Plotted are the time dependent model simulations using the new transport algorithm (solid), the previous 1995 transport algorithm (dotted), and observations (Kinnison *et al.* [1994] - dashed-asterisk). Values are in mixing ratio units, defined as  $10^5$  atoms of  $^{14}\text{C}$  per gram of dry air.

**Figure 16.** Vertical profiles of strontium 90 at 9°N for six time periods between January 1965 and October 1966. Plotted are the time dependent model simulations using the current transport algorithm (solid), the previous 1995 transport algorithm (dotted), and observations (Kinnison *et al.* [1994] - dashed-asterisk). Units are proportional to mixing ratio as in Kinnison *et al.* [1994]. Model simulations include a settling velocity for strontium-90 as discussed in the text.

**Figure 17.** Vertical profiles of strontium 90 at 34°S for six time periods between April 1965 and October 1966. Plotted are the time dependent model simulations using the current transport algorithm (solid), the previous 1995 transport algorithm (dotted), and observations (Kinnison *et al.* [1994] - dashed-asterisk). Units are proportional to mixing ratio as in Kinnison *et al.* [1994]. Model simulations include a settling velocity for strontium-90 as discussed in the text.

**Figure 18.** Mean age of air (years) derived from time dependent model simulations of  $\text{SF}_6$  for January, April, July, and October. The age is taken relative to the global mean value at the surface. The contour interval is 0.5 years.

**Figure 19.** Age of air as a function of latitude for October/November 1994 and January/February 1996. The ages are derived from  $\text{SF}_6$  using ER-2 measurements at 19-21



km (triangles) and model simulations at 20 km (lines). Included are model simulations using the previous 1995 model transport (dotted line), the current 1998 transport (solid line), and the 1998 transport with a photochemical loss identical to CFC-115 imposed on SF<sub>6</sub> (dashed line). The age is taken relative to the global mean value at the surface.

**Figure 20.** Vertical profiles of age of air from the model and balloon data taken at the latitudes and seasons indicated. The observations are from OMS SF<sub>6</sub> (triangles) and the balloon SF<sub>6</sub> measurements of Harnisch *et al.* [1996] (asterisks and squares). Included are model simulations using the previous 1995 model transport (dotted line), the current 1998 transport (solid line), and the 1998 transport with a photochemical loss identical to CFC-115 imposed on SF<sub>6</sub> (dashed line). The age is taken relative to the global mean value at the surface.

**Figure 21.** Age of air derived from SF<sub>6</sub> as a function of latitude for October/November 1994 and January/February 1996. The ER-2 observations (triangles) are identical to Figure 19. The model simulations are for 20 km and include: the standard '1998 model' as in Figure 19 (solid line); the standard '1998 model' with the minimum lower stratospheric  $K_{zz}$  increased to  $.1 \text{ m}^2 \text{s}^{-1}$  (dashed line); and the standard '1998 model' with the minimum lower stratospheric  $K_{zz}$  increased to  $1 \text{ m}^2 \text{s}^{-1}$  (dash-dot-dot-dot line). No mesospheric loss is imposed on SF<sub>6</sub>.

**Figure 22.** Vertical profiles of age of air from the model and balloon data taken at the latitudes and seasons indicated. The observations are identical to Figure 20 (OMS SF<sub>6</sub> - triangles; balloon SF<sub>6</sub> measurements of Harnisch *et al.* [1996] - asterisks and squares). The model simulations include: the standard '1998 model' as in Figure 20 (solid line); the standard '1998 model' with the minimum lower stratospheric  $K_{zz}$  increased to  $.1 \text{ m}^2 \text{s}^{-1}$  (dashed line); and the standard '1998 model' with the minimum lower stratospheric  $K_{zz}$  increased to  $1 \text{ m}^2 \text{s}^{-1}$  (dash-dot-dot-dot line). No mesospheric loss is imposed on SF<sub>6</sub>.

**Figure 23.** Latitude-height cross sections of the model annual cycle of CO<sub>2</sub>: (a) amplitude (ppmv), defined as one-half of the difference from peak to trough of the seasonal variation; (b) phase (month of maximum).

**Figure 24.** Time series of the model CO<sub>2</sub> (ppmv) at 55°N for 1994 and 1995 plotted at the indicated pressure levels.

**Figure 25.** Time series of CO<sub>2</sub> (ppmv) for 1992 to 1997 from the model simulation at the tropical tropopause (solid line), the average of the surface time series at Mauna Loa (19°N) and Samoa (14°S) with a two month time lag (dashed line), and averages of ER-2 CO<sub>2</sub> measurements taken just above the tropopause [Boering *et al.*, 1996] (triangles).

**Figure 26.** Time series of CO<sub>2</sub> (ppmv) for 1994 and 1995 from ER-2 observations (top row) and the model (bottom row) for three latitude ranges: tropics (6°S-12°N), subtropics (12°S-30°N), and midlatitudes (30°S-48°N). The observations are least squares fits to the seasonal cycle and trend and are adapted from Strahan *et al.* [1998]. The data have been binned by N<sub>2</sub>O and encompass three potential temperature ranges: 370-410K (solid line), 395-435K (dashed line), and 440-480K dashed-dotted line). See text for details.



**Figure 27.** Time series of CO<sub>2</sub> (ppmv) for 1994 and 1995 as in Figure 26, but plotted only for 370-410K for the three latitude regions indicated.

**Figure 28.** Vertical profiles of CO<sub>2</sub> (ppmv) versus potential temperature (K) from the model (solid line) and ER-2 measurements (plus sign) averaged over 10°S to 10°N for the month/year indicated. Approximate altitude is shown on the right hand axes.

**Figure 29.** Vertical profiles of CO<sub>2</sub> (ppmv) versus potential temperature (K) from the model (solid line) and ER-2 measurements (plus sign) averaged over 30°N to 40°N and 70°S to 60°S for the month/year indicated. Approximate altitude is shown on the right hand axes.

**Figure 30.** As in Figure 29, but with CO<sub>2</sub> (ppmv) plotted versus N<sub>2</sub>O (ppbv).

**Figure A.1.** Latitude-height sections of zonal mean temperature (a), zonal wind (b), and residual vertical velocity (c) and horizontal velocity (d) from the model transport. The contour intervals are 10K for temperature; 10 m/sec for zonal wind; 0.5 cm/sec for  $\bar{w}^*$  including the contours for  $\pm.2$ ,  $\pm.1$ , and  $\pm.05$  cm/sec; and 2 m/sec for  $\bar{v}^*$  including the contours for  $\pm 1$ ,  $\pm .5$ , and  $\pm .2$  m/sec. Negative values are shaded.

**Figure A.2.** Net diabatic heating rates for January. The contour intervals are 2 K/day and include the contours for  $\pm 1$ , and  $\pm .5$  K/day. Negative values are shaded.

**Figure A.3.** Contributions to the total heating rate for January from, latent heating (a), gravity wave heating effects separated (b-c), and the net gravity wave heating (d). See text for details. Contour intervals are .5K/day for latent heating, and 2K/day including the contours for  $\pm 1$ , and  $\pm .5$  K/day for the gravity wave heating. Negative values are shaded.

**Figure A.4.** The total heating rate for January. Contour intervals are 2K/day and include the contours for  $\pm 1$ , and  $\pm .5$  K/day. Negative values are shaded.

**Figure A.5.** Eliassen-Palm flux divergence due to planetary and synoptic scale waves (a) and gravity waves (b) for January. Also plotted are the associated model eddy diffusion coefficients  $K_{yy}$  (c) and  $K_{zz}$  (d). The contour intervals are, for (a): 2 m/sec/day including  $\pm 1$  and  $\pm .5$  m/sec/day (shaded corresponds to values  $\leq -2$  m/sec/day); (b): 20 m/sec/day including  $\pm 10$ ,  $\pm 5$ , and  $\pm 1$  m/sec/day (negative values are shaded); (c):  $1 \times 10^{10}$  cm<sup>2</sup>/sec including  $2 \times 10^8$ ,  $1 \times 10^9$ , and  $5 \times 10^9$  cm<sup>2</sup>/sec (shaded corresponds to  $K_{yy} \geq 1 \times 10^{10}$  cm<sup>2</sup>/sec); and, (d):  $2 \times 10^5$  cm<sup>2</sup>/sec including 200, 300, 1000,  $1 \times 10^4$ ,  $5 \times 10^4$ ,  $1 \times 10^5$  cm<sup>2</sup>/sec.

**Figure A.6.** Month-latitude sections of the model  $K_{yy}$  fields in color, along with  $\bar{u}$  overlaid in solid contours, for 68 mbar (a), 12 mbar (b), 1.7 mbar (c), and .1 mbar (d). The contour interval for  $\bar{u}$  is 10 m/sec, and the  $K_{yy}$  values are in  $10^8$  cm<sup>2</sup>/sec.

**Figure A.7.** Month-height sections of the model dynamical fields at the equator. Shown are  $\bar{u}$  (a), the total heating rate (b), the Eliassen-Palm flux divergence due to Kelvin waves (c) and gravity waves (d), the residual vertical velocity,  $\bar{w}^*$  (e), and the vertical diffusion,  $K_{zz}$  (f).

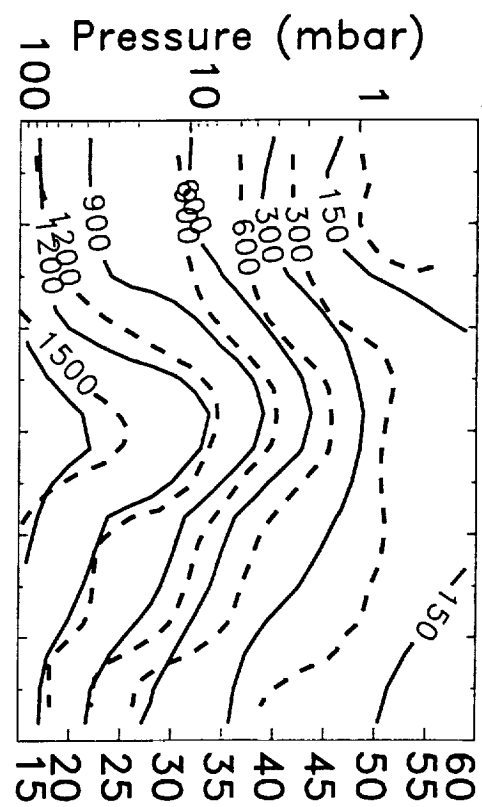


The contour intervals are, for (a):  $10 \text{ m/sec}$ ; (b):  $2K/\text{day}$  including  $\pm 1$  and  $\pm .5K/\text{day}$ ; (c):  $.5 \text{ m/sec/day}$  including  $.1 \text{ m/sec/day}$ ; (d):  $2 \text{ m/sec/day}$  including  $\pm 1$  and  $\pm .5 \text{ m/sec/day}$ ; (e):  $.2 \text{ cm/sec}$  including  $\pm .1, \pm .05, \pm .02, \pm .01 \text{ cm/sec}$ ; and, (f):  $.02, .1, .2, .5, 1, 2, 5, 10, 15, 20$ , and  $30 \text{ m}^2/\text{sec}$ . Negative values are shaded for all plots.

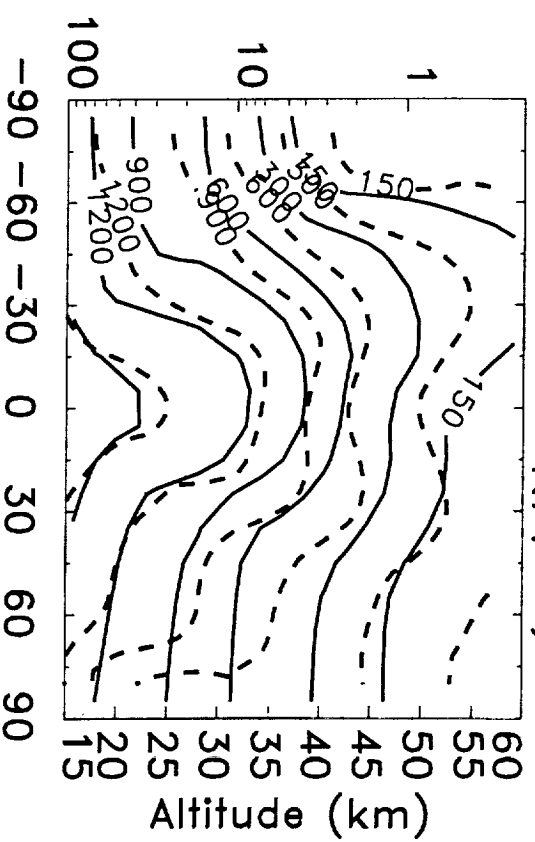
**Figure A.8.** The total Eliassen-Palm flux for January. Contour intervals are  $20 \text{ m/sec/day}$  and include the contours for  $\pm 1, \pm 2, \pm 5$ , and  $\pm 10 \text{ m/sec/day}$ . Negative values are shaded.



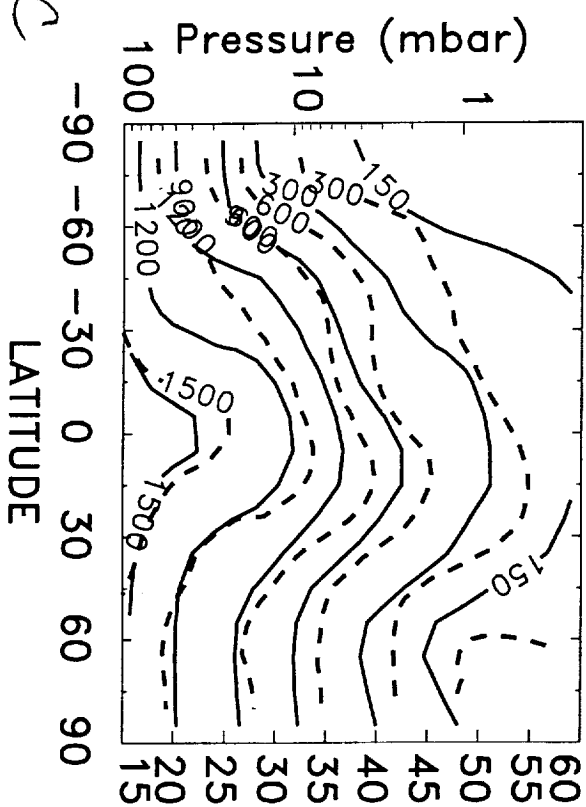
JANUARY  $\text{CH}_4$ (ppbv)



APRIL  $\text{CH}_4$ (ppbv)



JULY  $\text{CH}_4$ (ppbv)



OCTOBER  $\text{CH}_4$ (ppbv)

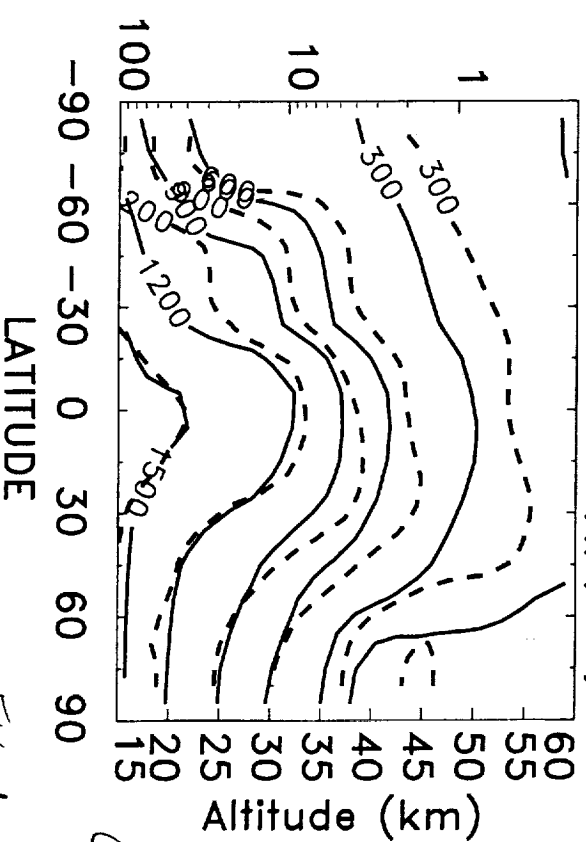
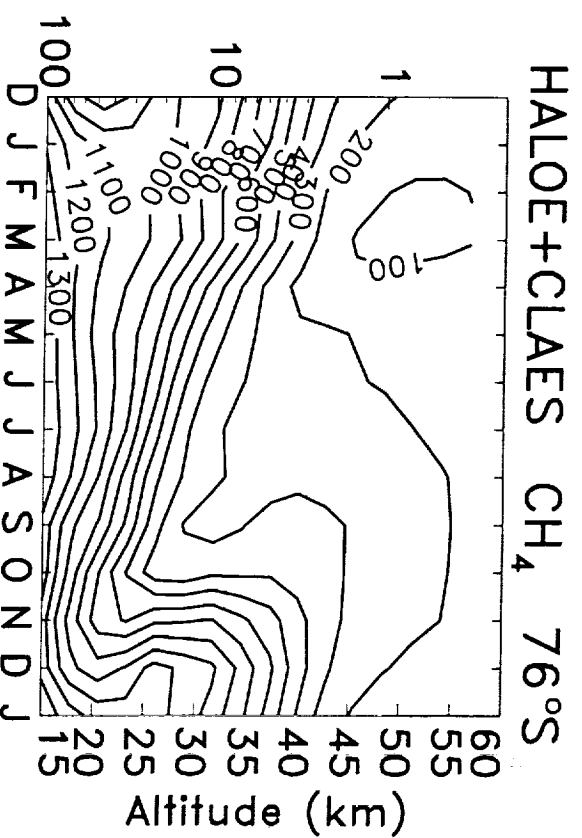
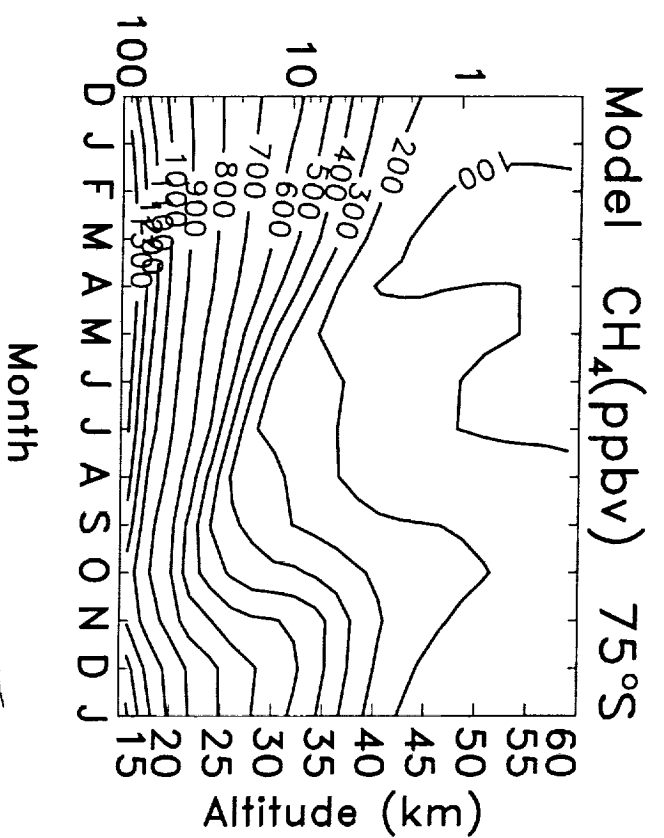
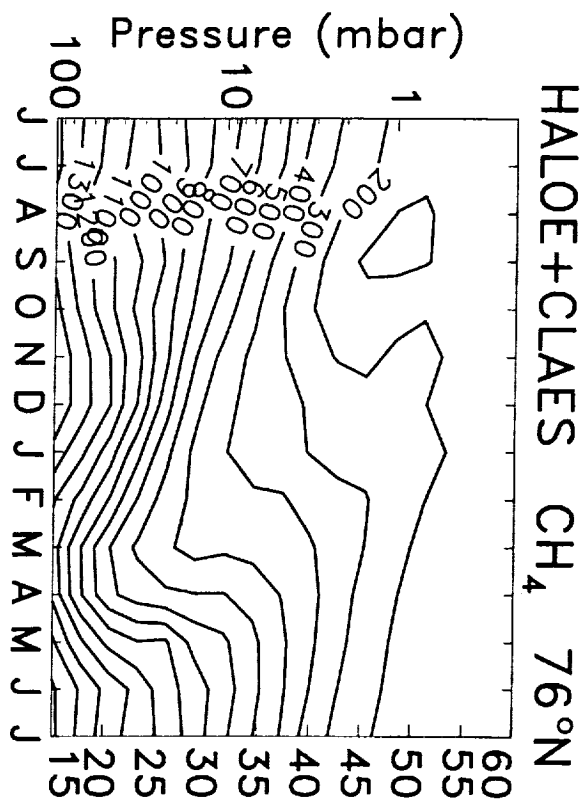
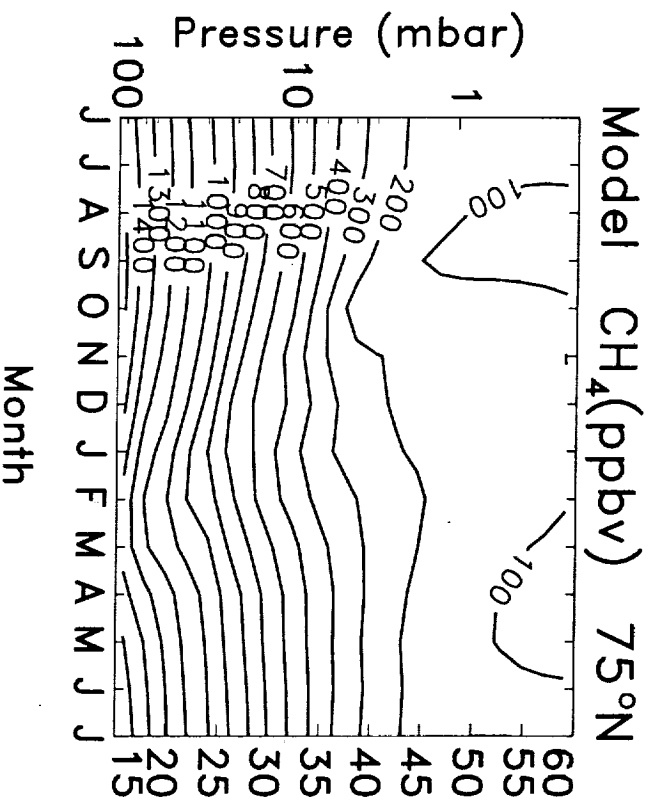


FIG. 1



# Circulation, $\text{CH}_4$ (ppbv)

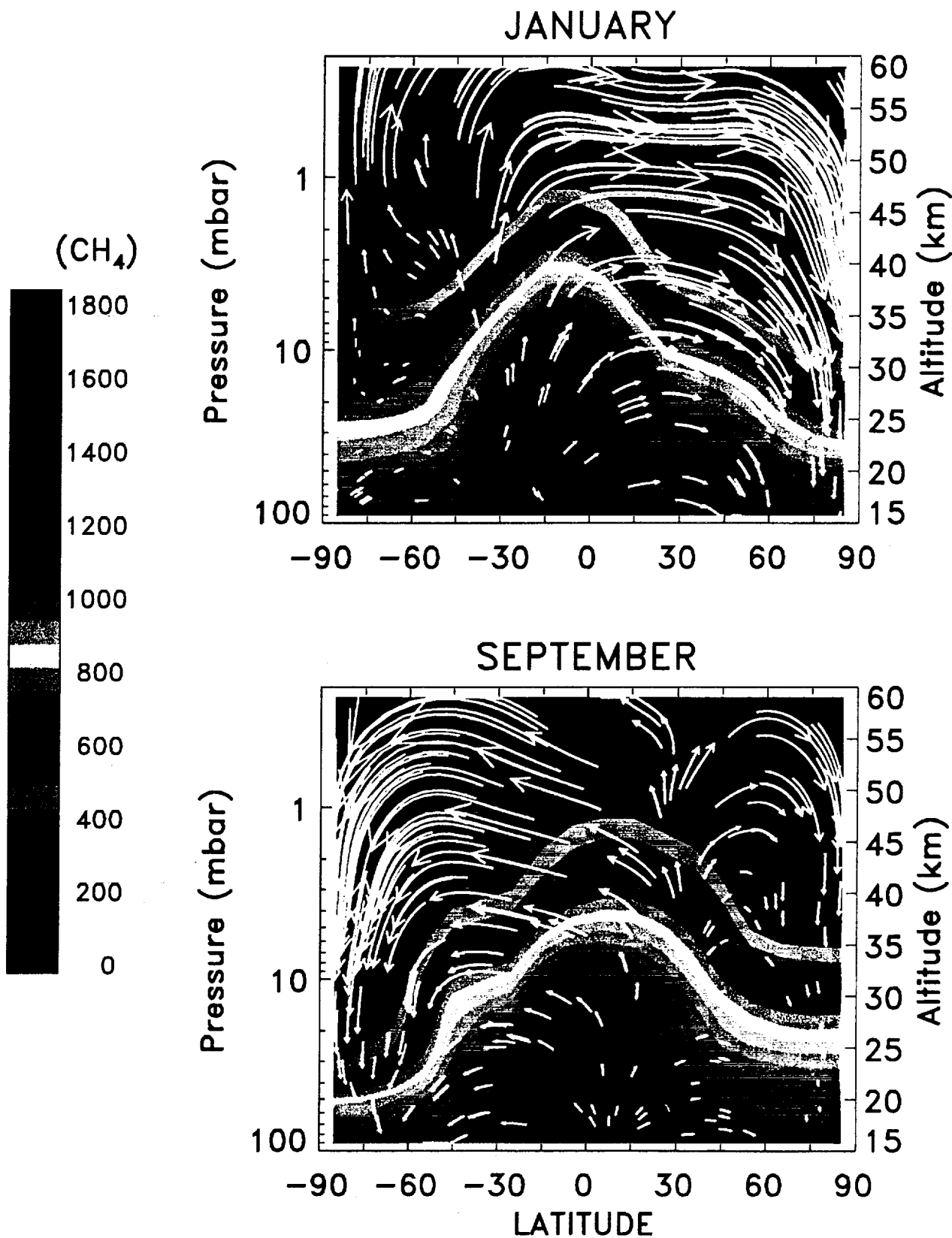
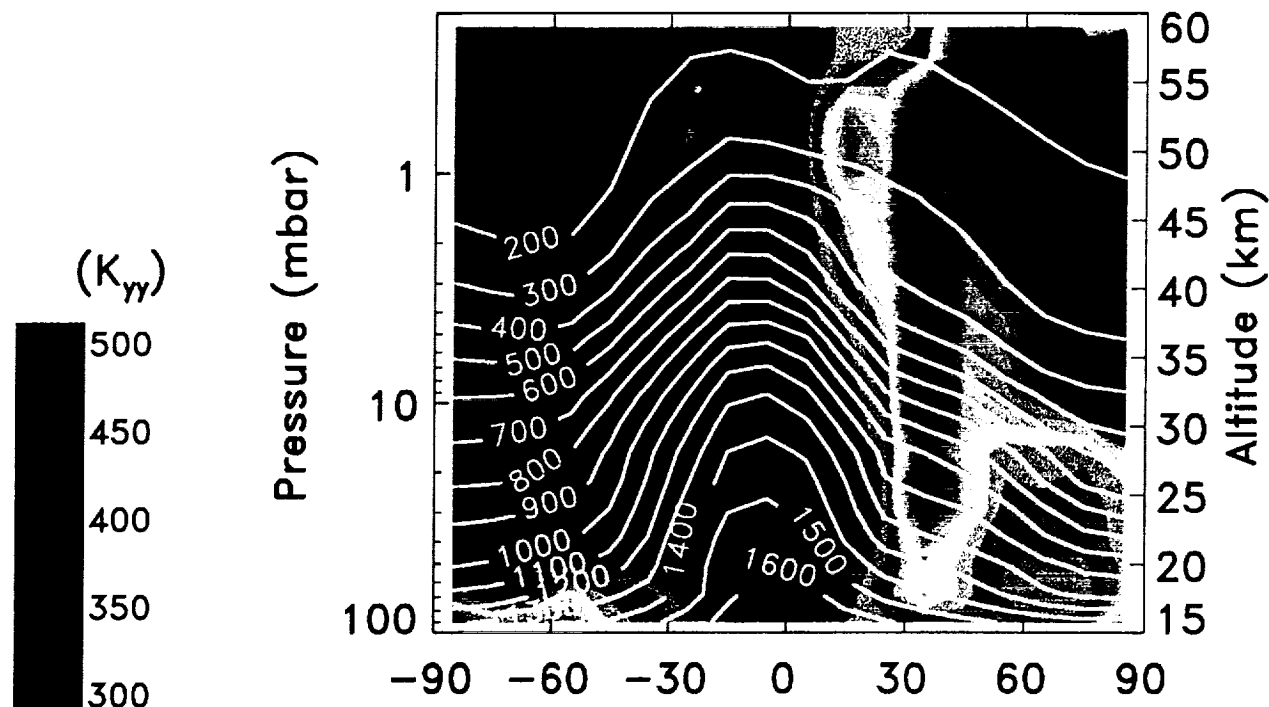


FIG 3

$K_{yy}$  ( $10^8$  cm $^2$ /sec), CH $_4$  (ppbv)

JANUARY



SEPTEMBER

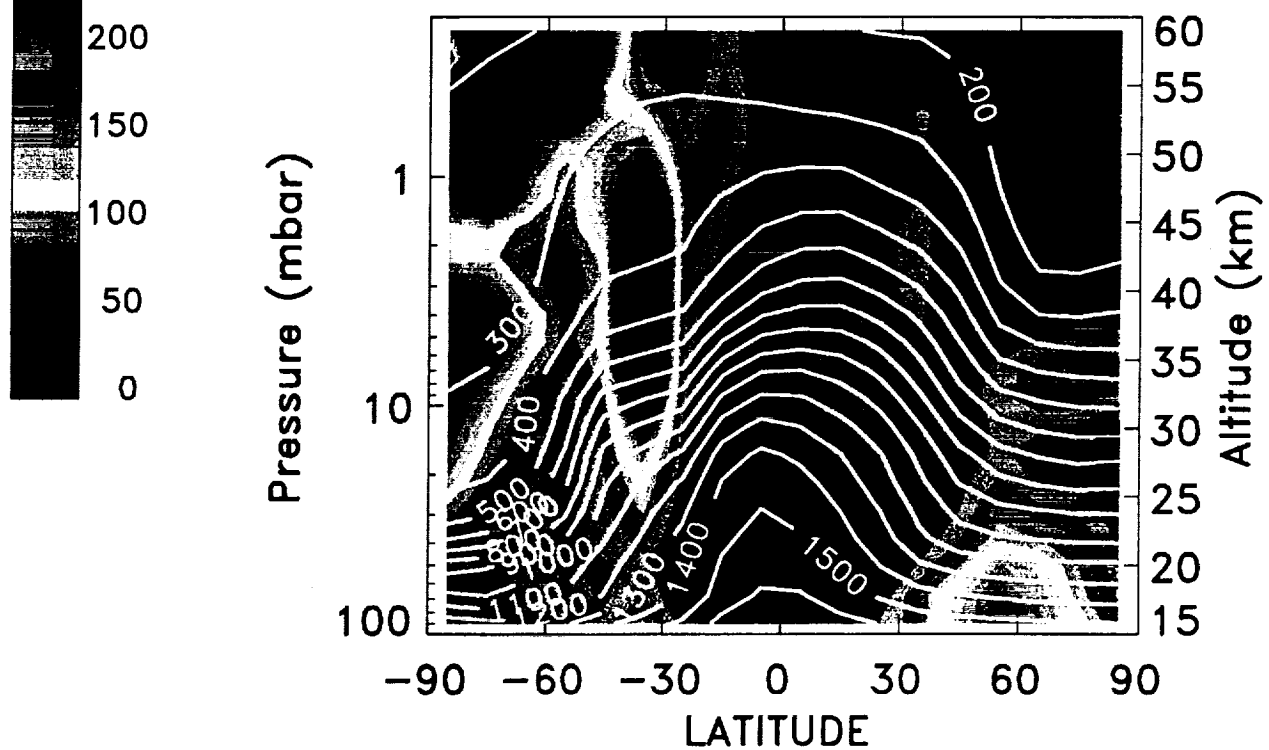


FIG 4

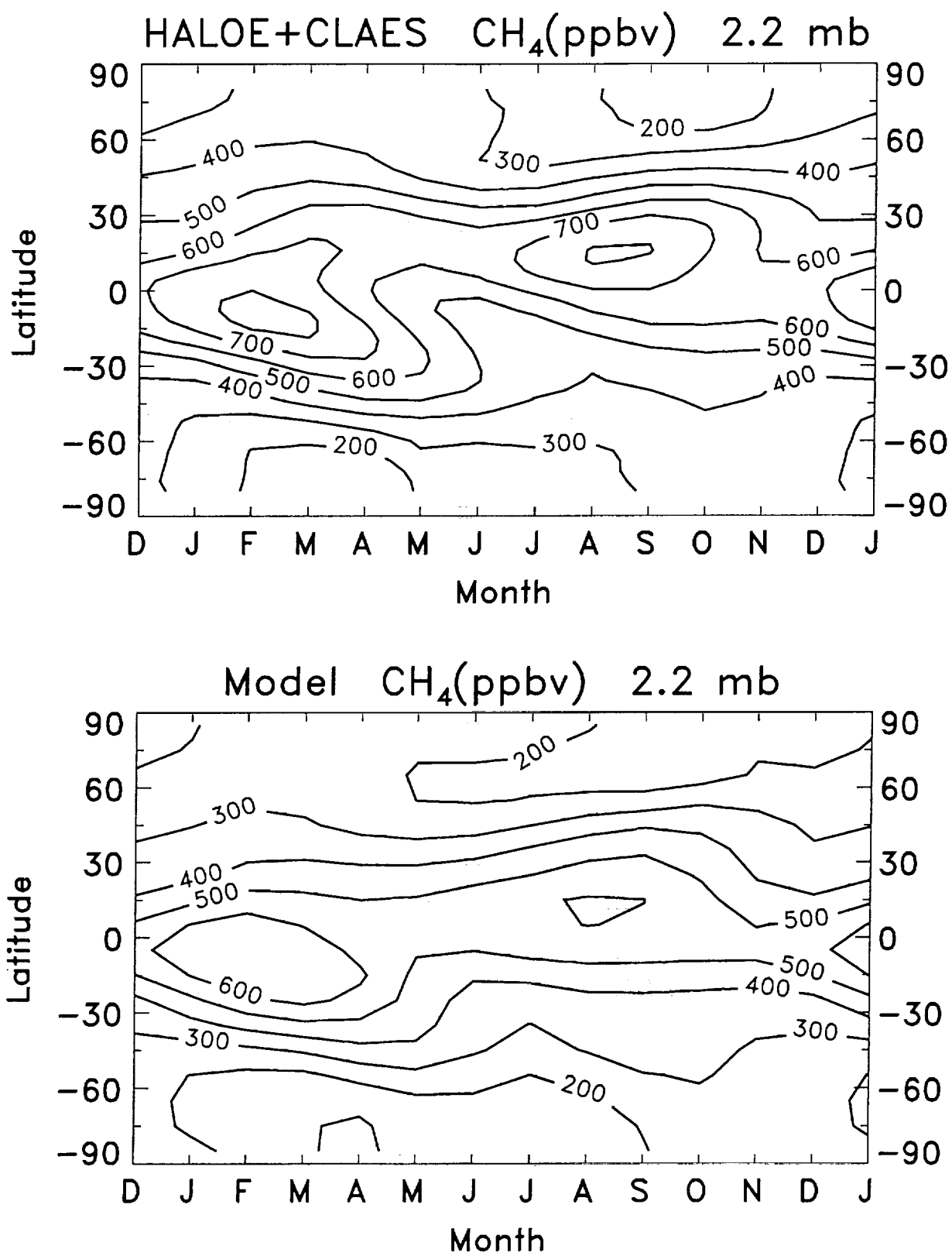
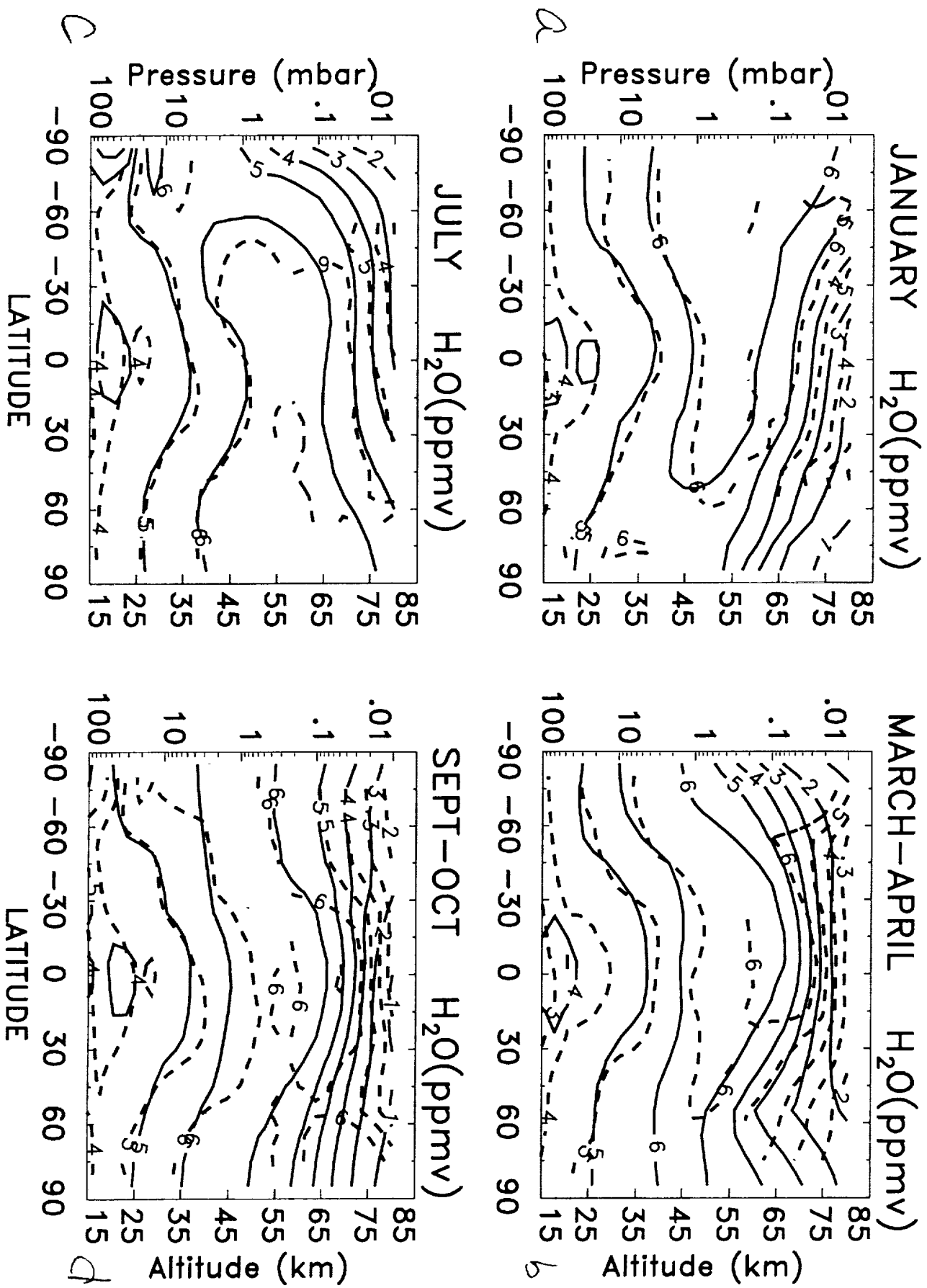


FIG 5



# HALOE $\text{H}_2\text{O}$ (ppmv) $10^\circ\text{S} - 10^\circ\text{N}$



# 2D Model $\text{H}_2\text{O}$ (ppmv) Equator

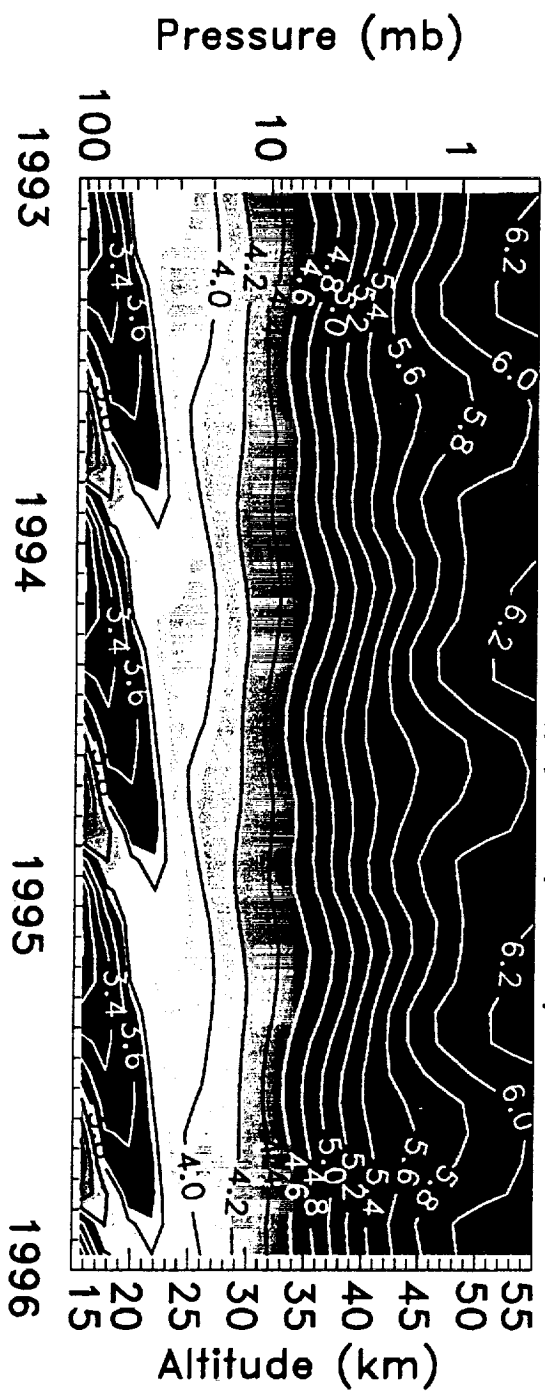


Fig 7

HALOE  $2*\text{CH}_4 + \text{H}_2\text{O}$  (ppmv)  $10^\circ\text{S} - 10^\circ\text{N}$



2D Model  $2*\text{CH}_4 + \text{H}_2\text{O}$  (ppmv) Equator

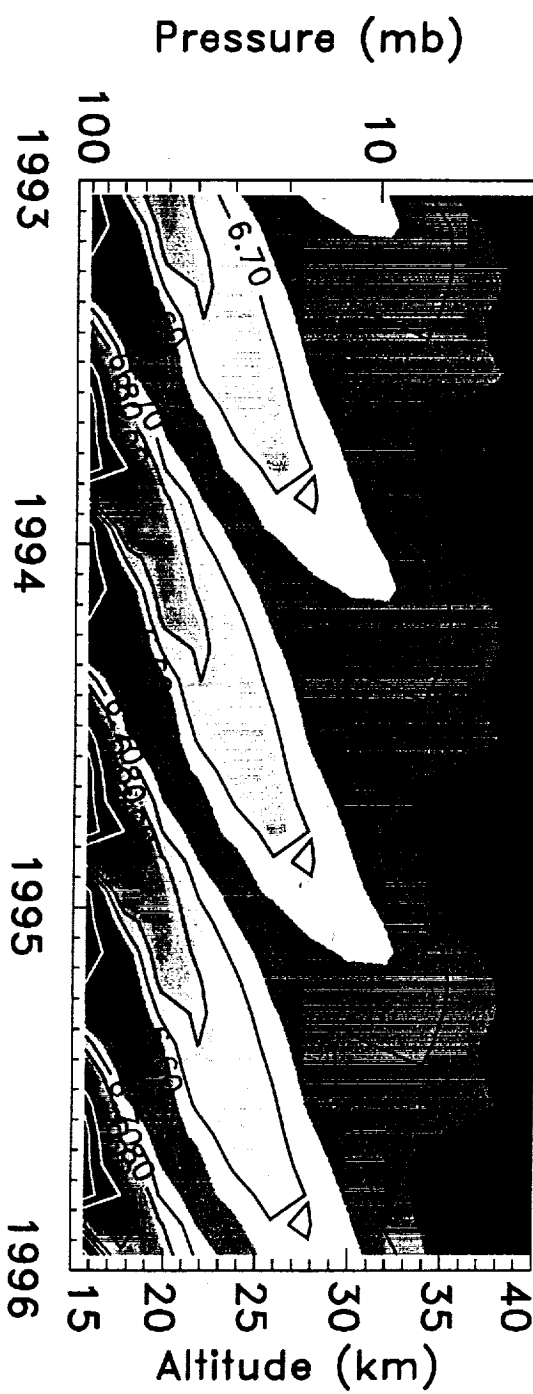


Fig 8

## Annual Cycle of $2\text{CH}_4 + \text{H}_2\text{O}$ at Equator

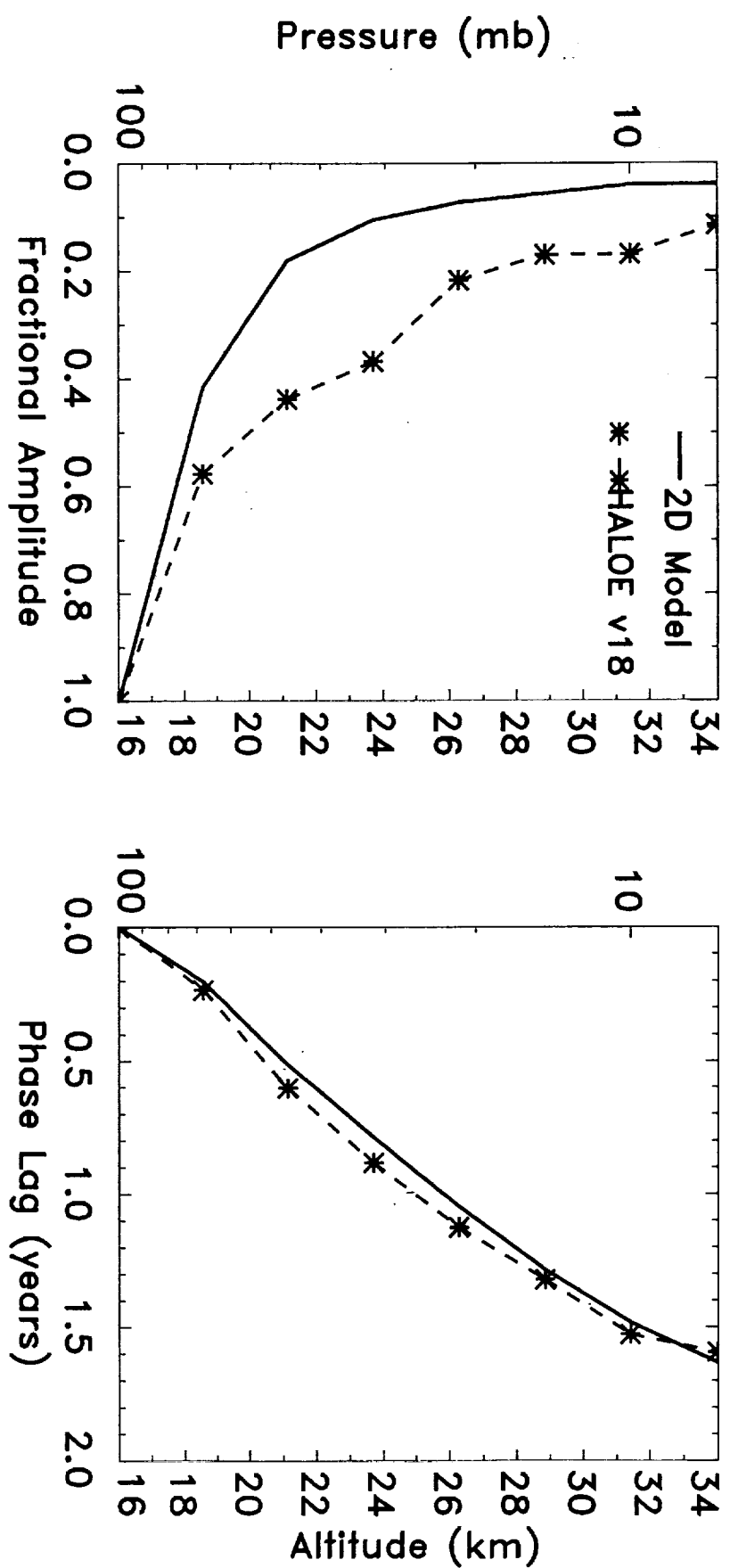
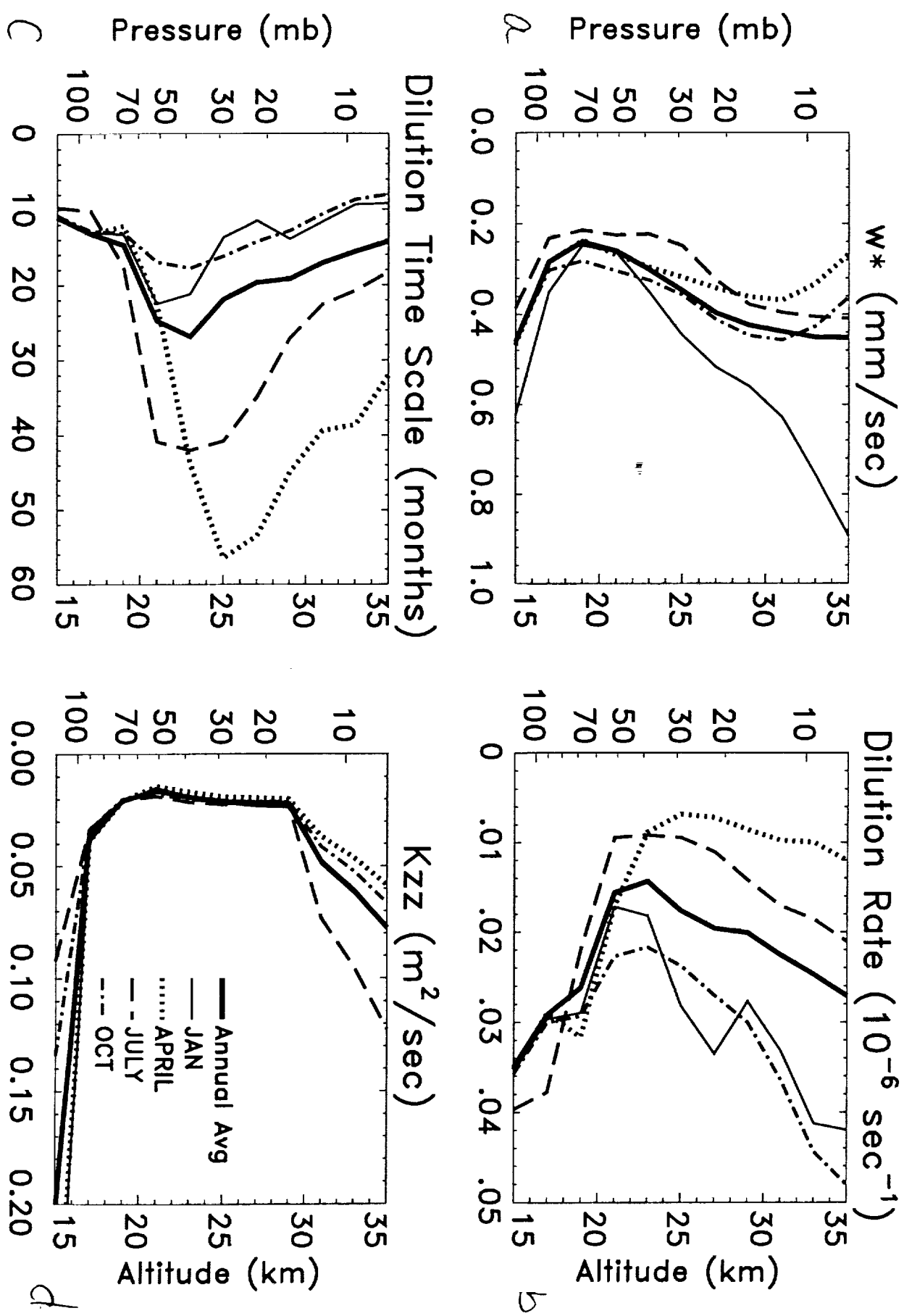


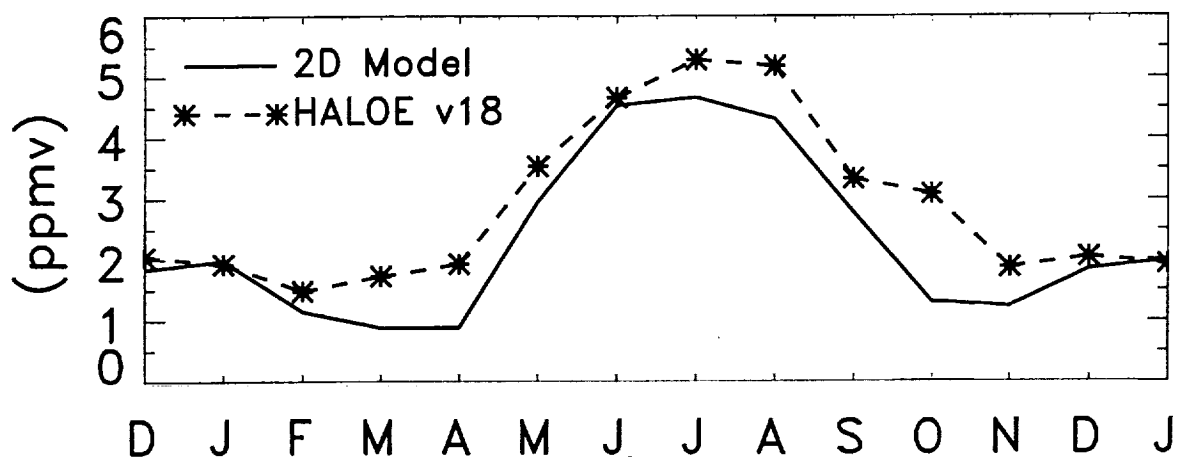
FIG 9

## 2D Model Equator

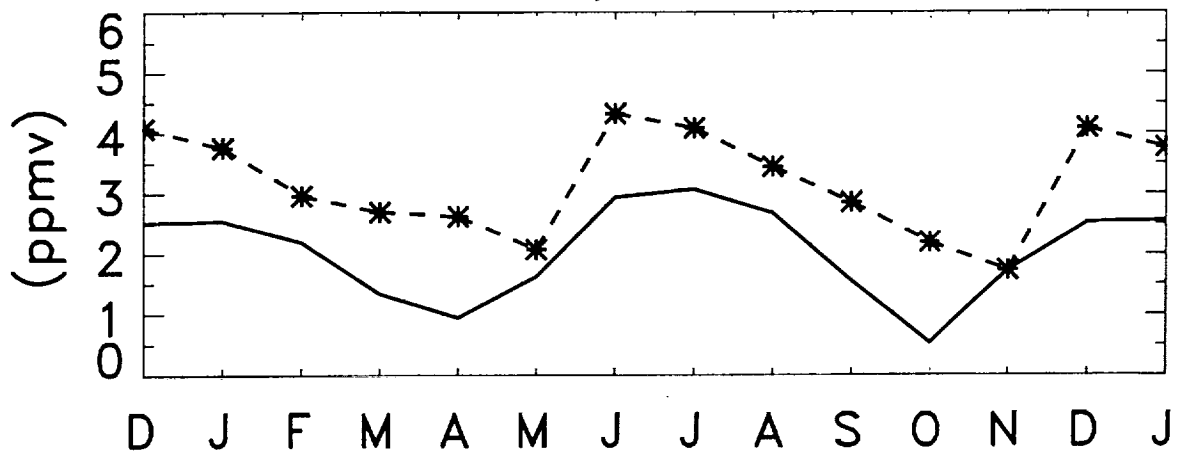


$\text{H}_2\text{O}$  (ppmv) 80 km (.01 mb)

45°N



Equator



45°S

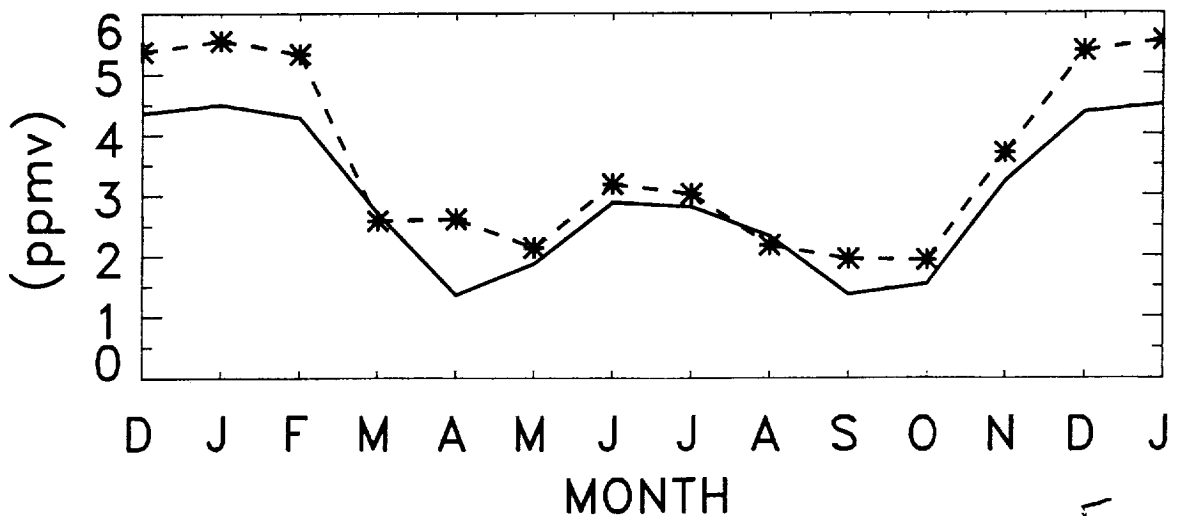


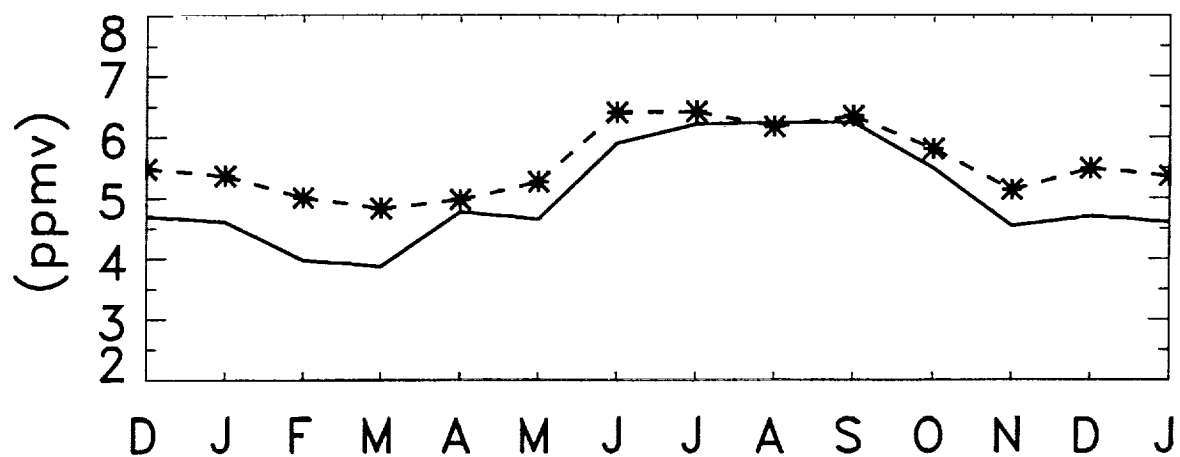
FIG 11

*300 mb, 65 km*

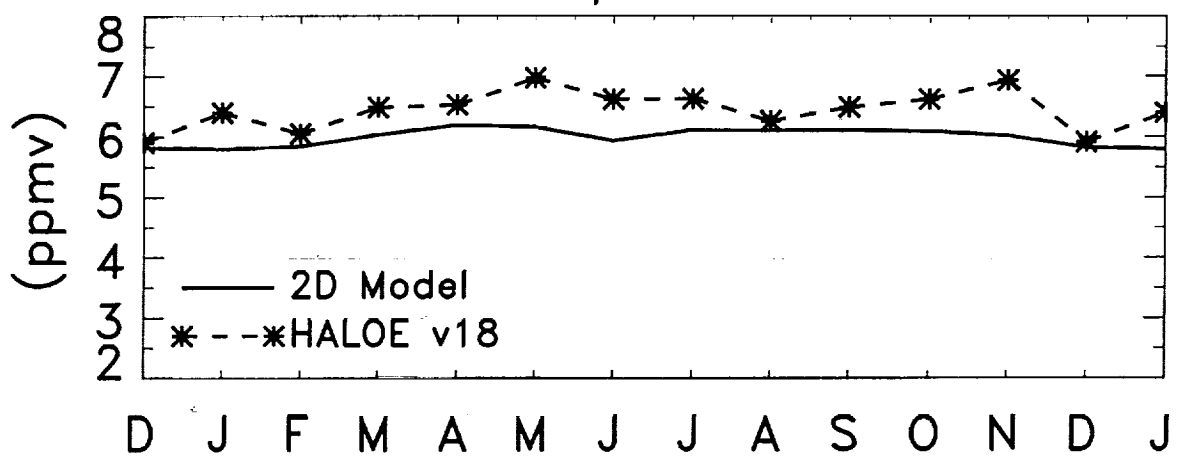
# $\text{H}_2\text{O}$ (ppmv) 65 km (.1 mb)

✓

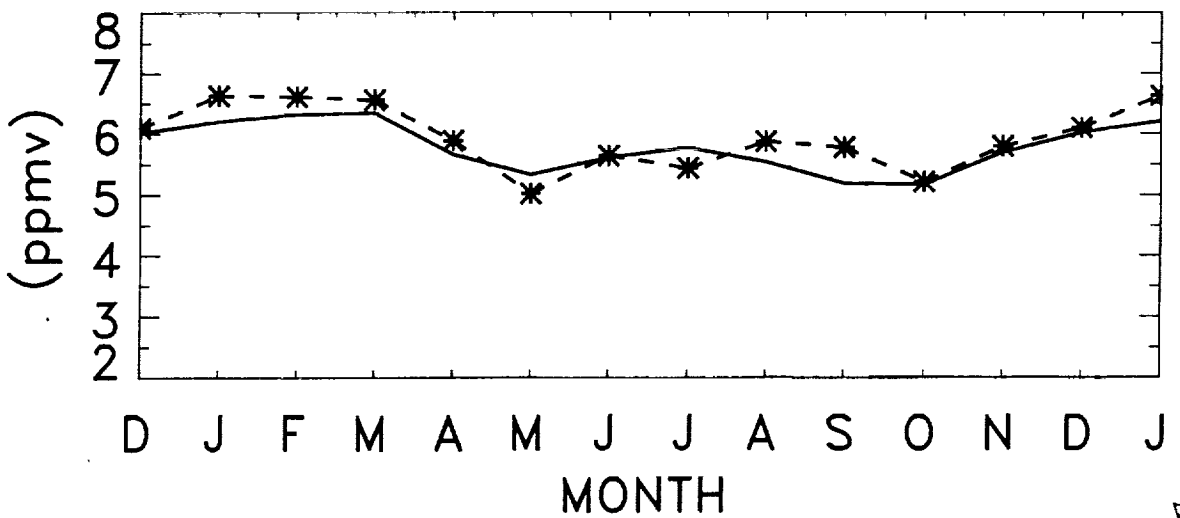
45°N



Equator

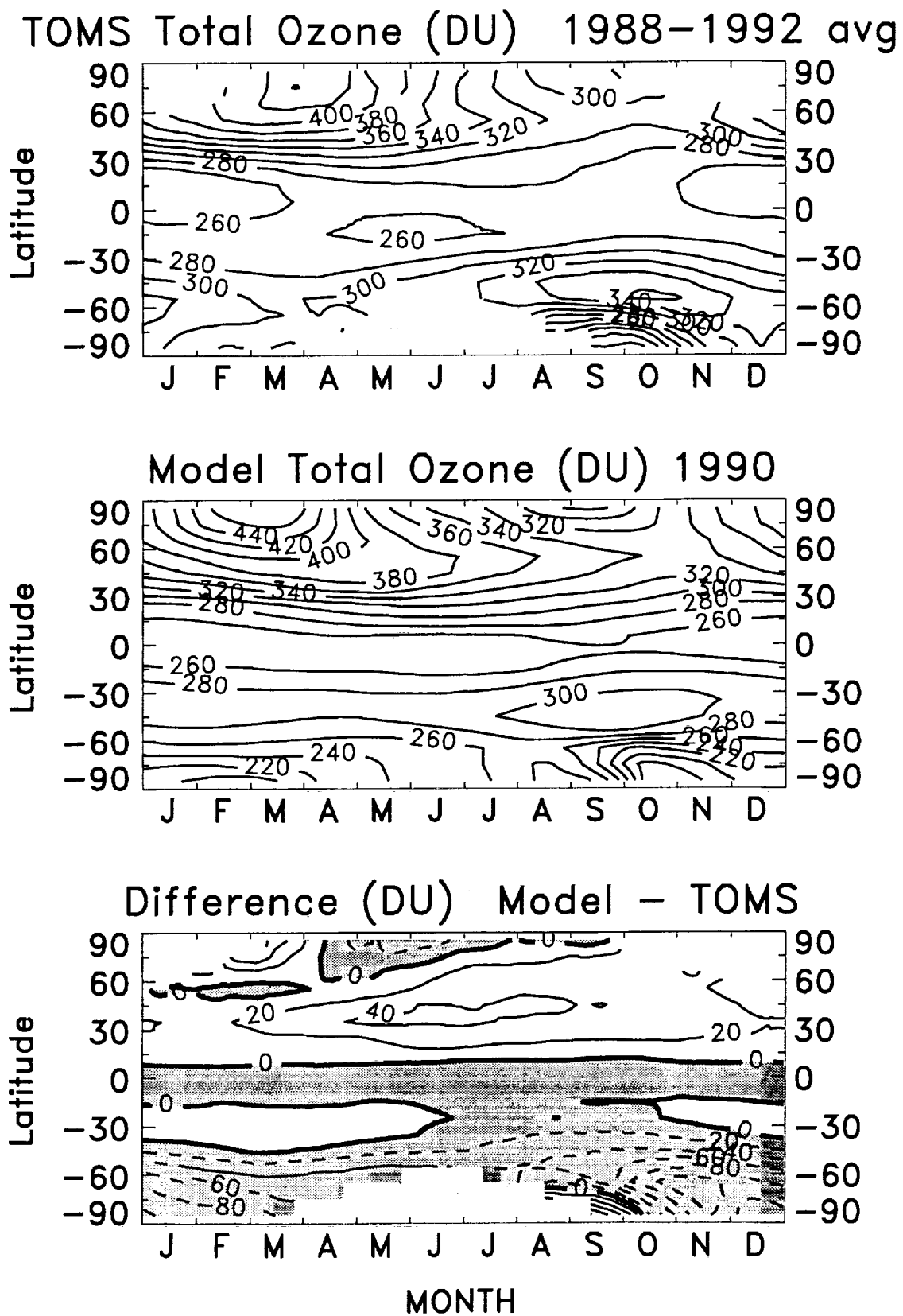


45°S



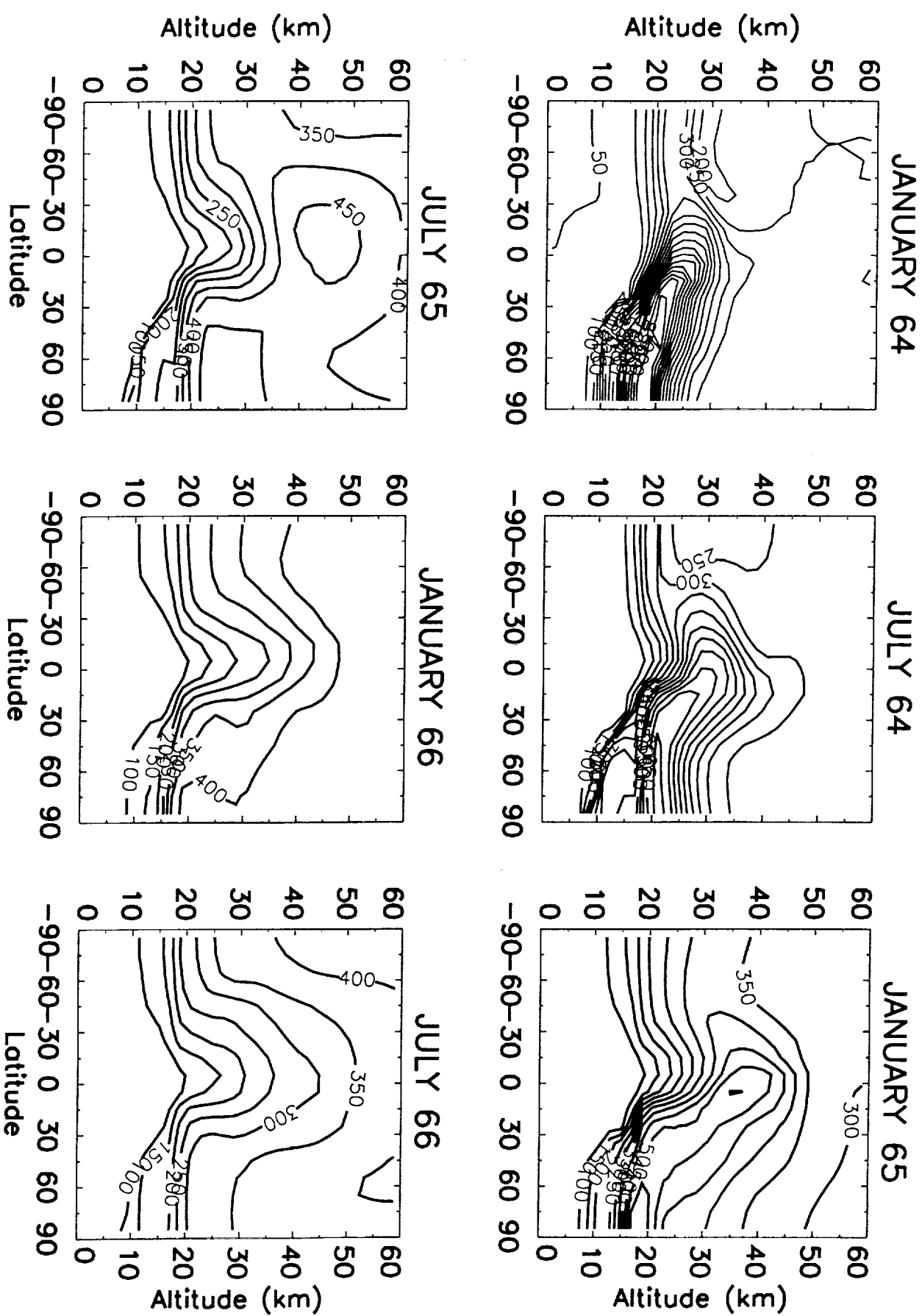
MONTH

FIG 12

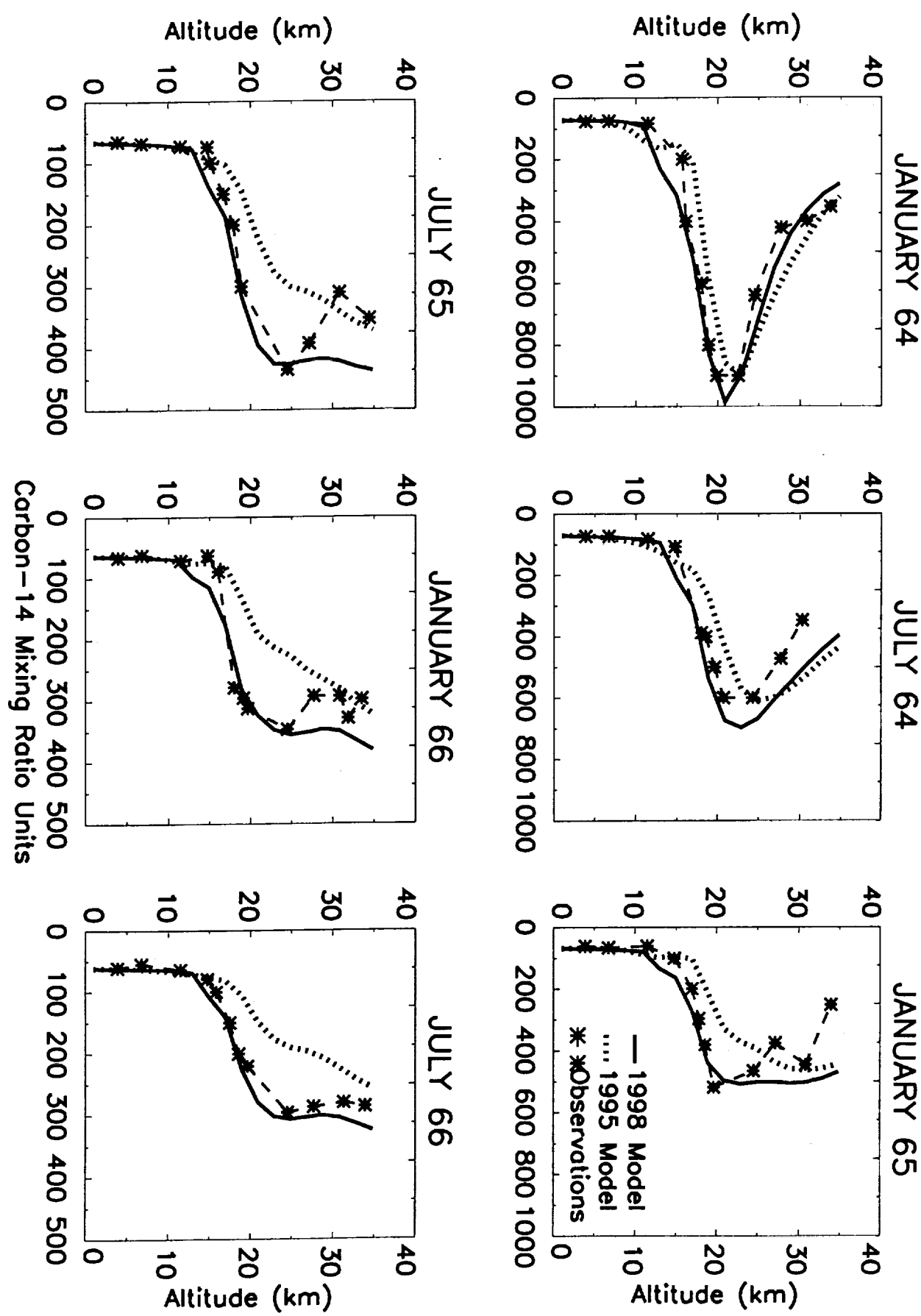


Carbon-14 (Mixing Ratio Units)

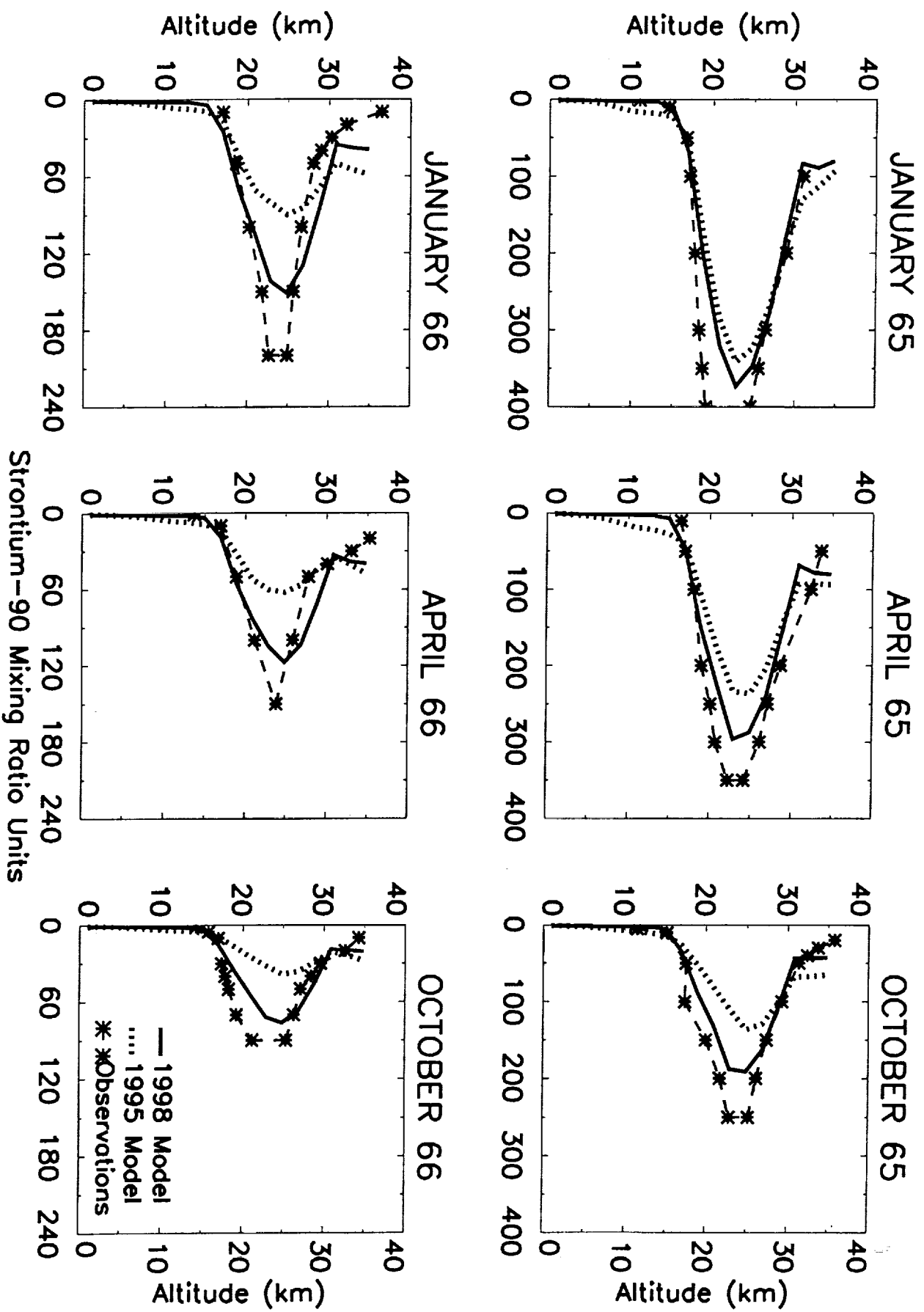
104



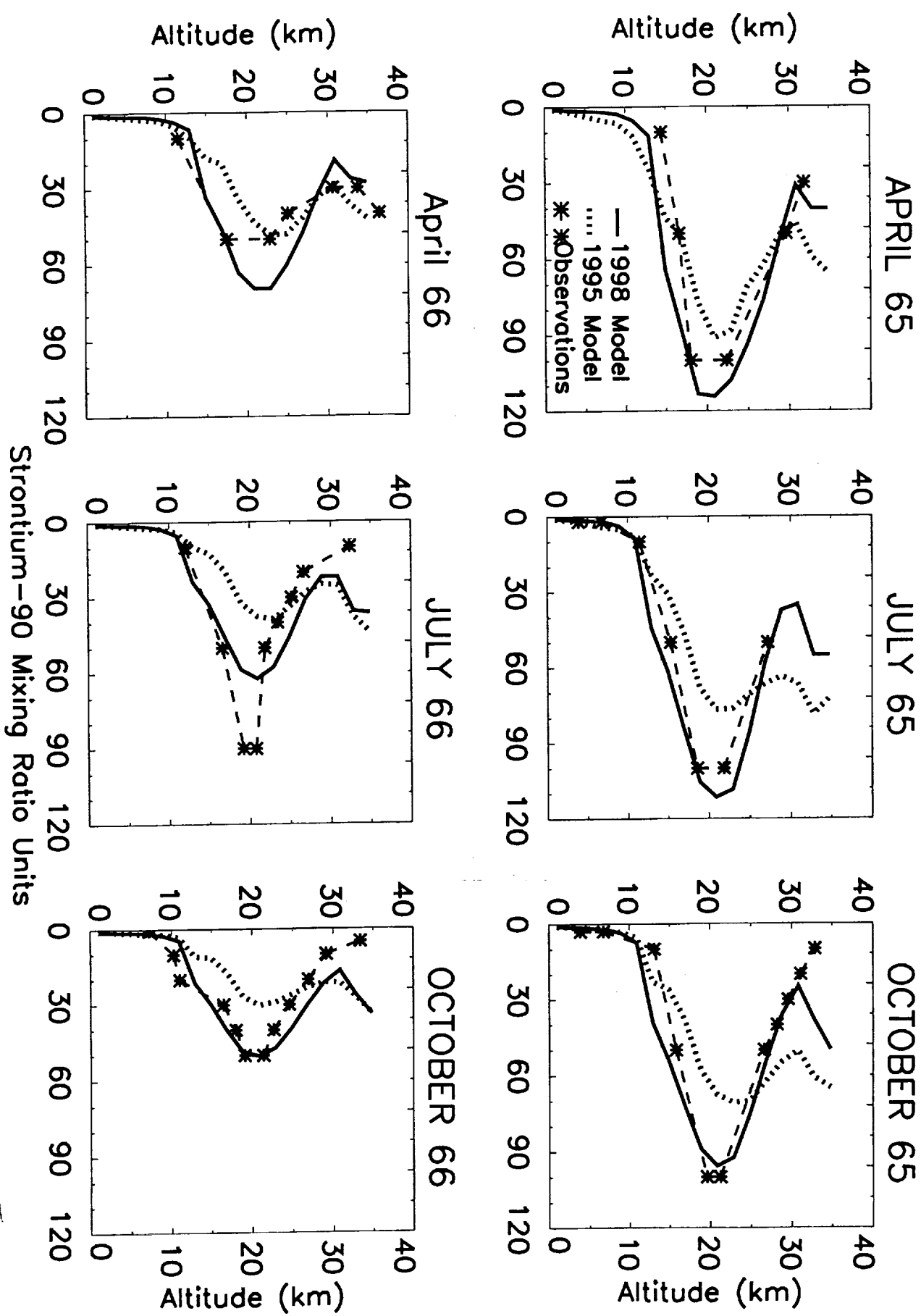
# Carbon-14 (Mixing Ratio Units) 31°N



Strontium-90 (Mixing Ratio Units) 9°N



# Strontium-90 (Mixing Ratio Units) 34°S



# MEAN AGE (Years)

JANUARY

APRIL

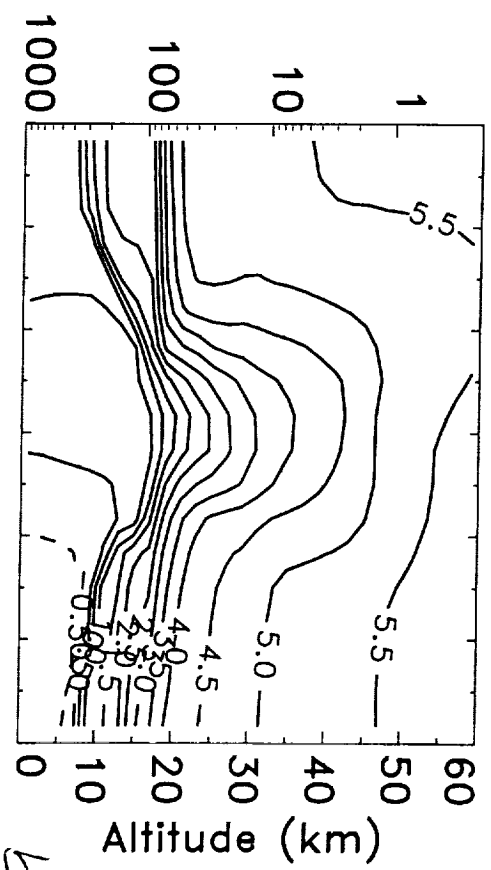
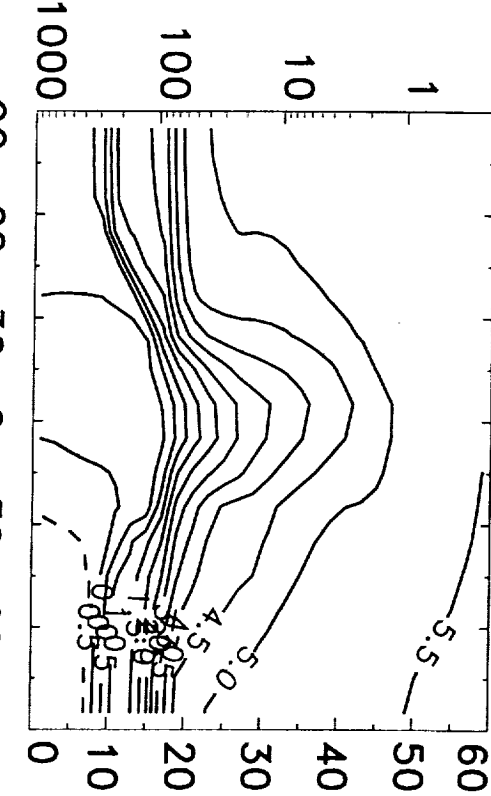
JULY

OCTOBER

Pressure (mbar)

b

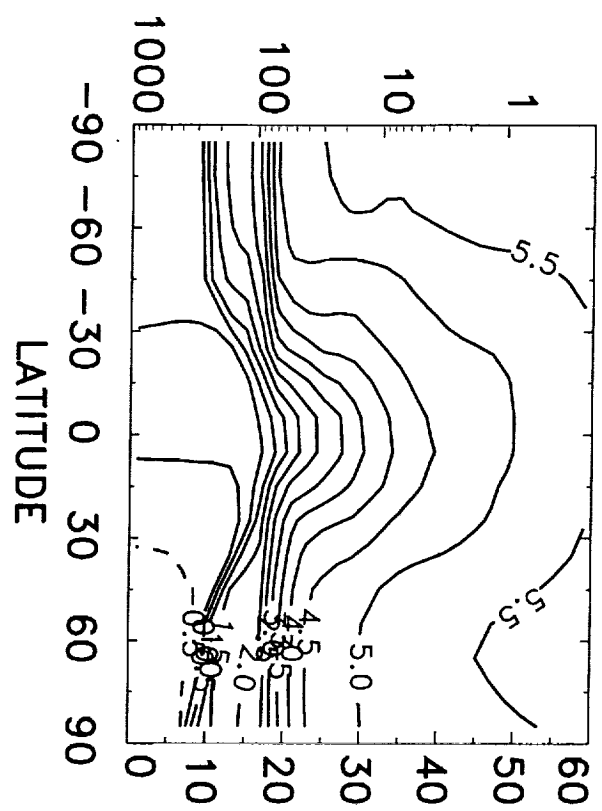
a



Pressure (mbar)

c

Altitude (km)



LATITUDE

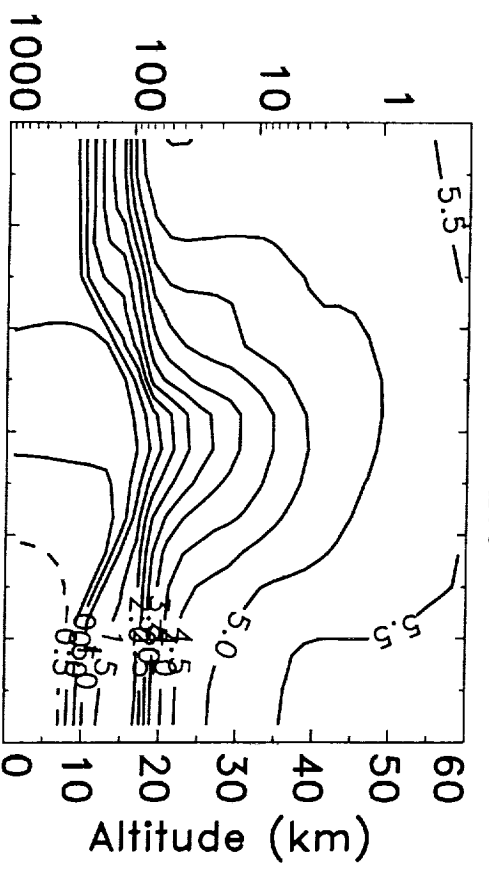


FIG. 18

d

LATITUDE

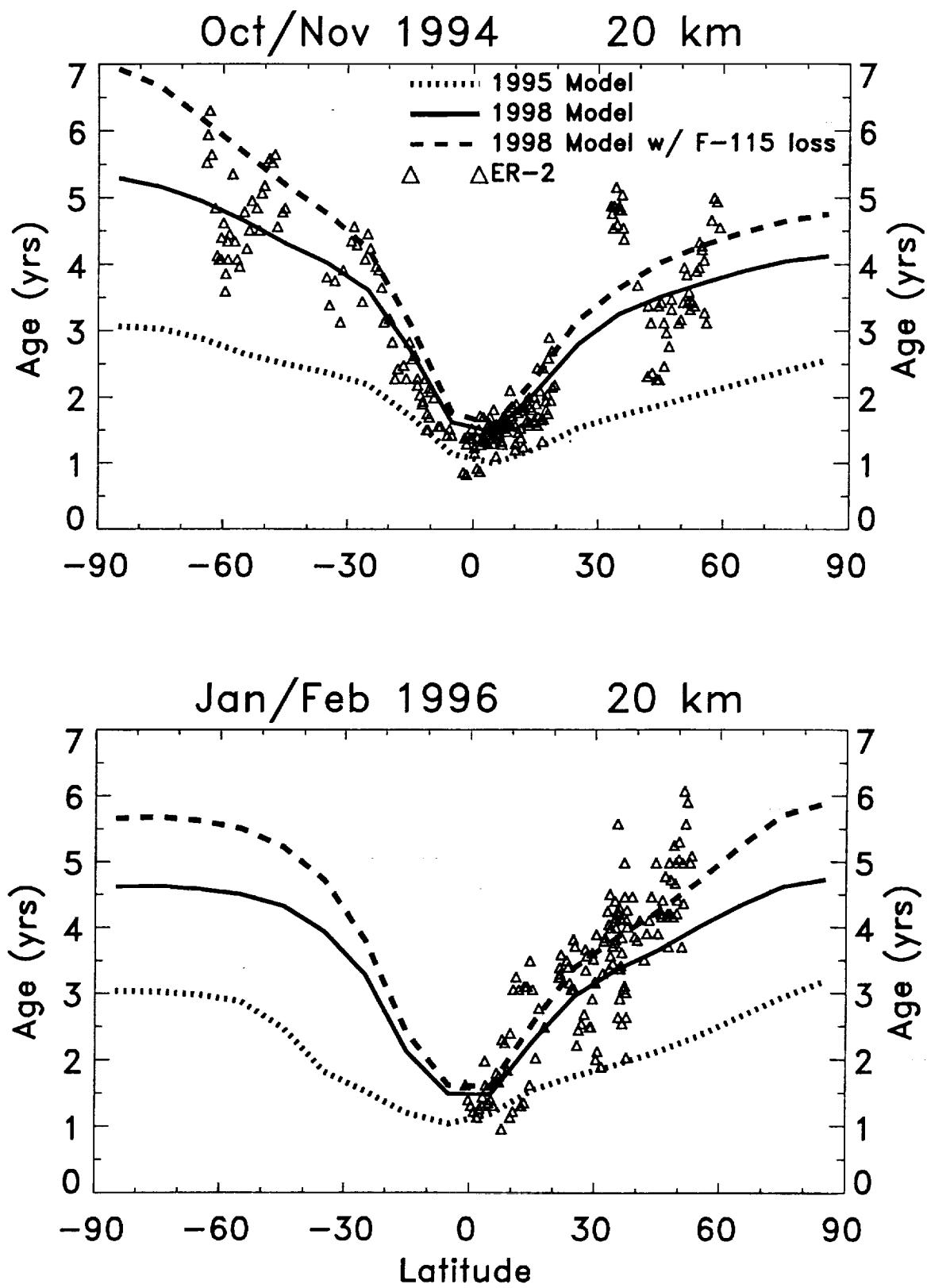
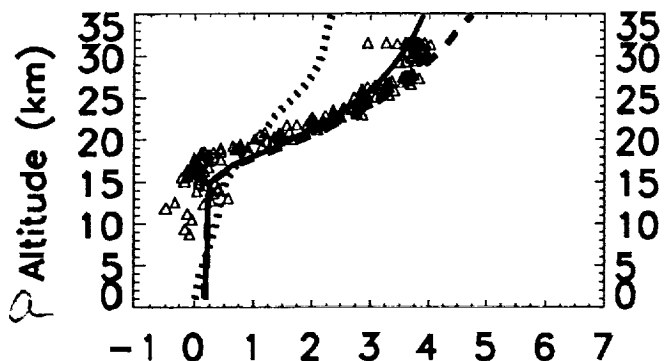


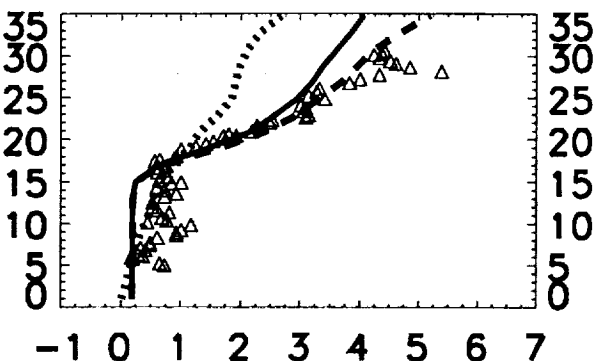
Fig 19

... 1995 Model  
 — 1998 Model  
 - - 1998 Model w/ CFC-115 loss  
 \* \* Harnisch et al., 1996 SF<sub>6</sub>  
 □ □ Harnisch et al., 1996 SF<sub>6</sub>  
 △ △ OMS SF<sub>6</sub>

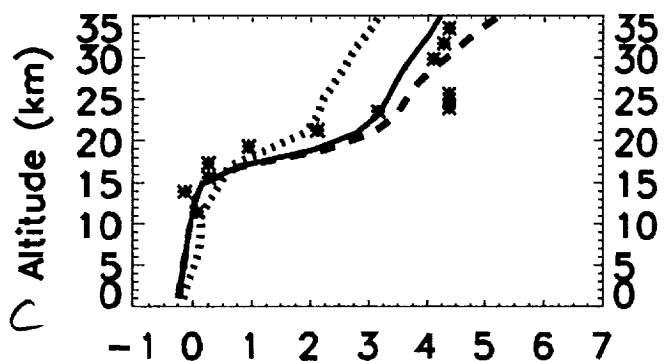
Feb 7°S



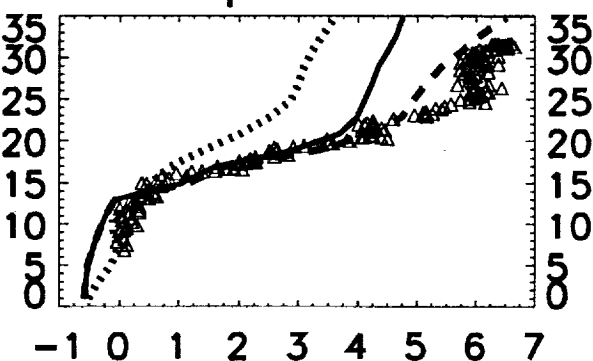
Nov 7°S



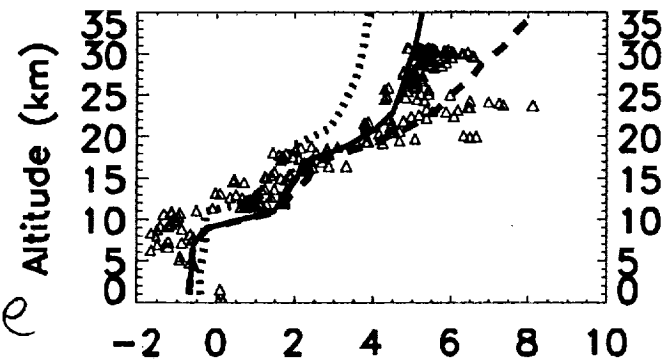
March 17°N



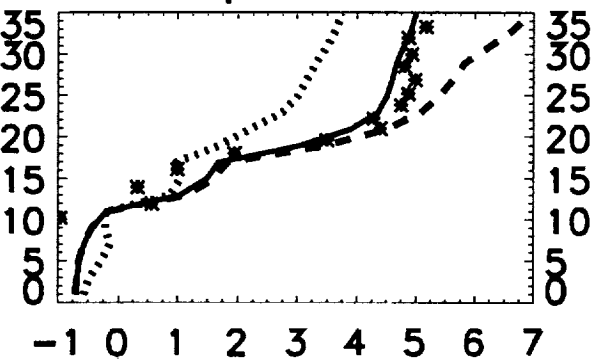
Sept 35°N



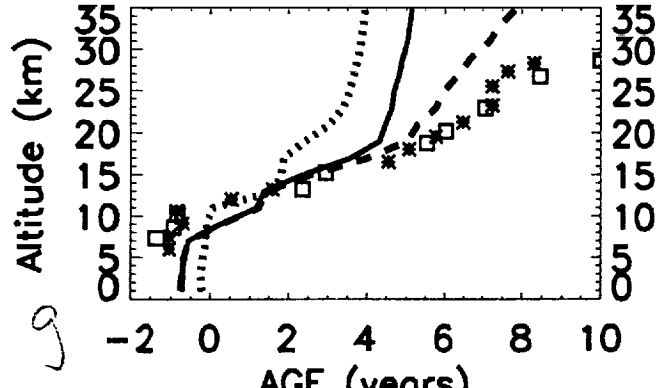
June 65°N



Sept 44°N



Jan/Feb 68°N



March 68°N

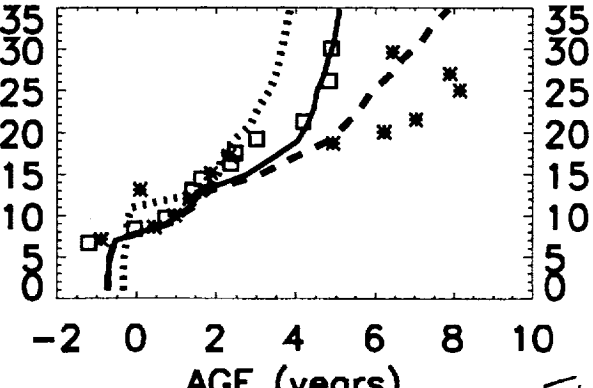


FIG 20

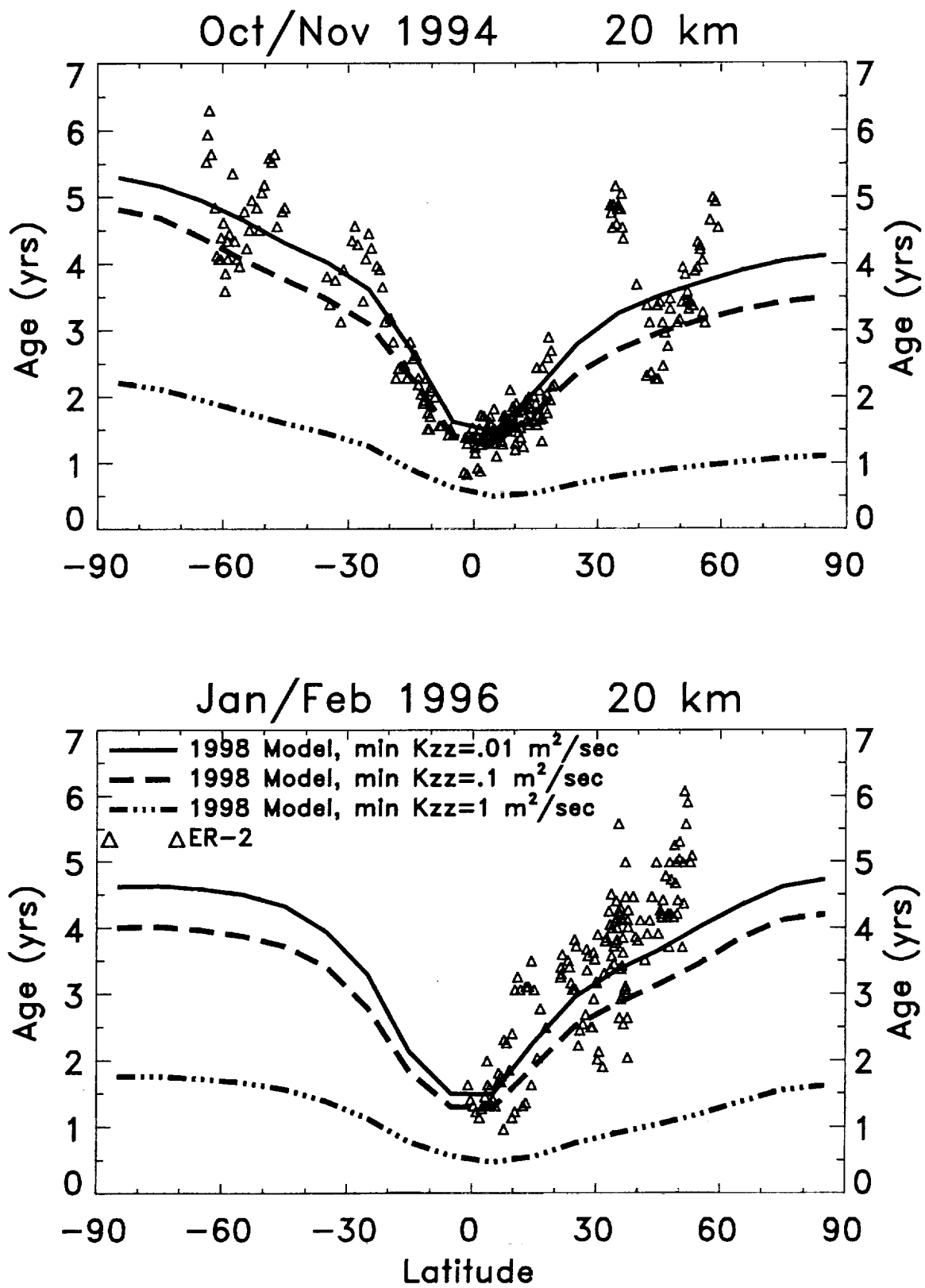
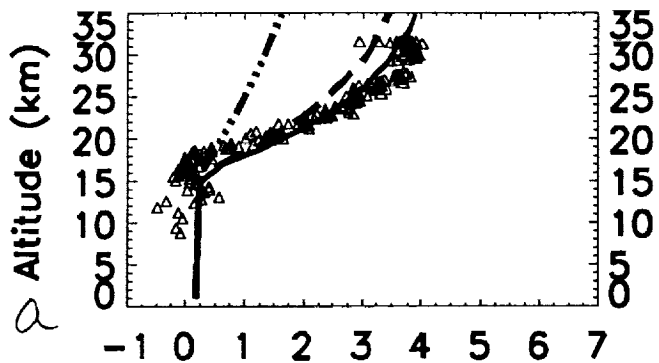


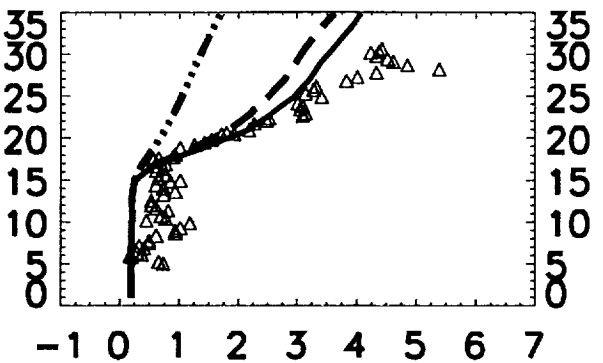
FIG 21

— 1998 Model, min  $K_{zz} = .01 \text{ m}^2/\text{sec}$   
 — 1998 Model, min  $K_{zz} = .1 \text{ m}^2/\text{sec}$   
 - - 1998 Model, min  $K_{zz} = 1 \text{ m}^2/\text{sec}$   
 \* Hornisch et al., 1996 SF<sub>6</sub>  
 □ Hornisch et al., 1996 SF<sub>6</sub>  
 Δ DMS SF<sub>6</sub>

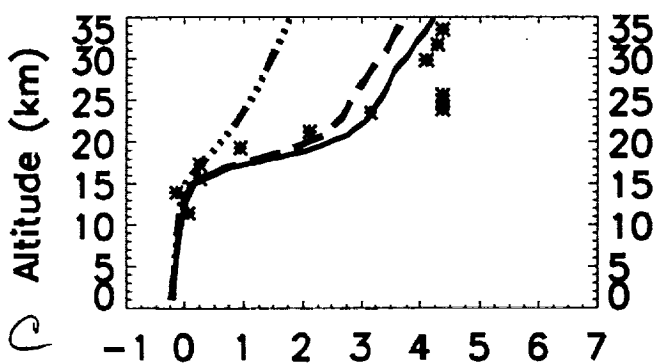
Feb 7°S



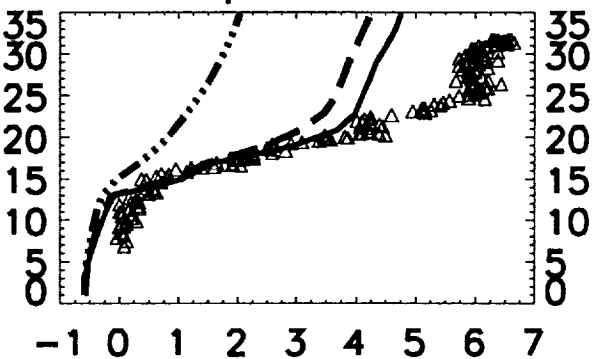
Nov 7°S



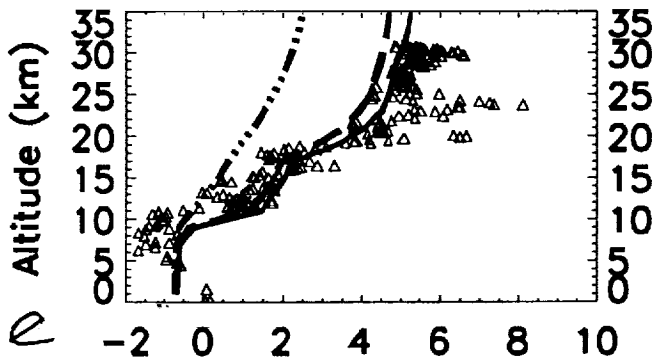
March 17°N



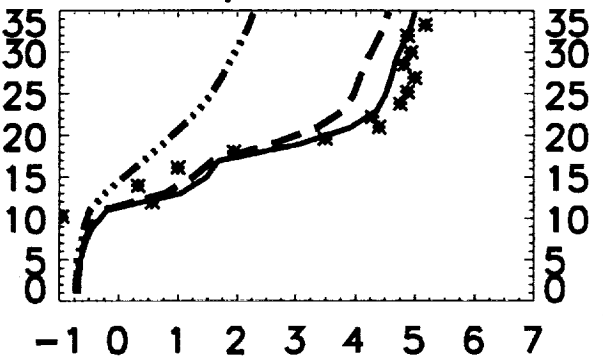
Sept 35°N



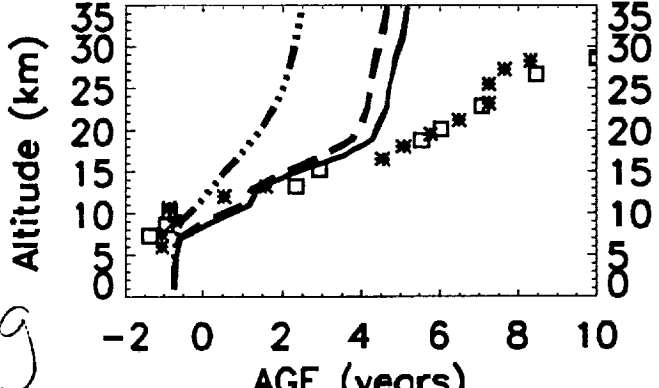
June 65°N



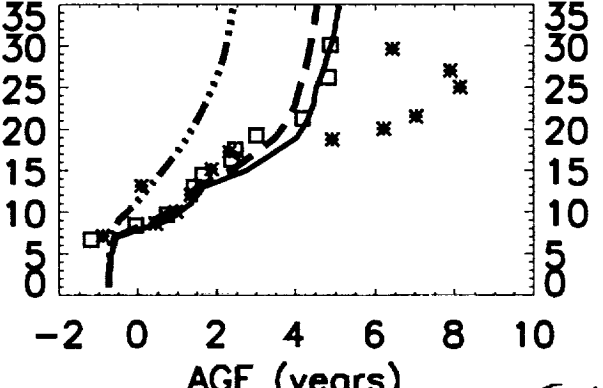
Sept 44°N



Jan/Feb 68°N



March 68°N



F1622

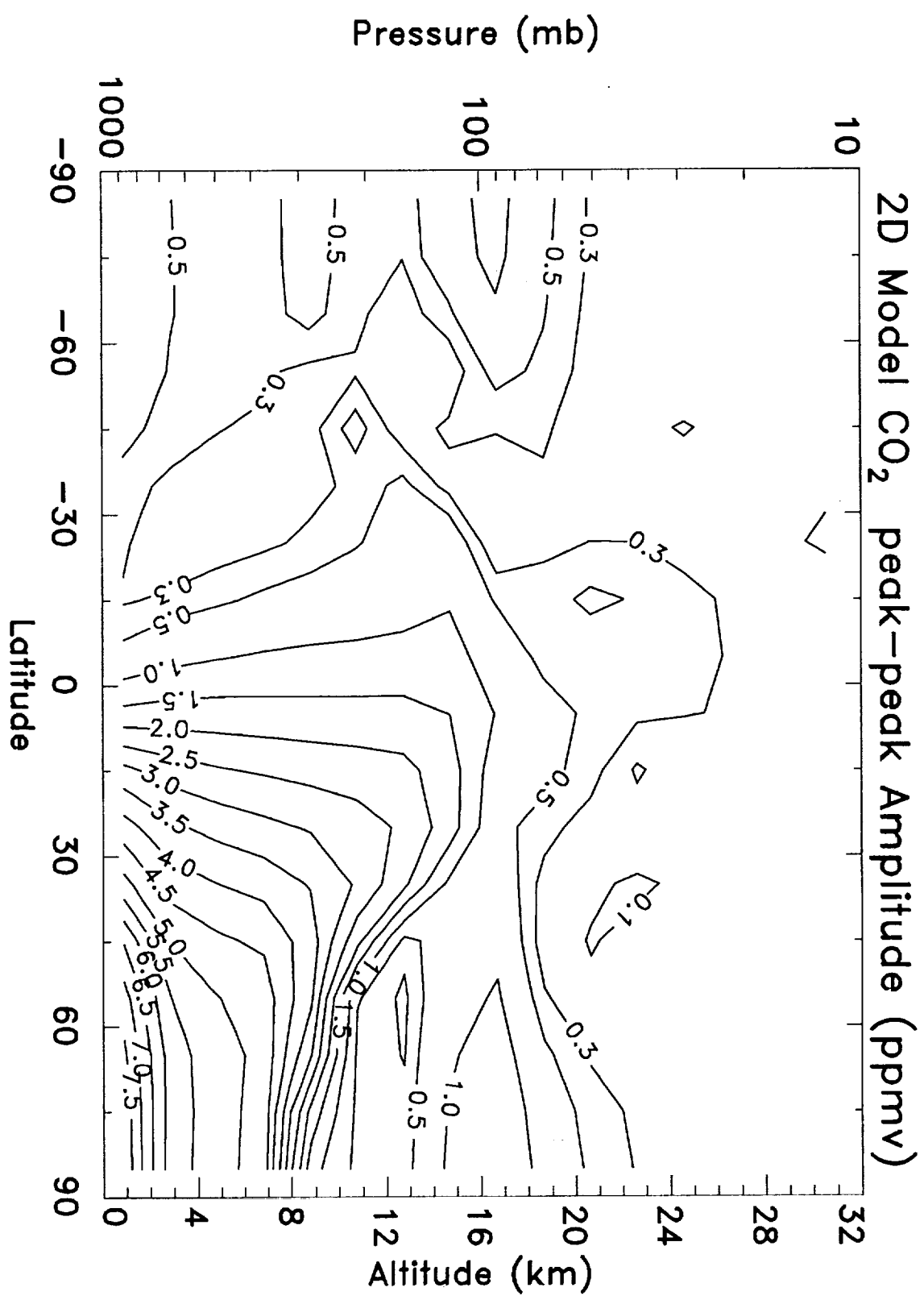


Fig. 23a

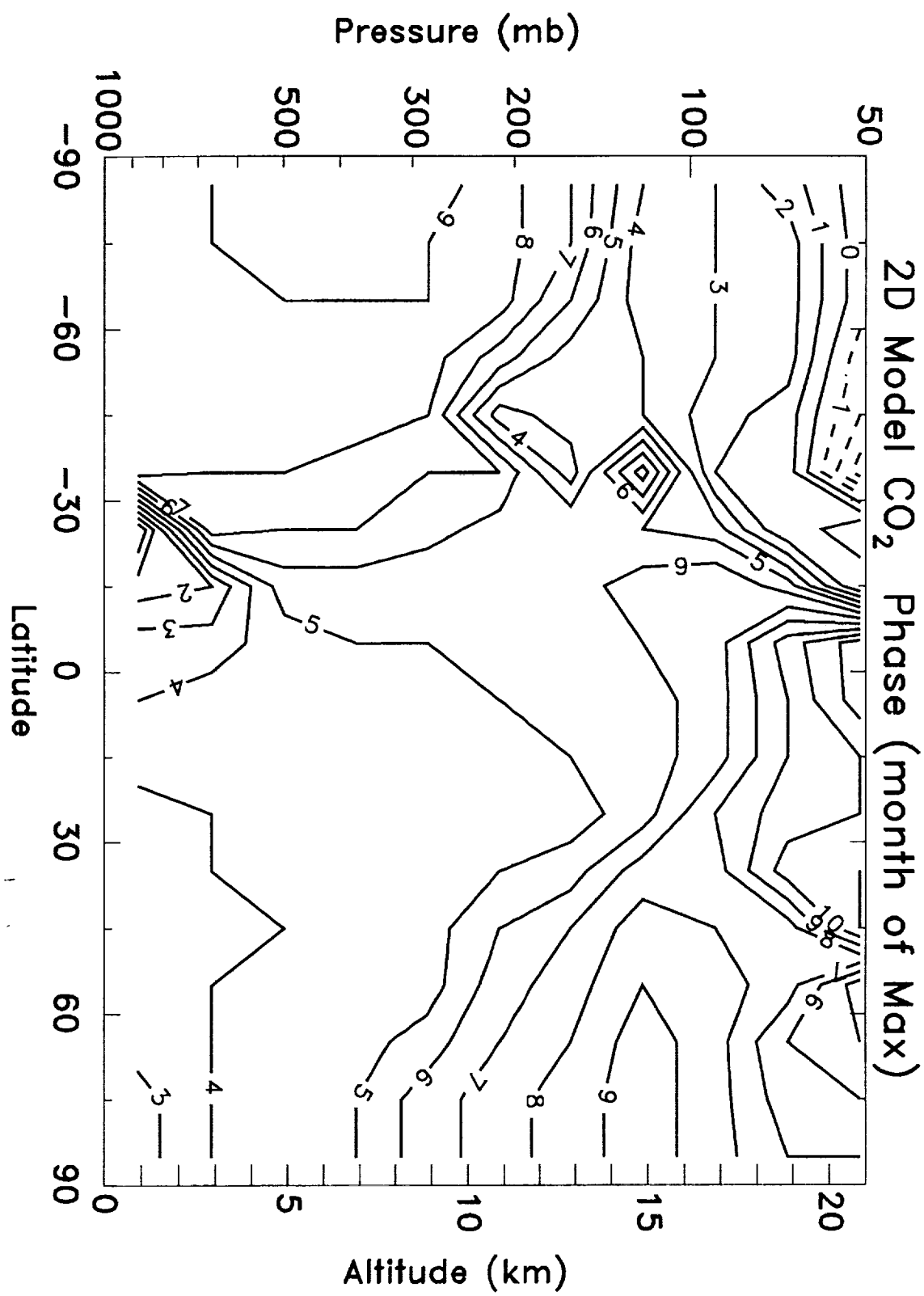
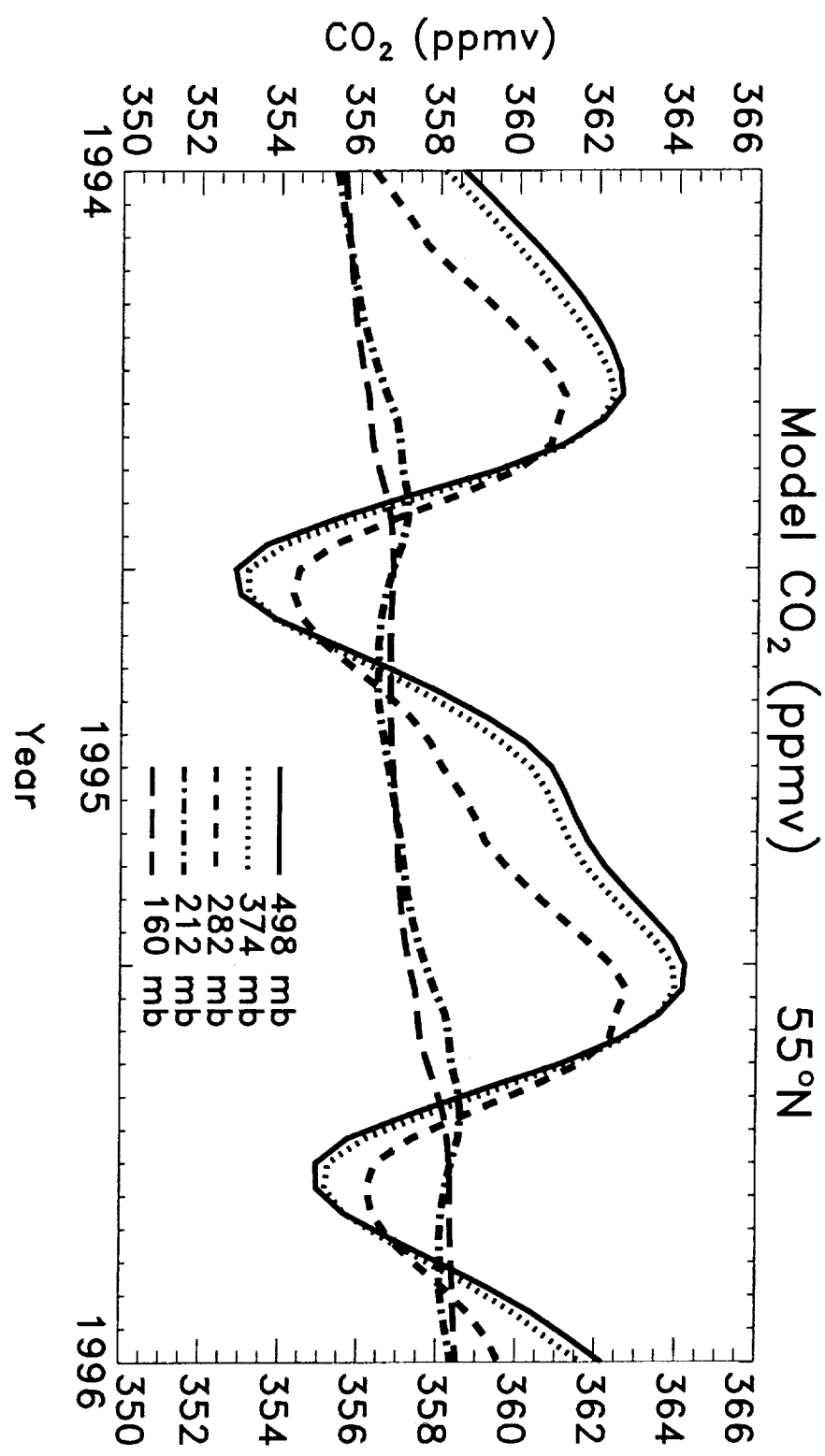
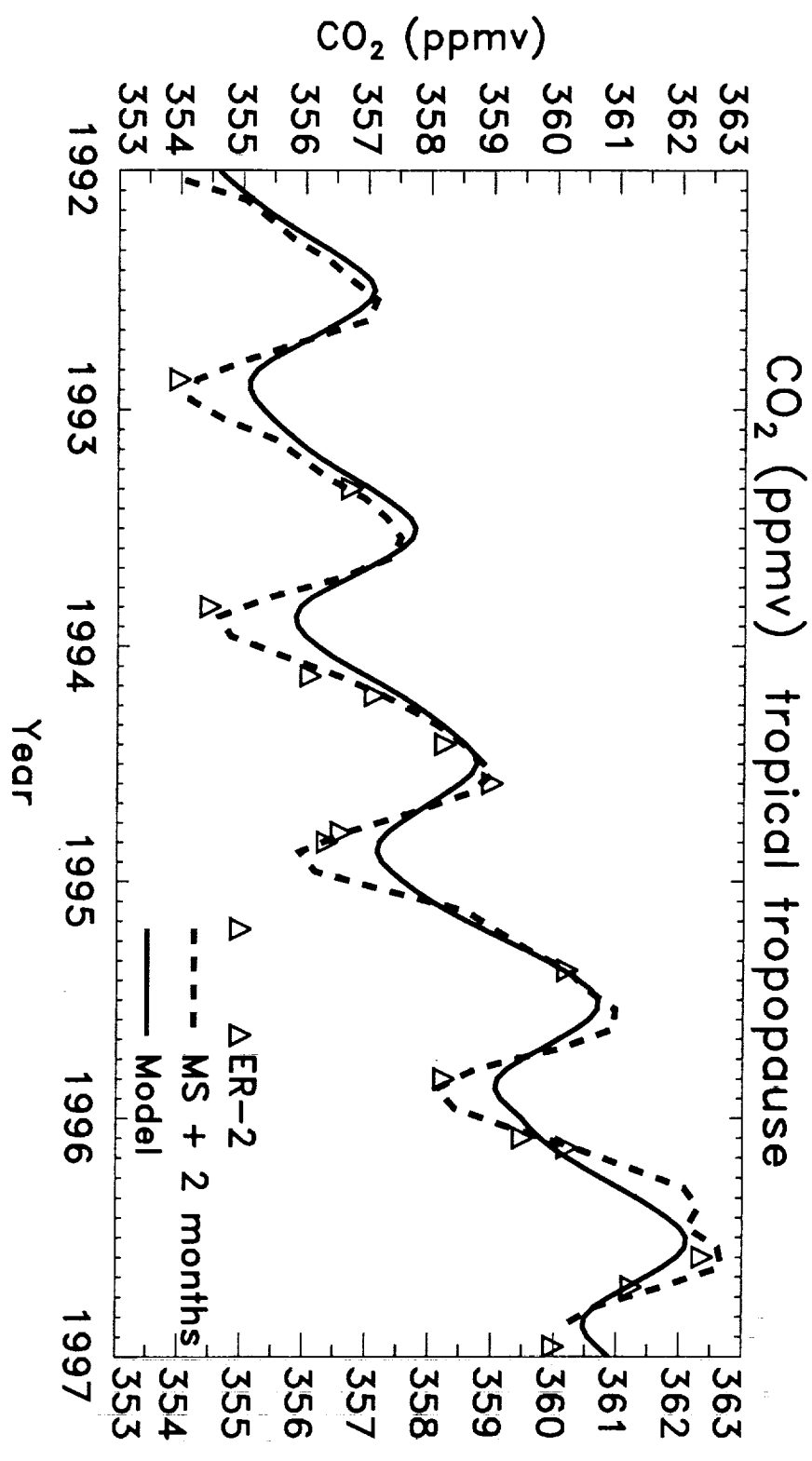
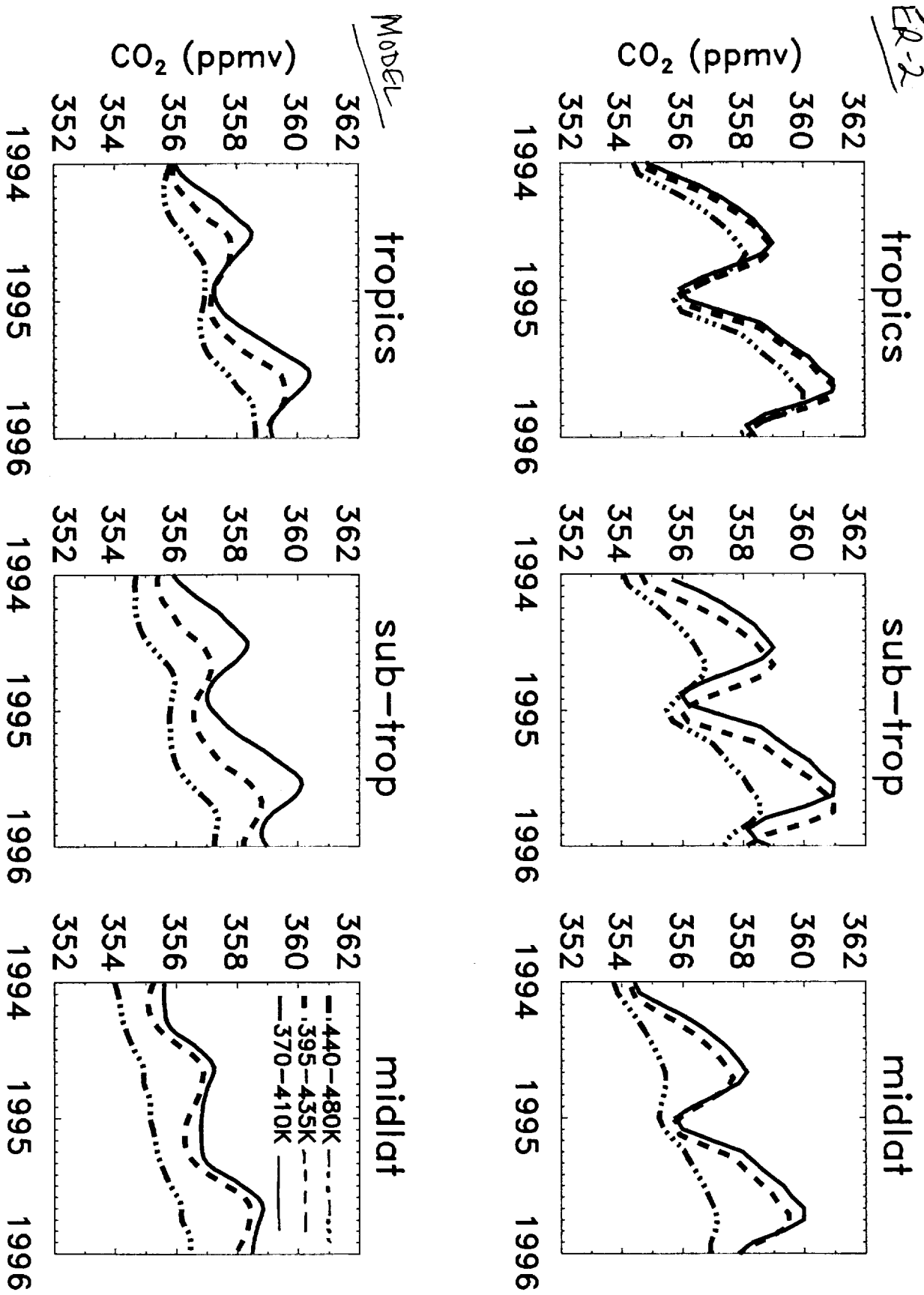
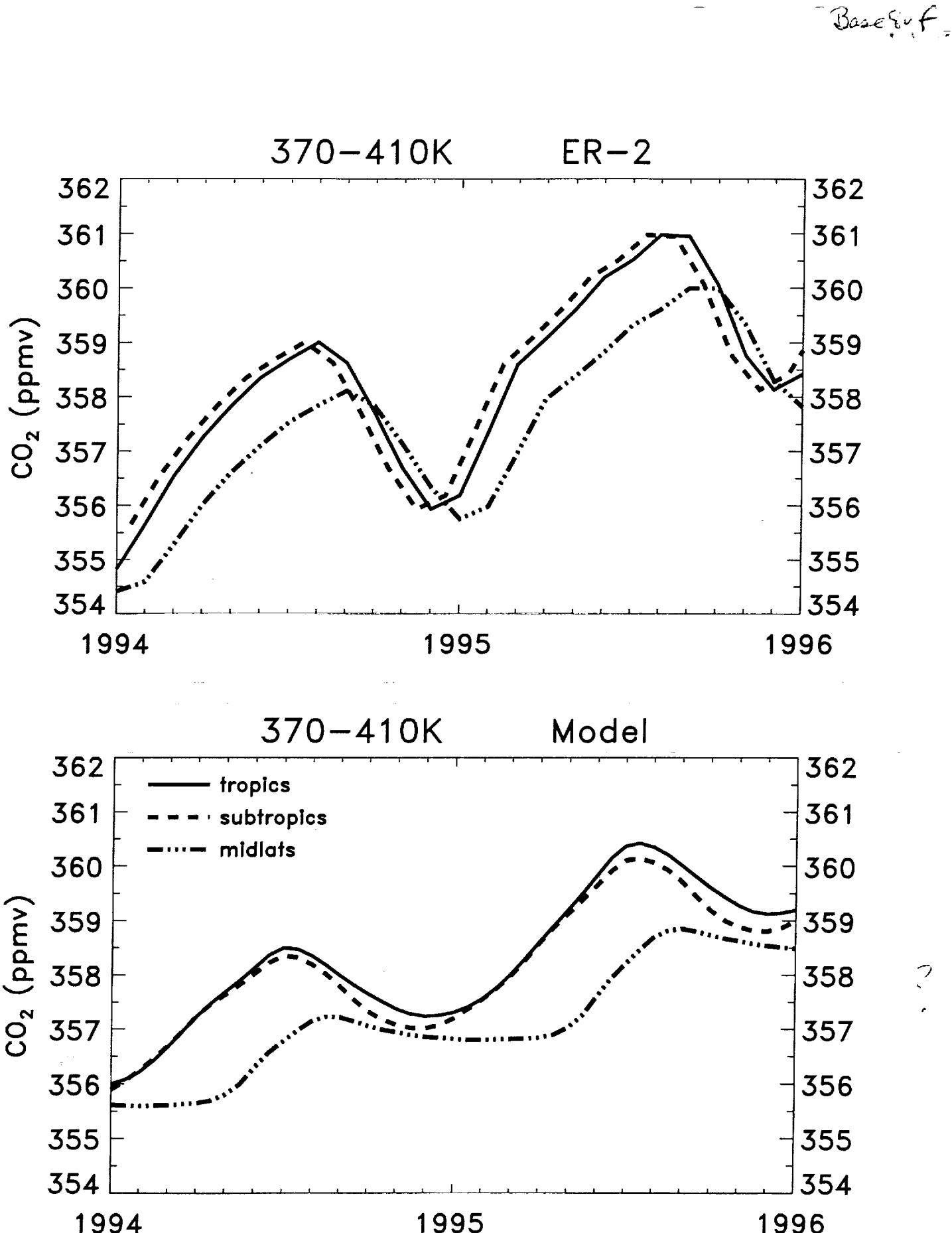


Fig 23b









F16 27

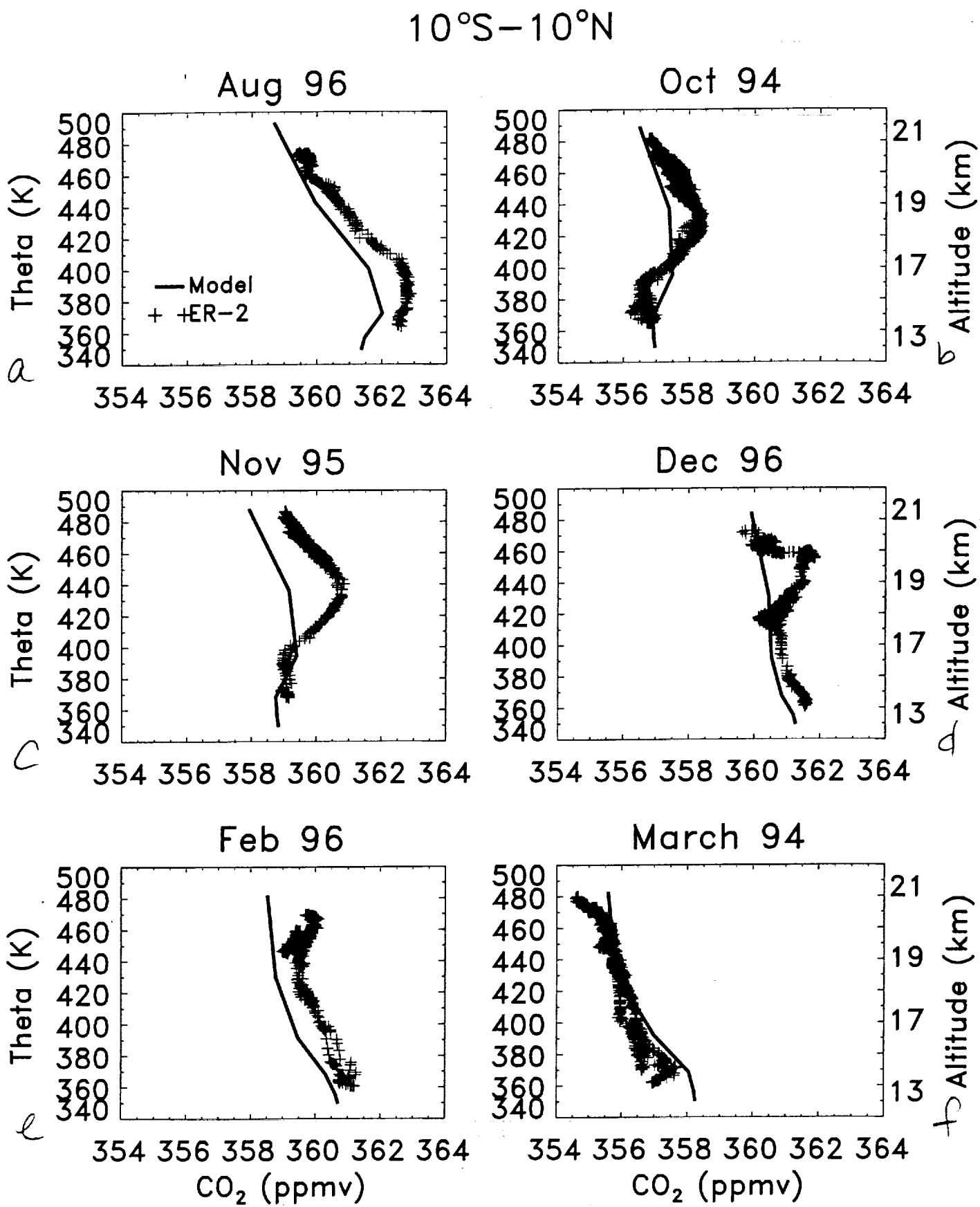


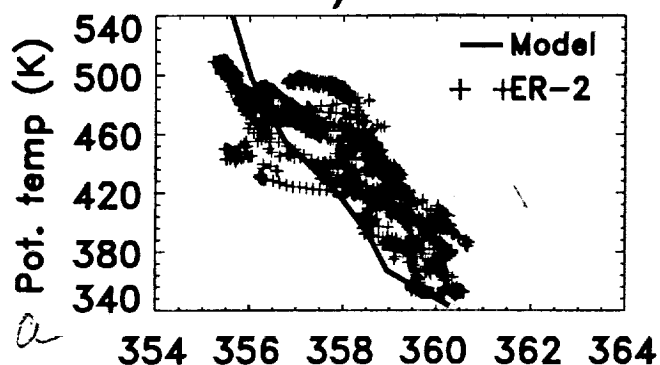
Fig. 28

30°N–40°N

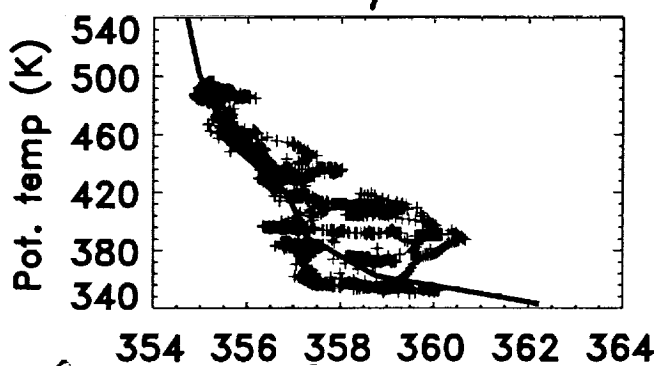
70°S–60°S

base

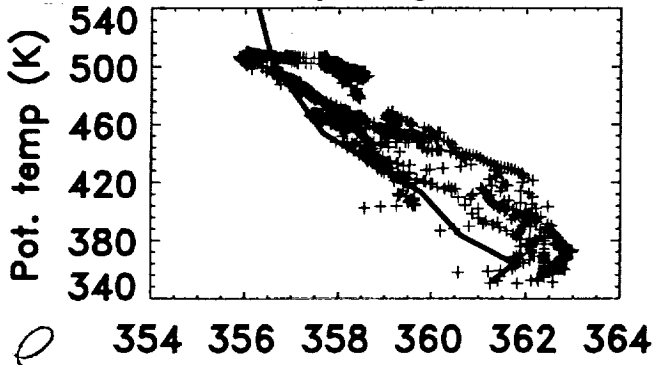
Jan/Feb 96



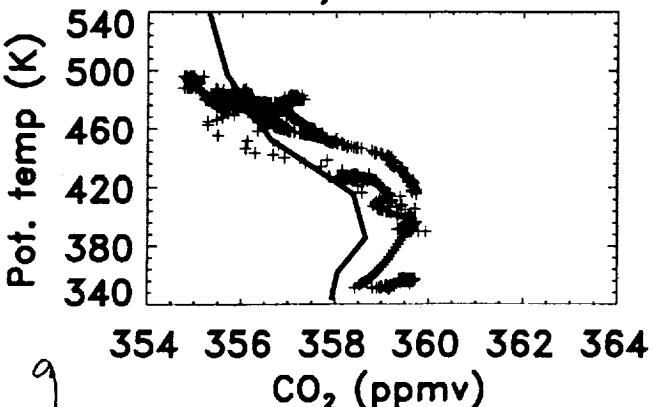
May 95



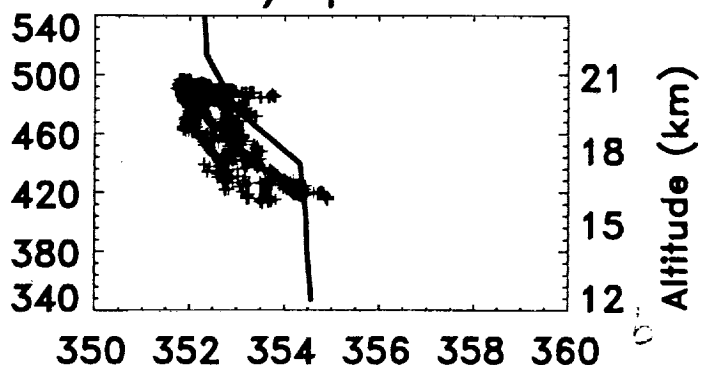
Jul/Aug 96



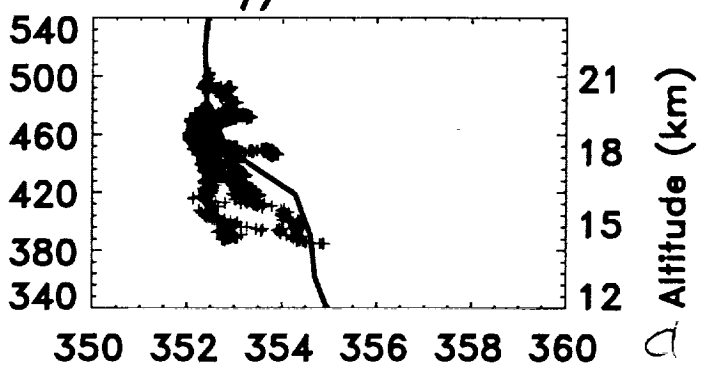
Oct/Nov 95



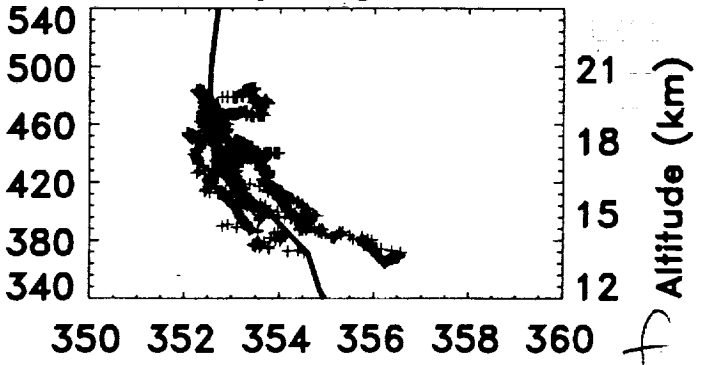
Mar/April 94



May/June 94



Jul/Aug 94



Oct 94

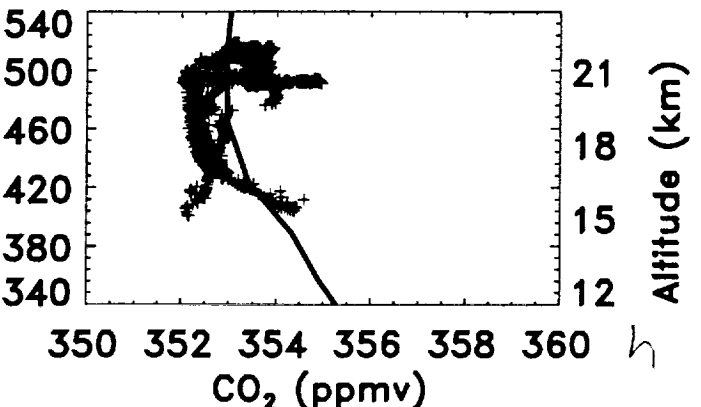


Fig 29

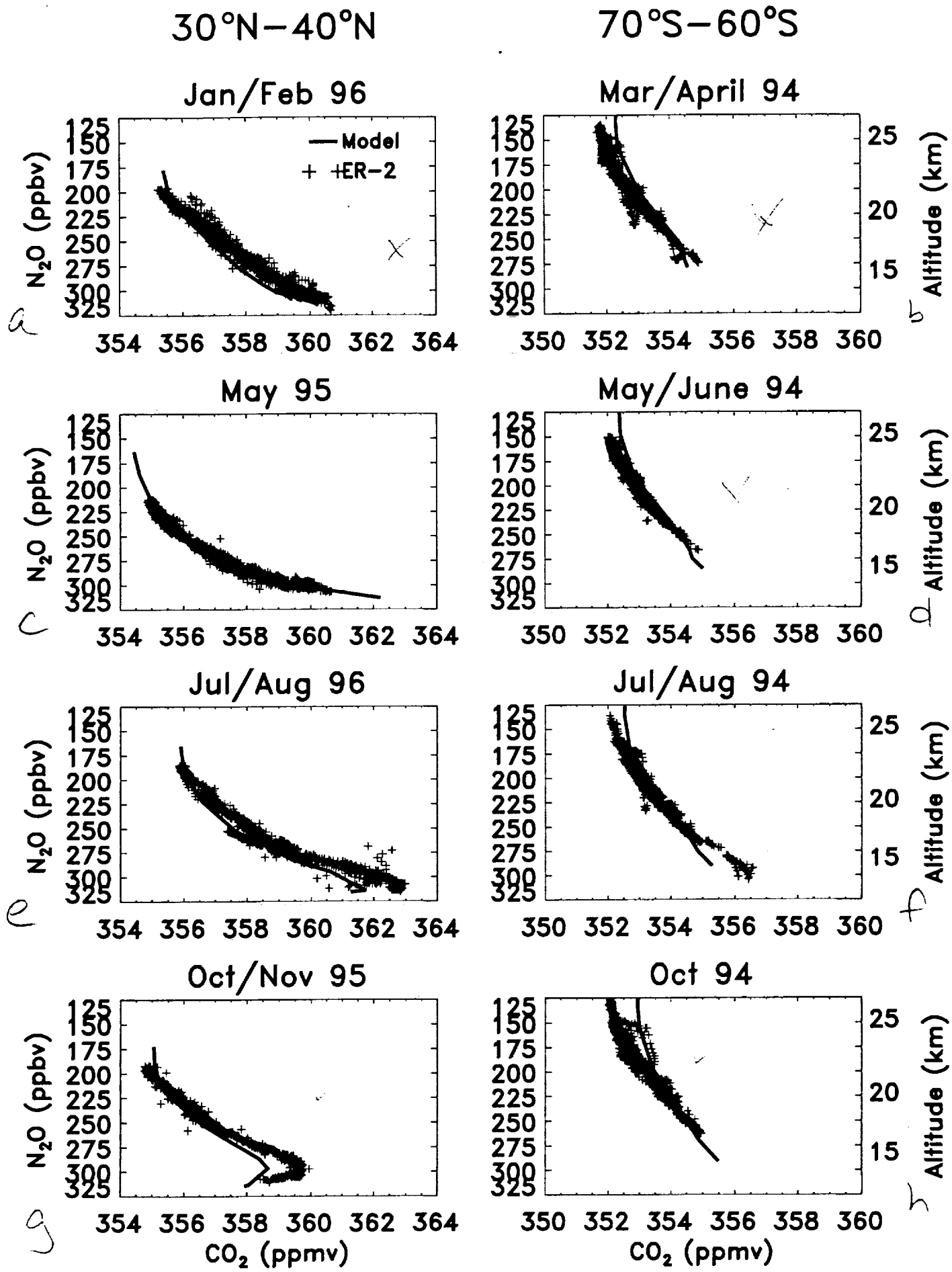
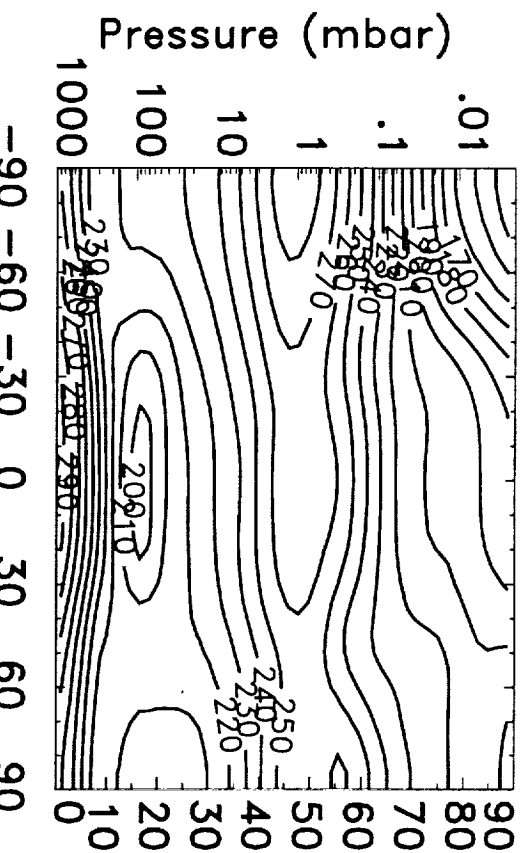


FIG 30

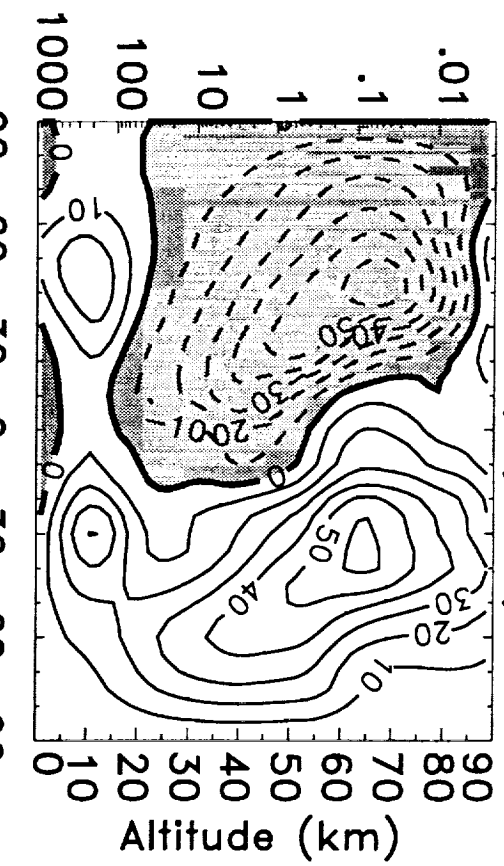
# JANUARY

FIG. A.1

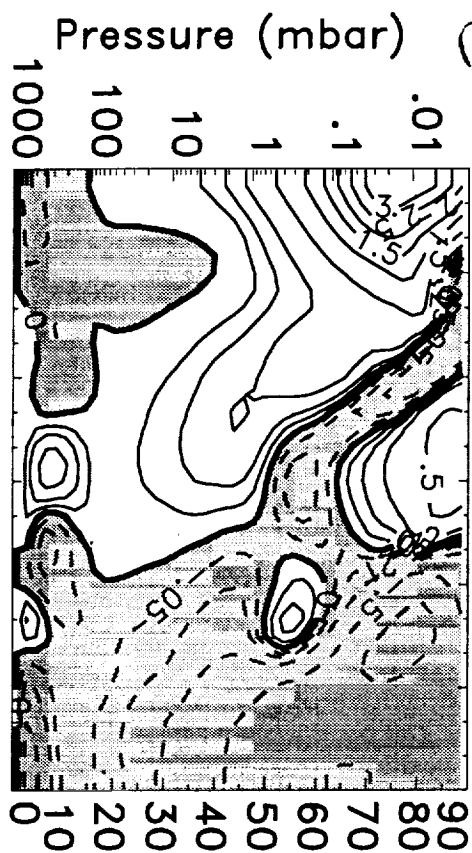
a TEMP (K)



b UBAR (m/sec)



c  $w^*$  (cm/sec)



d

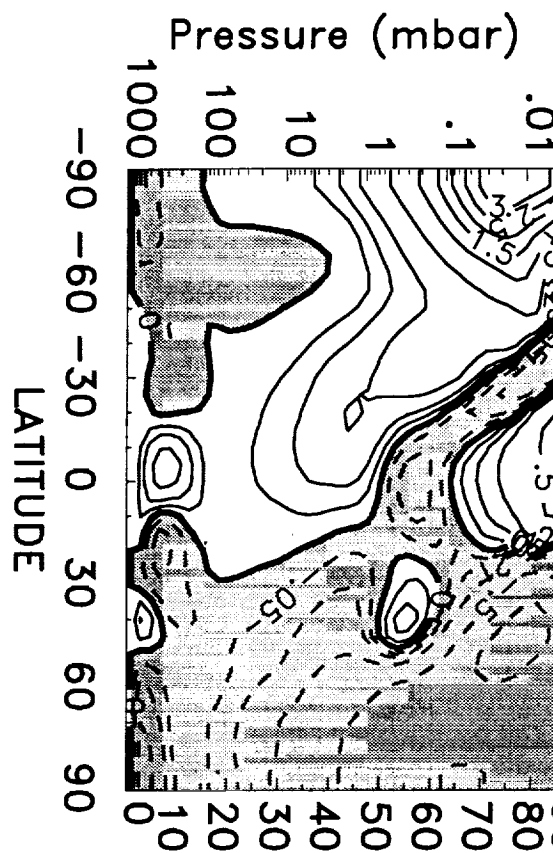


FIG. A.1

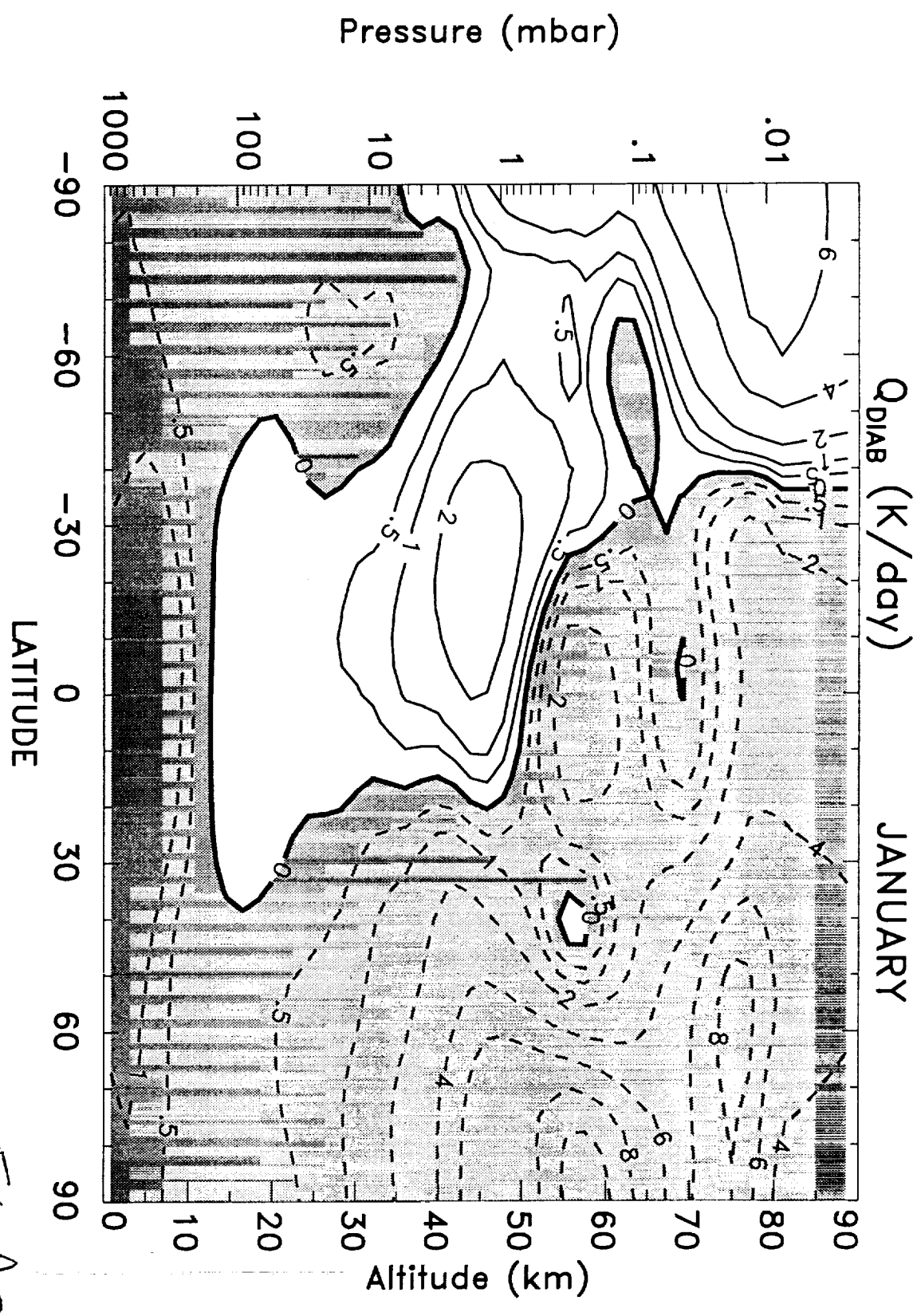


FIG. A.2

# JANUARY

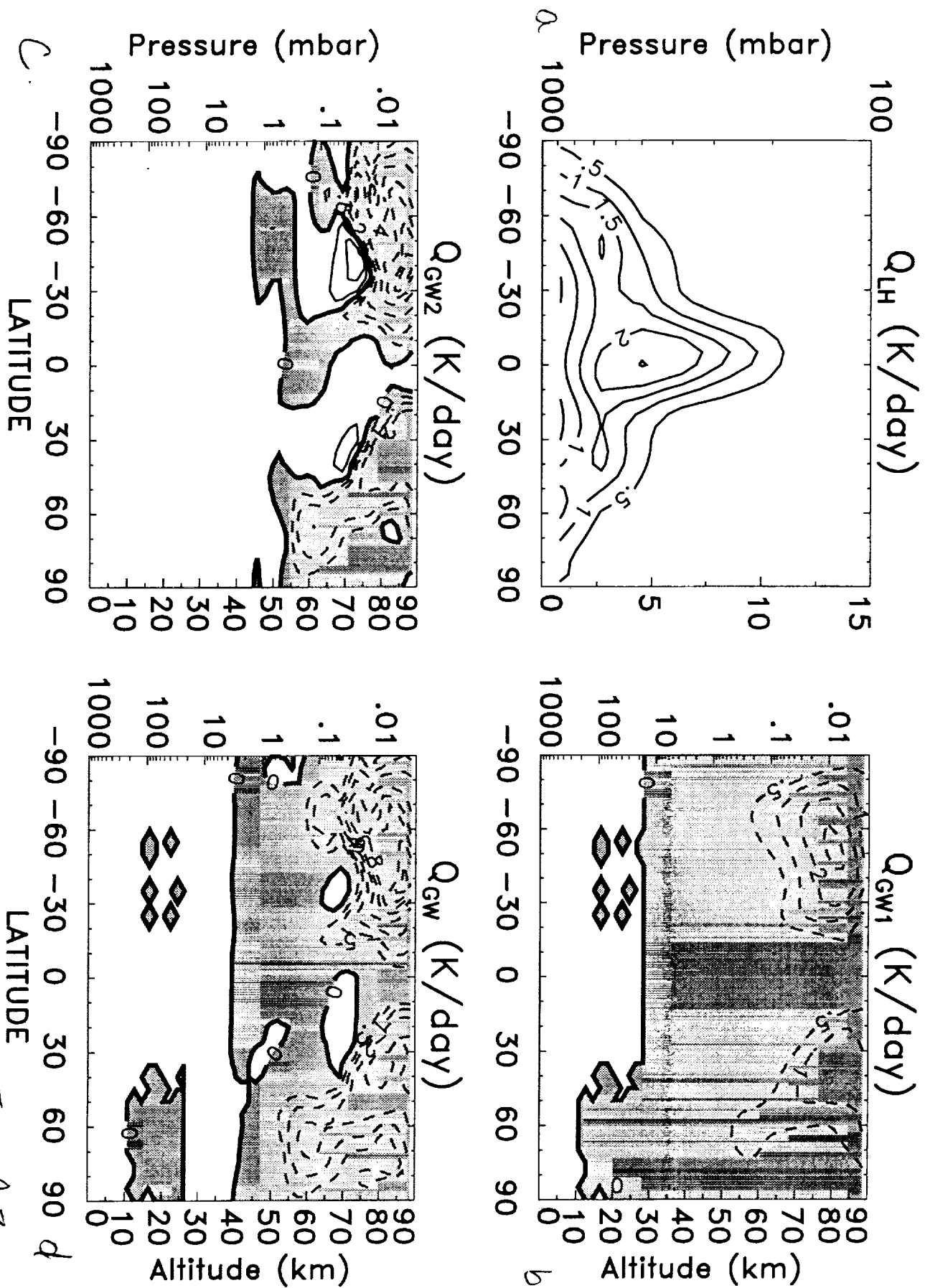


FIG A.3

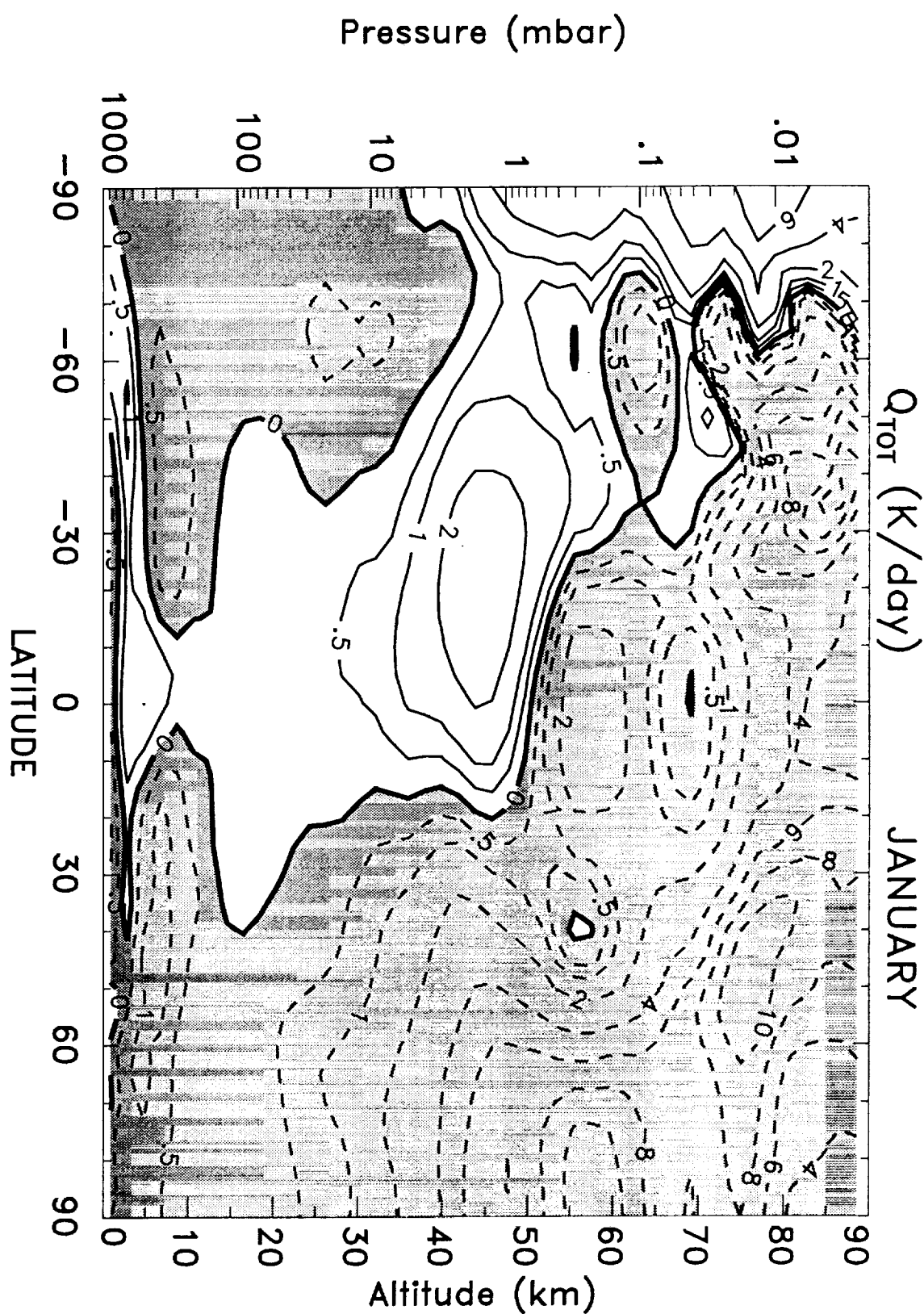


FIG. A.4

# JANUARY

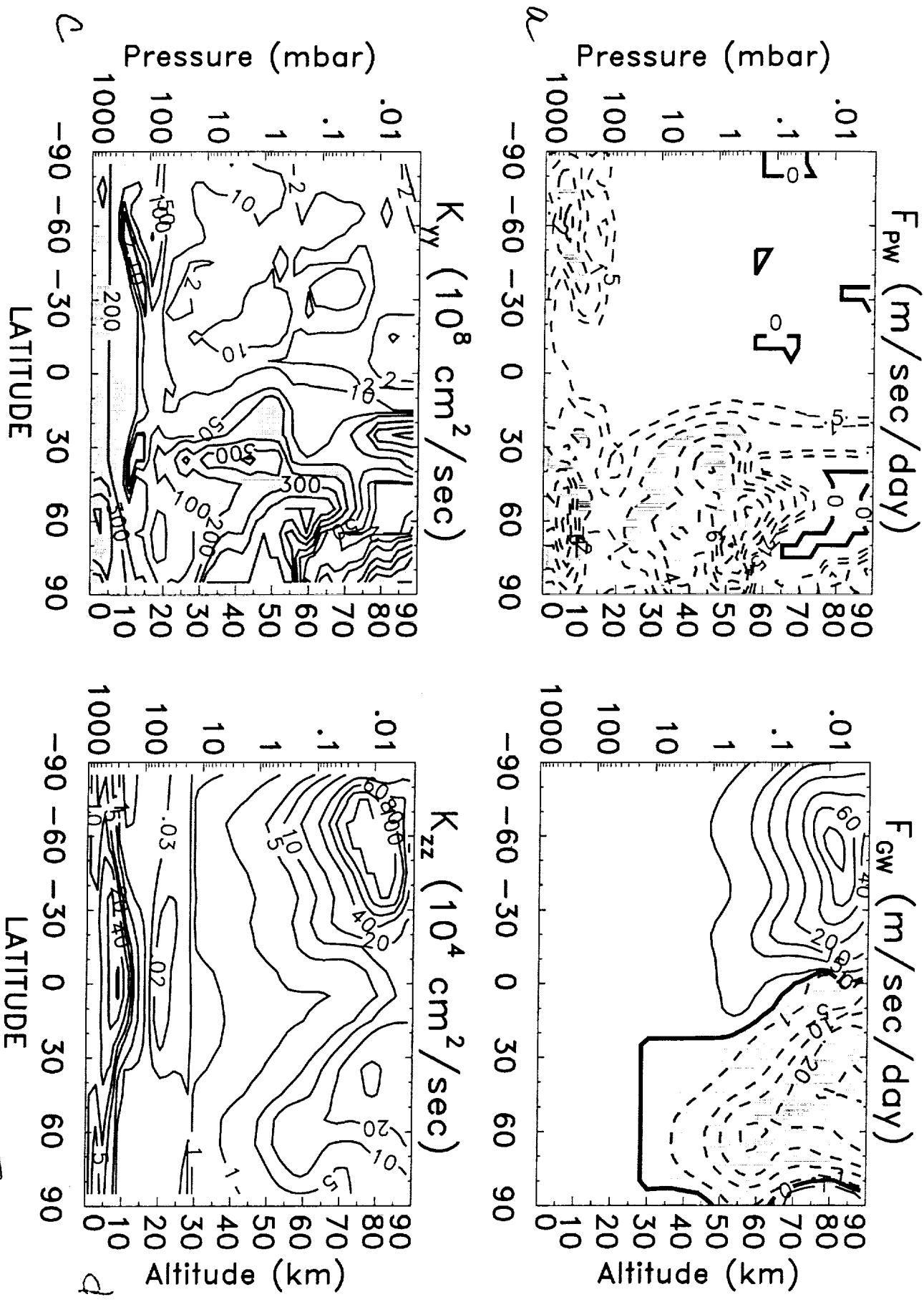


FIG. A.5

Fig A.6a

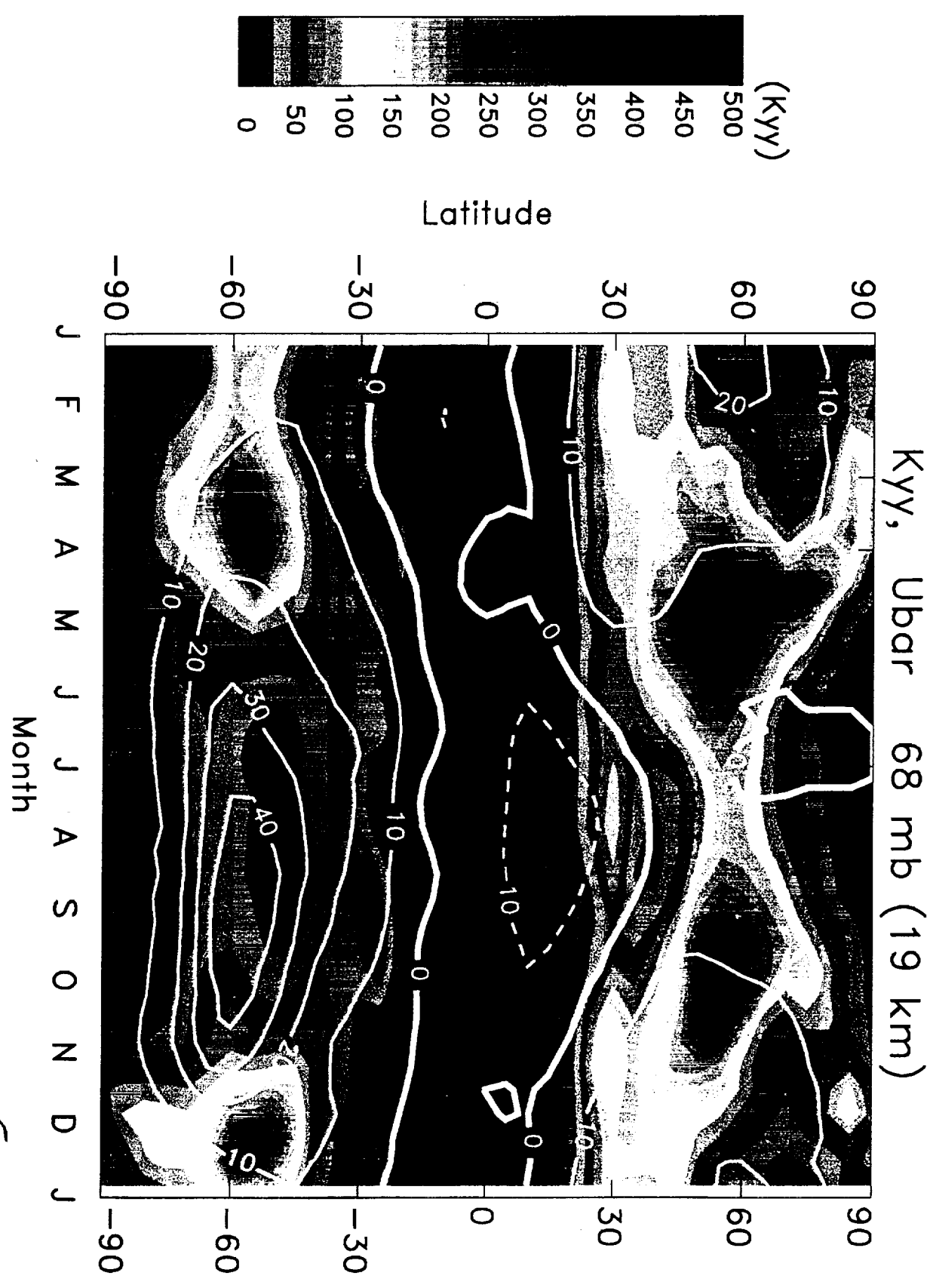


Fig A.6a

fig A.6.b

KYY, Ubar 12 mb (31 km)

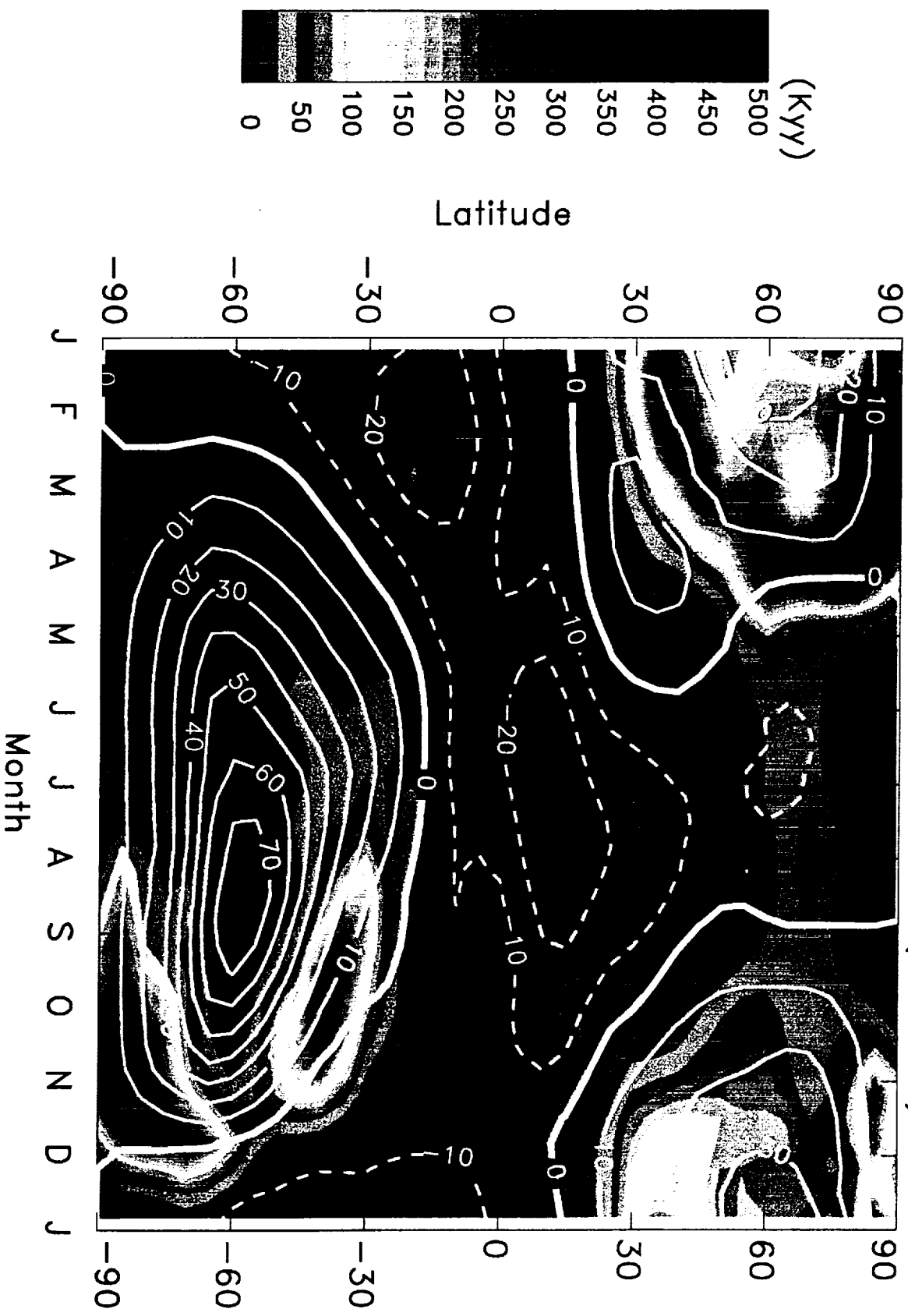


FIG A.6.b

Fig A.6.c

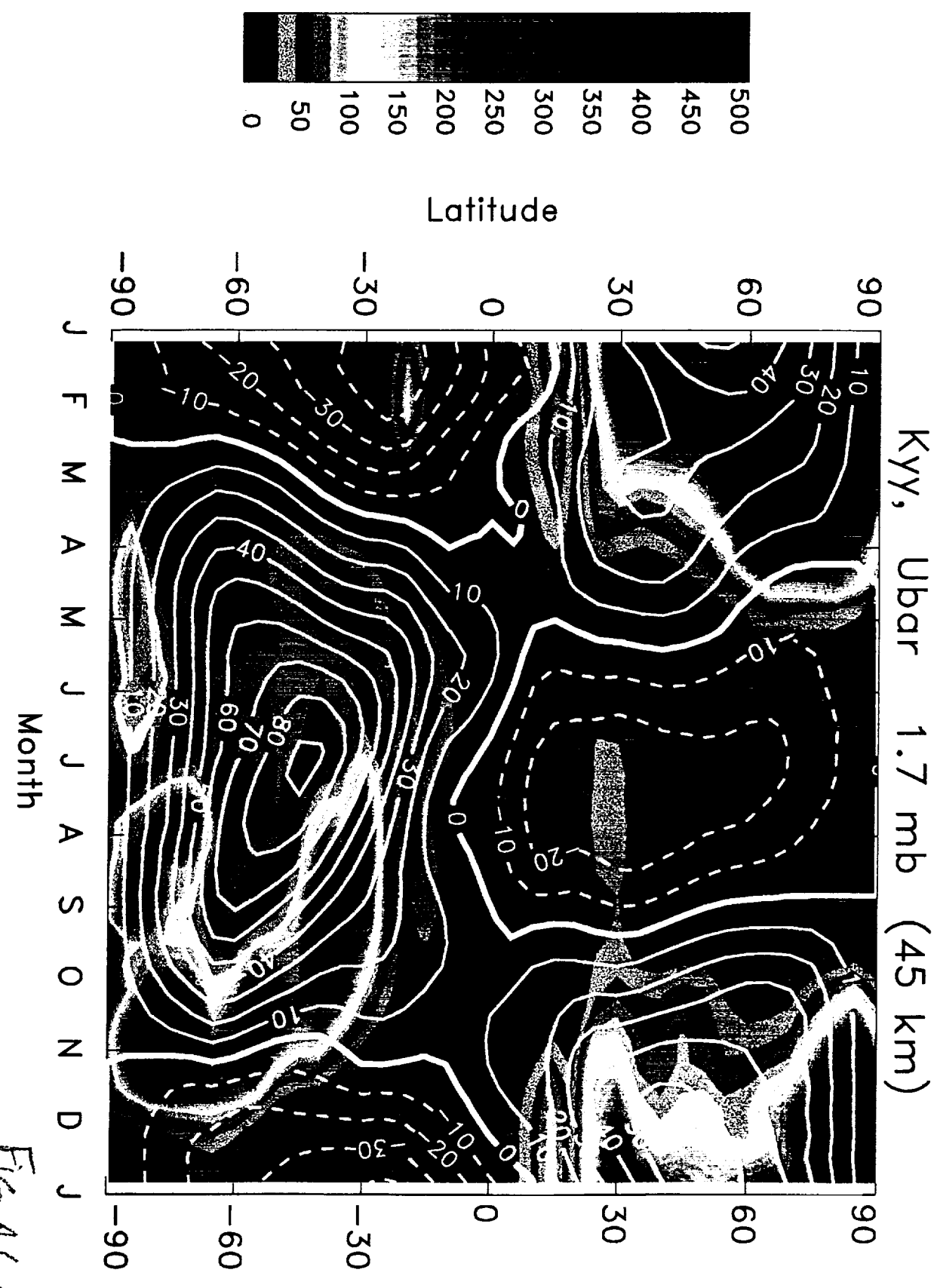


Fig A.6.c

Fig A.6.d

KYY, Ubar .1 mb (65 km)

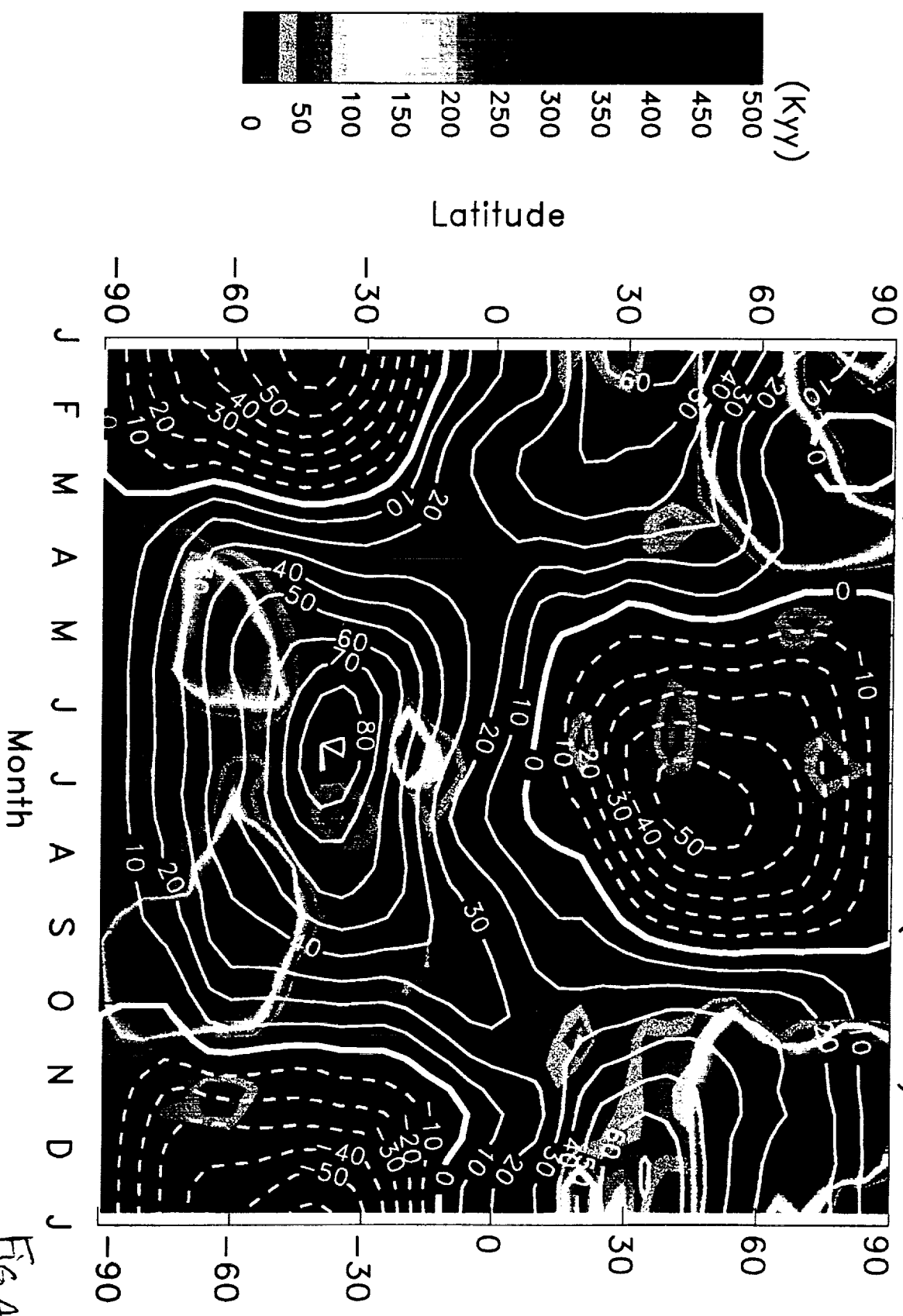


Fig A.6.d

# EQUATOR

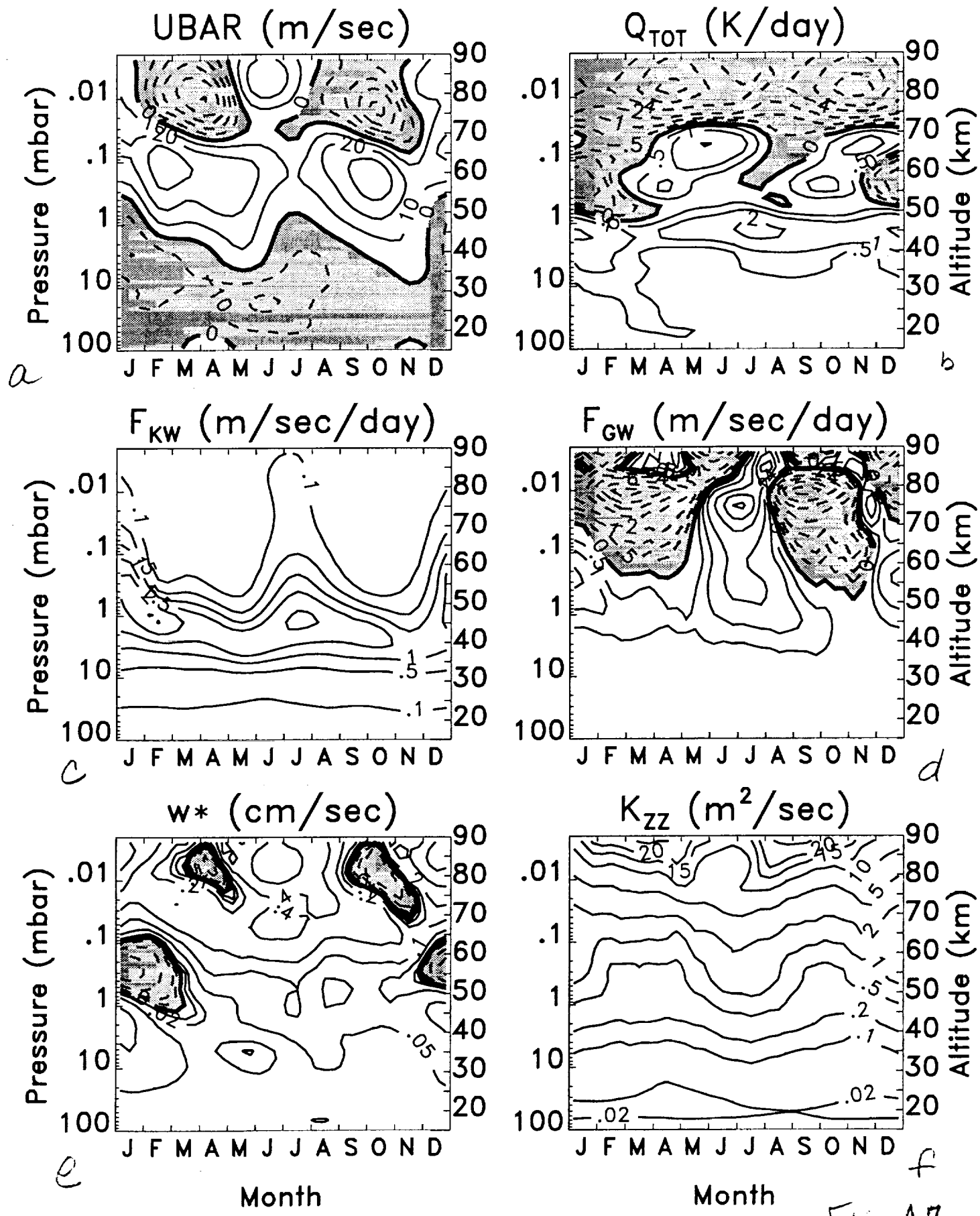


FIG. A.7

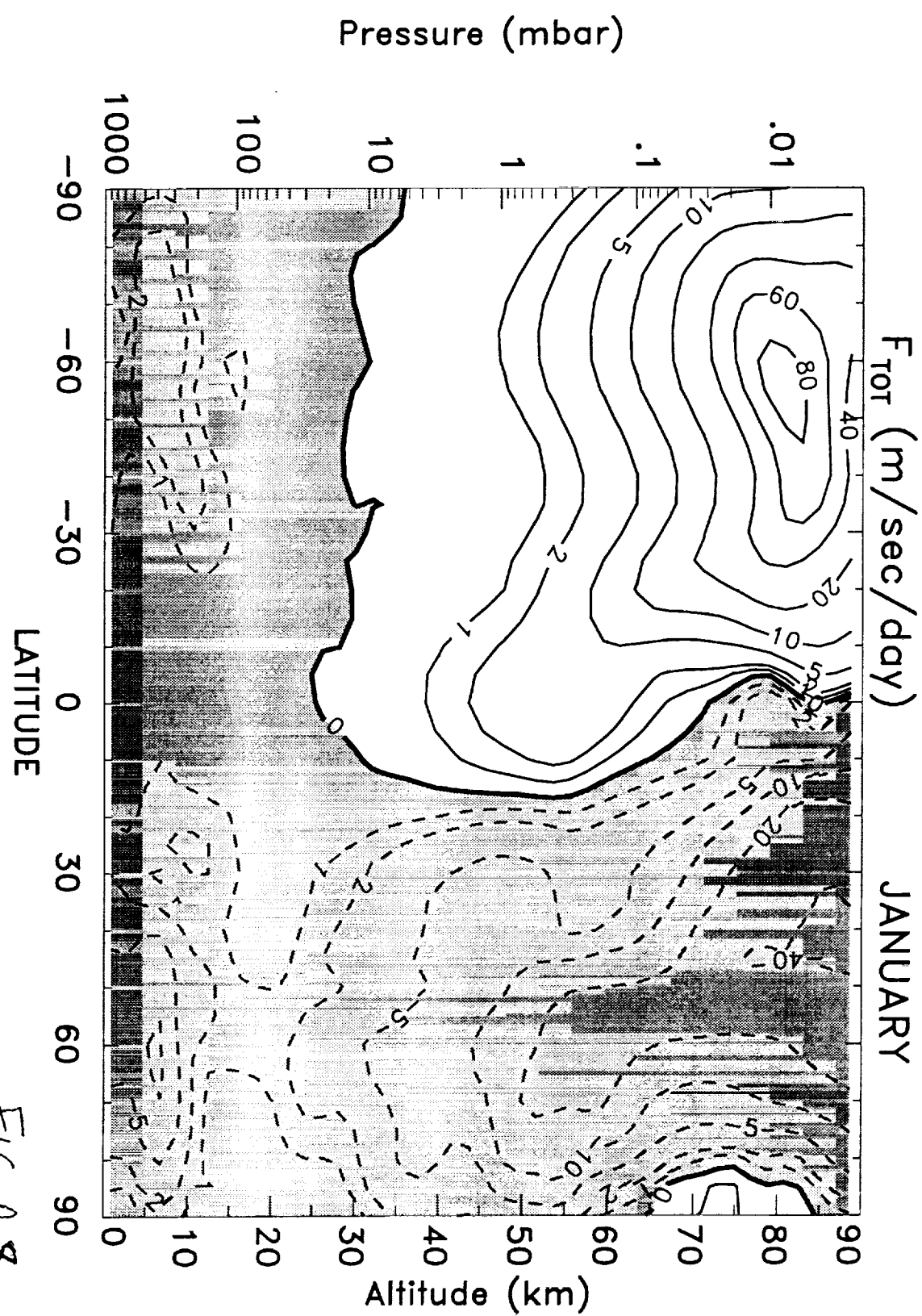


FIG A.8